EXPLORING NOVEL INORGANIC ANTIMICROBIAL NANOSTRUCTURES:

SYNTHESIS, CHARACTERIZATION, AND PROPERTIES

by

LU ZHU

(Under the Direction of Yiping Zhao)

ABSTRACT

Infectious diseases caused by bacteria continue to be a major problem in our daily life. The discovery of antibiotics has helped improve human health and medical treatments dramatically since 1940s. However, the number of infections associated with drug-resistant bacteria keeps increasing in recent years. Inorganic nanomaterial is considered as a promising candidate to solve such a difficult problem. This dissertation focuses on exploring three novel inorganic antimicrobial nanomaterials, carbon dots, $CuBi_2O_4$ and $Cu_xFe_yO_z$, and their morphological, structural, optical, antimicrobial and other properties.

The carbon nanodots with a size around 5 nm are modified with a layer of surface passivation of 2,2′-(Ethylenedioxy)bis(ethylamine) (EDA) molecules. They show visible light induced photodecay rate of $0.307 \pm 0.0002\ h^{-1}$ against methylene blue (MB), and demonstrated 4 logs of *Escherichia coli* (*E. coli*) reduction after 30 min treatment with visible light illumination. Narrow bandgap semiconductor $CuBi_2O_4$ microstructures with different morphologies such as three dimensional hierarchical microspheres, microflowers, one dimensional microrods and nanorods are fabricated through a hydrothermal synthesis approach by systematically changing the synthesis conditions. Among them, the hierarchical micro-flower shaped $CuBi_2O_4$ sample at a

concentration of 1 mg/ml shows a high photodecay rate of $0.114 \pm 0.002\ h^{-1}$ against 30 μM MB, and a high antibacterial effect against *E. coli*, with ~ 93% bacteria reduction after 6 h illumination by a commercial white LED light ($10\ mW/cm^2$) comparing with the negative controls. In addition to these two antimicrobial photocatalysts, the $Cu_xFe_yO_z$ nanostrucutres fabricated by microwave-assisted hydrothermal synthesis exhibit highly antimicrobial properties without light illumination. The optimized $Cu_xFe_yO_z$ nanoparticles (1 mg/ml) can kill 10^9 CFU/ml *E. coli* in PBS in 15 min and 10^{10} CFU/ml *Staphylococcus aureus* (*S. aureus*) in 1 hr. Similar effect is found for highly drug-resistant bacteria such as *K. Pneumoniae* 148 and *H. pylori* X47. These $Cu_xFe_yO_z$ suspensions are also effective in inhibiting the bacterial growth in fresh media and are low toxic to mouse fibroblast cells at 1 mg/ml.

This dissertation work demonstrates that inorganic nanomaterials are promising candidates for antimicrobial applications.

INDEX WORDS: Nanomaterials, Inorganic materials, Metal oxides, Antimicrobial materials, Photocatalysts, Oxidative stress

EXPLORING NOVEL INORGANIC ANTIMICROBIAL NANOSTRUCTURES: SYNTHESIS, CHARACTERIZATION, AND PROPERTIES

by

LU ZHU

B.E., Beijing Institute of Technology, China, 2011

M.E., Beijing Institute of Technology, China, 2013

A Dissertation Submitted to the Graduate Faculty of The University of Georgia in Partial Fulfillment of the Requirements for the Degree

DOCTOR OF PHILOSOPHY

ATHENS, GEORGIA

2018

EXPLORING NOVEL INORGANIC ANTIMICROBIAL NANOSTRUCTURES:

SYNTHESIS, CHARACTERIZATION, AND PROPERTIES

by

LU ZHU

Major Professor:	Yiping Zhao
Committee:	Leidong Mao
	Ralph A. Tripp
	Xianqiao Wang
	William Kisaalita

Electronic Version Approved:

Suzanne Barbour
Dean of the Graduate School
The University of Georgia
August 2018

DEDICATION

To my parents.

ACKNOWLEDGEMENTS

First and foremost, I would like to express my deepest gratitude to my advisor Dr. Yiping Zhao for his academic guidance, scientific insight and patience throughout my Ph.D. studies. I would also like to thank my advisory committee members Dr. Leidong Mao, Dr. Ralph A. Tripp, Dr. Xianqiao Wang and Dr. William Kisaalita, and also Dr. Ya-ping Sun from Clemson University for their guidance, without whom, this dissertation would not have been possible.

I owe special thanks to my family and friends for years of support. Their love, support, encouragement, and sacrifices motivate me all the time.

Finally, I would like to acknowledge many of my colleagues, both past and present for the help throughout my Ph.D. program: Dr. Rui Cheng, Dr. Weijie Huang, Dr. Yizhuo He, Dr. Jing Chen, Dr. Xiaomeng Wu, Dr. Whitney Ingram, Dr. George Larsen, Dr. Manoj Manjare, Dr. Bin Ai, Mr. Steven Larson, Mr. Layne Bradley, Ms. Zilan Yang, and Mr. David Pearson.

TABLE OF CONTENTS

Page

LIST OF TABLES

Page

LIST OF FIGURES

Page

CHAPTER 1

INTRODUCTION

1.1 Development of antimicrobial materials

Throughout the human societal development, infectious diseases have accounted for a large portion of human death. Even today, infectious diseases are still the second leading cause of death, the leading cause of disability-adjusted life years worldwide (1 disability-adjusted life year is 1 lost year of healthy life), and the third leading cause of death in the United States. [1-3] Among those, bacteria caused infections contribute to a large portion of overall infections. The leading pathogens include *Salmonella*, *Escherichia coli* (*E. coli*), *Shigella*, *etc*. As reported, 31 known foodborne pathogens such as *E. coli* O157:H7 and *Salmonella spp*. are responsible for 9.4 million illnesses in the United States each year [4]. Many methods have been developed to inactivate the pathogenic bacteria for different situations throughout history. For example, from the medical aspect, there are three common methods of sterilization for medial materials/devices: ethylene oxide exposure, g-irradiation, and steam sterilization. [5] However, these methods have serious drawbacks, such as they are expensive, the residue of ethylene oxides are toxic to bio-systems, and hard to be directly applied to biomaterials. [5] Thus, the development and use of appropriate antimicrobial agents are important for the human society.

In 1928, an important millstone for the development of antimicrobial agents was set. A substance produced by a blue mold (a fungus from the *Penicillium* genus) was discovered effective to inhibit the growth of *Staphylococcus aureus* (*S. aureus*) by a Scottish scientist Alexander Fleming, and this substance was named as penicillin. [6] Penicillin came into the clinical use in

1940s and saved tens of thousands of lives during World War II. After penicillin, many other effective antibiotics were found. For example, sulfonamide was discovered in 1935, aminoglycoside, chloramphenicol, tetracycline, macrolide, and vancomycin in 1950s. [6] Improvement of each category of antibiotics were achieved in the past decades. For example, evolutions and improvements of penicillin has been achieved. As shown in **Figure 1.1**, the group of penicillin antibiotics has been developed from penicillin G to methicillin, ampicillin and piperacillin. Originally, penicillin was effective on Gram-positive bacteria, such as *S. aureus*. Later on, methicillin was developed to fight against the penicillin-resistant *S. aureus*. Ampicillin was developed to inhibit some Gram-negative bacteria, such as *E. coli*. From the structure of ampicillin, piperacillin (even effective on Gram-negative *Pseudomonas aeruginosa*) was derived to be effective on broader antimicrobial spectrum. [6]

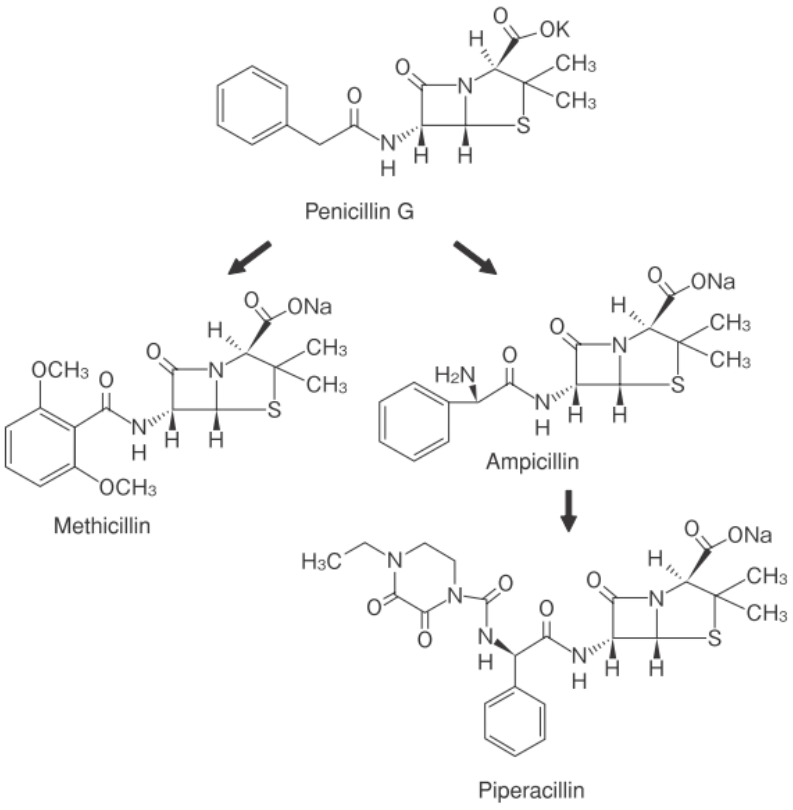

Figure 1.1. Evolution of penicillin antibiotics. Reprint from [6].

However, because of the widespread and frequently use of antibiotics for a very long time, the targeted infectious bacteria have gradually adapted to the antibiotics and changed its respond to the drugs. In the research nowadays, the speed of antibiotic development has been reduced because of such emergence of drug resistant bacteria (when bacteria don't respond to the drugs designed to inhibit their activities [7]). According to U.S. Centers for Disease Control and Prevention, more than 2 million of severe infections were caused by the antibiotic resistant bacteria annually. For example, Carbapenem-resistant Enterobacteriaceae (CRE) are bacteria that are resistant to nearly all antibiotics and spread easily.[7] New antimicrobial approaches other than the use of antibiotics have been proposed and developed, such as photodynamic therapy [8] and bacteria inactivation by nanoparticles [9-10]. Inorganic nanomaterials are considered as a group of promising alternative materials. [11] Here, the inorganic antimicrobial materials can be divided into two major catalogs based on their mechanisms of actions, the photocatalytic antimicrobial materials and metal/metal oxide nanomaterials that can directly lead to bacteria elimination or death. Due to the advanced oxidation processes induced by photocatalytic properties, metal oxides based photocatalytic nanomaterials have shown great promise as effective non-targeted disinfectants against a wide range of microorganisms and decomposition of chemical contaminants.[12-22] The highly reactive oxygen species generated by inorganic photocatalysts serves as the main oxidant, and are capable of inactivating microorganisms including viruses, bacteria, spores and protozoa. At the early stage of antimicrbial application of photocatalysts, ultraviolet (UV) light is usually utilized to activate their antibacterial function due to the energy bandgaps of the photocatalyst. [23-25] For example, the well-known nanostructured titanium dioxide (TiO_2) has been demonstrated to have a high antimicrobial efficiency under UV light irradiation.[26] However, from a practical point of view, an ideal photocatalytic antimicrobial

material should be able to utilize the energy of natural sunlight or indoor illumination. Thus, over the past decades, many efforts have been attempted to develop visible light driven antimicrobial photocatalysts based on those large bandgap materials through different strategies, such as doping,[27-28] coupling with other semiconductor materials, [29-30] coupling with carbon based materials, [31-33] *etc*. For example, the visible light induced bactericidal ability of N-doped TiO_2 has been reported by Wong *et al*. [28] It has been demonstrated to be effective on killing different kinds of human pathogens such as *S. flexneri*, *L. monocytogenes*, and *V. parahaemolyticus* under visible light illumination. A hybrid Cu_xO/TiO_2 nanocomposite reported by Qiu *et al*. has been shown to be efficient for volatile organic compound (VOC) decomposition and antipathogenic (bacteria and viruses) effects under indoor conditions. [34] An alternative approach is to explore new semiconductor materials with narrow energy bandgaps. Ag_3PO_4, with a bandgap of 2.36 − 2.43 eV, is considered as a highly efficient visible light photocatalyst. [35] However, Ag_3PO_4 is not stable during photocatalysis. [35] Other Ag_3PO_4 related heterostructures, such as $Ag_3PO_4/TiO_2/Fe_3O_4$ nanocomposites [29] and $P25/Ag_3PO_4$/graphene oxide heterostructures [36] have also been reported as antimicrobial materials. Bai *et al*. have fabricated "corn-like" ZnO/Cu hierarchical structures through a two steps hydrotehrmal synehsis. The as-syntehsized material has shown about 7 log reduction of *E. coli* under visible light irradiaiton at a dosage of 0.1 g/L for 30 min. [37] Graphene based materials are also a popular study subject in the research of photocatalyst due to their unique chemical and physical properties, such as high electron conductivity and large surface area. They are promising materials to enhance the photocatalytic activities of the semiconductor based photocatalysts. [38-40] For example, Gao *et al*. have used graphene oxide to modify CdS. The GO-CdS composite has shown much less leaking of Cd^{2+} (3.5 wt%, for pure CdS which is 38.6 wt%). This composite also showed nearly 100 % bacterial inhibition of both Gram-

positive (*Bacillus subtilis* (*B. subtilis*)) and Gram-negative (*E. coli*) bacteria within 25 min under visible light illumination. [38]

Other than the photocatalysts, metal oxides/metal nanoparticles which can directly introduce oxidative stress to the bacterial cells are also popular antimicrobial materials. For example, Ag nanoparticles are widely studied for antimicrobial applications. [9-10] The study of Baker *et al.* has shown that with Ag nanoparticles surface concentration as low as 8 μg of Ag/cm^2, the surface is completely cytotoxic to *E. coli*. [41] Other metal nanoparticles have also been investigated. Cu nanoparticles with a size of 2 – 5 nm in diameter embeded into sepiolite have been reported to be able to kill both *S. aureus* and *E. coli* (with a starting concentration from 2.5×10^5 to 10×10^5 CFU/ml) by 99.9%. [42] Jia *et al.* have prepared Cu nanoparticle coated cellulose films, and these films have shown effective antibacterial activities against *S. aureus* (4 log reduction) and *E. coli* (3 log reduction) after 0.5 hrs exposure in PBS at 37 ^oC. [43] Similarly, the antimicrobial acitivities of other metal oxides nanoparticles have also been studied. [44] Perelshtein *et al.* have coated the surface of cotton fabrics with 15 nm CuO nanocrystals, the resutled CuO-cotton composite are demonstrated as effective to inactivate both *S. aureus* and *E. Coli* in NaCl solutions, even with a 1% coating dosage. [45] The study of Saravanan *et al.* has shown that the inhition zones of *S. aureus* and *E. coli* by $ZnO/Ag/Mn_2O_3$ nanocomposite is twice as large as that of ZnO under the same conditions. [46]

1.2 The mechanisms of antimicrobial activities of different materials

1.2.1 Structure of bacterial cells

To understand the mechanisms of the antimicrobial activities, it is important to understand the structures of the bacterial cells first. Here we will briefly discuss about the structure of a

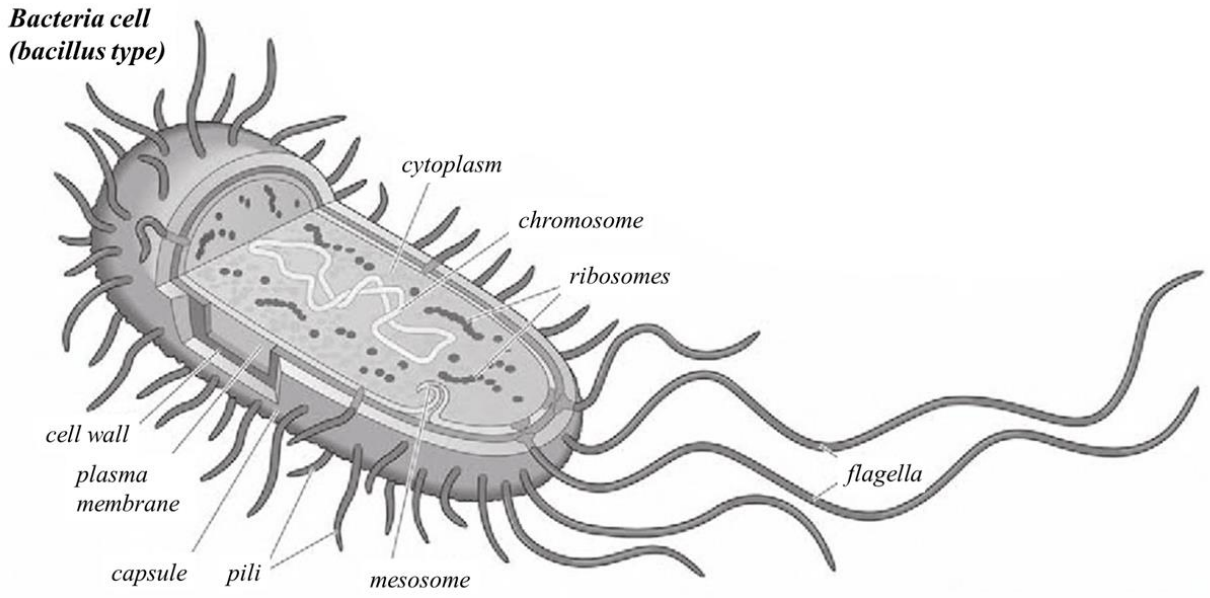

Figure 1.2. Illustration of a bacteria cell (*bacillus* type, Gram-positive). Reprint from [47].

bacteria cell. **Figure 1.2** illustrates of a *bacillus* type bacteria cell, which mainly includes the cell wall, plasma membrane, ribosomes, chromosome, cytoplasm, capsule, pili, and flagella. [47] The structure of the bacterial cells differs from the structure of mammalian cells and other plant cells. One of the fundamental differences is that a bacterial cell does not have the intracellular organelles.

In the structure of the bacterial cells, the cell wall and the plasma membrane play important roles of protecting and holding the structure of the bacteria. The wall of a bacterium is much stronger than the cell walls of higher plants at a unit thickness due to the special chemical and physical structure of the bacterial wall. [48] Although the bacterial cell walls vary from organism to organism, peptidoglycans are the major parts of bacterial cell walls. The peptidoglycans consist of large amino acid molecules, they are cross-linked to molecules of polysaccharides to form a network. [48] **Figure 1.3(a)** and **(b)** show the top and side views of the structure of the polymeric peptidoglycan segment of the cell wall. [49] And the structures of the cell wall of the Gram-positive bacterial cell and the Gram-negative cell are different. The Gram-positive cell walls are

thick and the peptidoglycan layer constitutes almost 95% of the cell wall, while the Gram-negative bacteria have as little as 5-10 % peptidoglycan of the cell wall (**Figure 1.3(c)**). The plasma membrane of the bacterial cell is composed of a phospholipid bilayer, and it works as a permeability barrier. Pili and flagella are the external structures of bacteria. Pili are the extending parts out from the membrane and can attach the cell to a surface. Flagella are the parts that the bacterium uses to swim.

Inside of the cell wall and membrane, the bacterial structure is simpler than the internal structure of a mammalian cell. The cytoplasm of a bacterium is a matrix composed of water, enzymes, nutrients, wastes, and gases; it also contains bacterial cell structures such as ribosomes, a chromosome, and plasmids. Thus, the cytoplasm of the bacterial cell is responsible for the functions for cell growth, metabolism, and replication, *etc*.

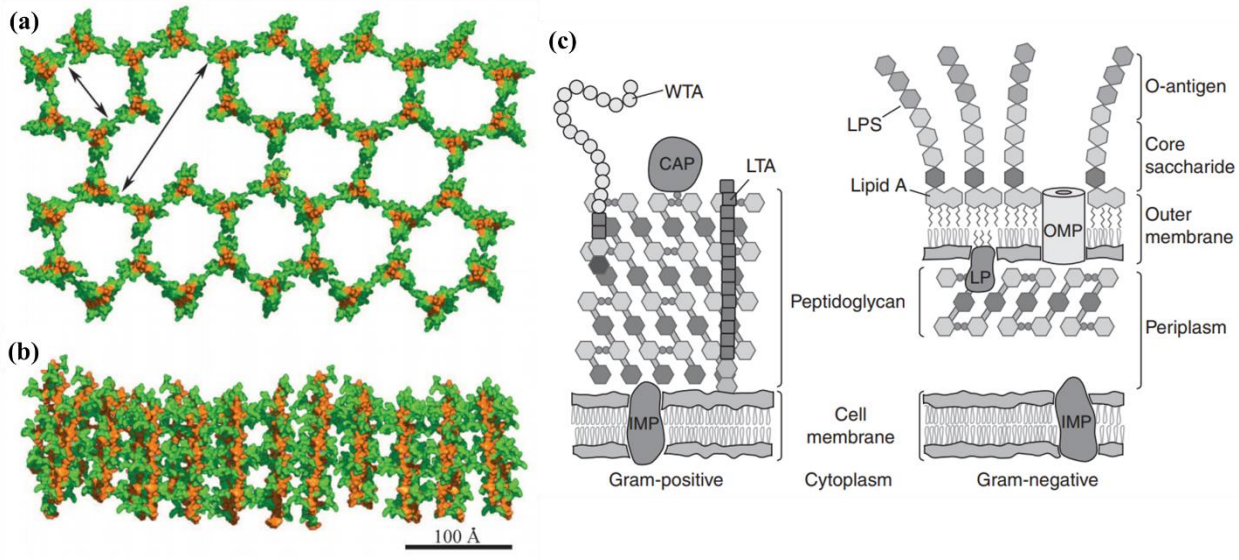

Figure 1.3. (a) and (b) Top and side views of the structure of the polymeric peptidoglycan segment. Reprint from [49]. (c) Depiction of Gram-positive and Gram-negative cell envelopes: CAP: covalently attached protein; IMP: integral membrane protein; LP: lipoprotein; LPS: lipopolysaccharide; LTA: lipoteichoic acid; OMP: outer membrane protein; WTA: wall teichoic acid. Reprint from [50].

1.2.1 Traditional antimicrobial agents

Throughout the history, many disinfection methods to remove or inhibit the activities of bacteria have been developed, and they mainly include two categories, the chemical, and physical disinfections. [51] A major part of the disinfectants are based on chemicals such as phenol, alcohol and aldehydes. The detailed antimicrobial principles of the chemical disinfectants vary from chemical to chemical and they might be hard to identify. They mainly include oxidation, reduction, and introducing cytotoxicity to bacterial cells. The physical disinfection methods mainly include raising the temperature, fumigation, drying, and filtration. [51] However, for the medical treatments, nowadays, antibiotics are the most important antimicrobial agents. For example, as mentioned earlier, the discovery of penicillin is one of the important millstone in human health history. The antimicrobial activity of the antibiotics includes several steps. Generally, the antibiotic has to be able to enter the bacterial cells firstly. Then it needs to be stable enough in the bacterial cells to accumulate to inhibitory concentrations. [52] However, the detailed principles of actions of different antibiotics are different. Several categories of antibiotics can inhibit the cell-wall synthesis, then stop the replication of the bacteria cells, such as the *β*-Lactams antibiotics (e.g. penicillins, cephalosporins, cefotaximes, and carbapenems), glycopeptides (e.g. vancomycin), and streptogramins (e.g. virginiamycins, quinupristin and dalfopristin). Some antibiotics can inhibit the protein synthesis of bacteria then stop bacteria activities, such as aminoglycosides antibiotics (e.g. streptomycin, gentamycin, tobramycin and amikacin). There are several other kinds of antimicrobial mechanisms for antibiotics, such as disrupting the DNA replication of the bacterial cell, inhibiting ribsosomal complex, *etc*. The antimicrobial actions of selected antibiotics are summarized in **Table 1.1**. Since the chemical structures of the antibiotics discovered until early 1970s have been used as leads to generate new generations of clinically useful antibiotics by

chemical modification, [53] here the antimicrobial mechanism of penicillin is discussed as an example. The mechanism of bacteria killing by penicillin is illustrated in **Figure 1.4**. Overall, the bacteria cells are killed by the specifically inhibiting the transpeptidase of penicillin (for instance, penicillin binding proteins (PBP)). The transpeptidase catalyzes the final step in cell wall biosynthesis, the cross-linking of peptidoglycan. [54] As shown in **Figure 1.3**, the cell wall contains polymeric peptidoglycan segments. And the peptidoglycan consists sugars (such as N-acetylglucosamine (NAG) and N-acetylmuramic acid (NAM)) and amino acids. As shown in **Figure 1.4(a)**, the bacterial cell wall consists of strands of repeating NAG and NAM subunits. And the peptide chains are attached to the NAMs. The NAG and NAM strands are cross-linked together by the amino acids such as alanine. These amino acids are linked by the transpeptidase, such as PBP (**Figure 1.4(b)** and **(c)**). Once the penicillin is added into the system, it enters the active site of the PBP and binds to PBP (**Figure 1.4(d)**). The binding between the PBP and penicillin activate the antibiotic and inactivate the transpeptidase enzyme (**Figure 1.4(e)**). Thus, the cell wall synthesis can be inhibited by penicillin. [55] Due to the difference of cell wall structures shown in **Figure 1.3(c)** between the Gram-positive and the Gram-negative bacteria, the actions of penicillin are different on these types of bacteria. It is clear that penicillin works more effective on the Gram-positive bacteria than the Gram-negative type.

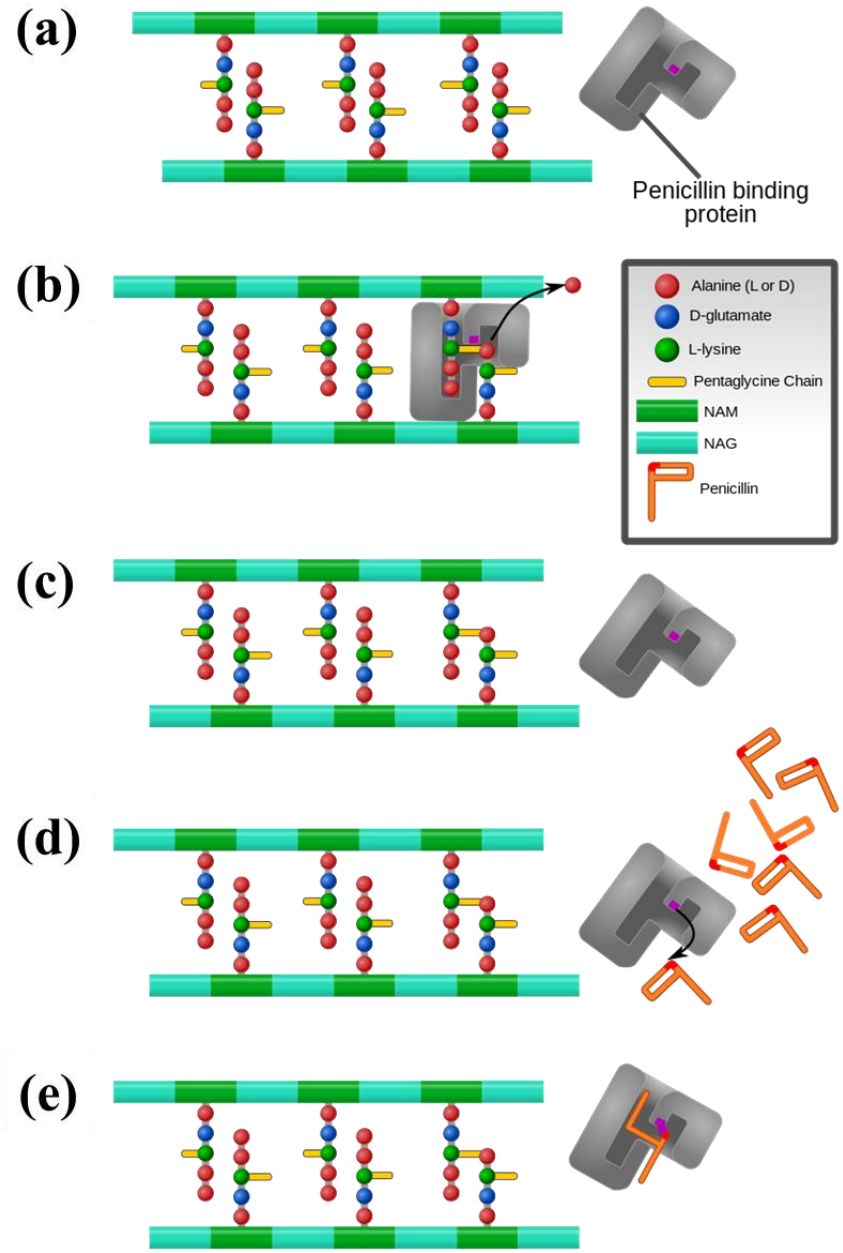

Figure 1.4. Penicillin and other β-lactam antibiotics act by inhibiting penicillin-binding proteins, which normally catalyze cross-linking of bacterial cell walls.(a) The bacterial cell wall consists of strands of repeating NAGs and NAMs. The peptide chains attached to NAMs. (b) The PBP binds the peptide side chains and forms the cross-link with the expulsion of one D-Alanine from one peptide side chain. (c) The PBP dissociates from the wall once the cross-link has been formed. (d) Penicillin enters the systems, binds to the active site of the PBP and reacts with the serine group that is important in its enzymatic activity. (e) The beta-lactam ring of penicillin (represented here as the top of the "P") is irreversibly opened during the reaction with the PBP. Penicillin remains covalently linked to the PBP and permanently blocks the active site. Reprint from [55].

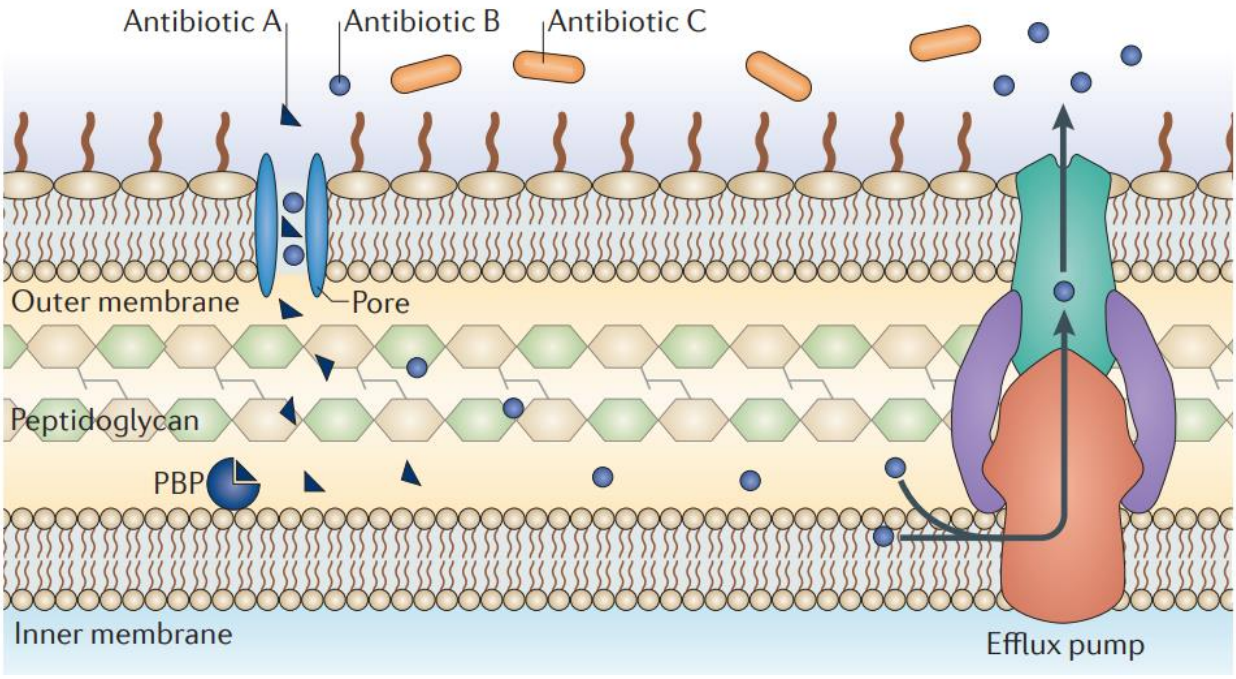

Figure 1.5. Bacterial intrinsic mechanisms of resistance. Antibiotic A, Antibiotic B, and Antibiotic C are used to represent three different *β*-lactams antibiotics. Reprint from [56].

However, with the broad using of antibiotics, the drugs designed to inactivate the bacteria tend to be less and less effective. Drug resistant bacteria start to threaten human health in recent years. The antibiotic resistance is a natural phenomenon, **Figure 1.5** shows an overview of the mechanisms of the bacterial intrinsic resistance of the *β*-lactams antibiotics (A, B, and C are used to represent three different *β*-lactams antibiotics). As shown in **Table 1.1**, the *β*-lactams kill the bacteria by inhibiting the synthesis of cell wall. However, as shown in **Figure 1.5**, the *β*-lactams antibiotics are targeting the PBP. Antibiotic A gets through the outer membrane and enters the bacterial cell via a membrane-spanning porin protein. Then it reaches the target and inhibits the synthesis of peptidoglycan. Antibiotic B can also enter the cell *via* the pores, but it can be removed by efflux of the cell, then it cannot effectively work to inhibit the cell wall synthesis. And antibiotic C cannot cross the outer membrane then is unable to target the PBP. [56] Most antibiotics bind with its specific targets then prevent the normal activity of the targets. [56] However, the mutation

of the bacterial cells lead to the changes in the structures of the antibiotic targets, which can prevent the binding of the antibiotics. And such development in antibiotic resistance has grown as one of the biggest challenges to the modern medical treatment of the infectious disease. Seeking new antimicrobial approaches is urgent to improve medical treatments of infectious diseases.

Table 1.1 Representative antibiotics and their modes of action. [52]

Category	**Example members**	**Mode of action**
β-Lactams	Penicillins, Cephalosporins, Cefotaximes, Carbapenems	Inhibition of cell wall synthesis
Aminoglycosides	Streptomycin, Gentamycin, Tobramycin,Amikacin	Inhibition of protein synthesis
Quinolones	Ciprofloxacin, Ofloxacin, Norfloxacin	Inhibition of DNA replication
Glycopeptides	Vancomycin	Inhibition of cell wall synthesis
Tetracyclines	Tetracycline	Inhibition of translation
Rifamycins	Rifampin	Inhibition of transportation

1.2.2 Inorganic antimicrobial agents

Combining the wide range of material choice provided by the inorganic materials, and the unique properties of nanomaterials, the inorganic nanomaterials provide a promising future as the antimicrobial agents. It might be one of the most promising approaches to overcome microbial drug resistance. As shown in **Figure 1.6**, nanoparticles can inactive the bacterial cells in multiple ways depending on the properties of the applied materials, such as generating reactive oxygen

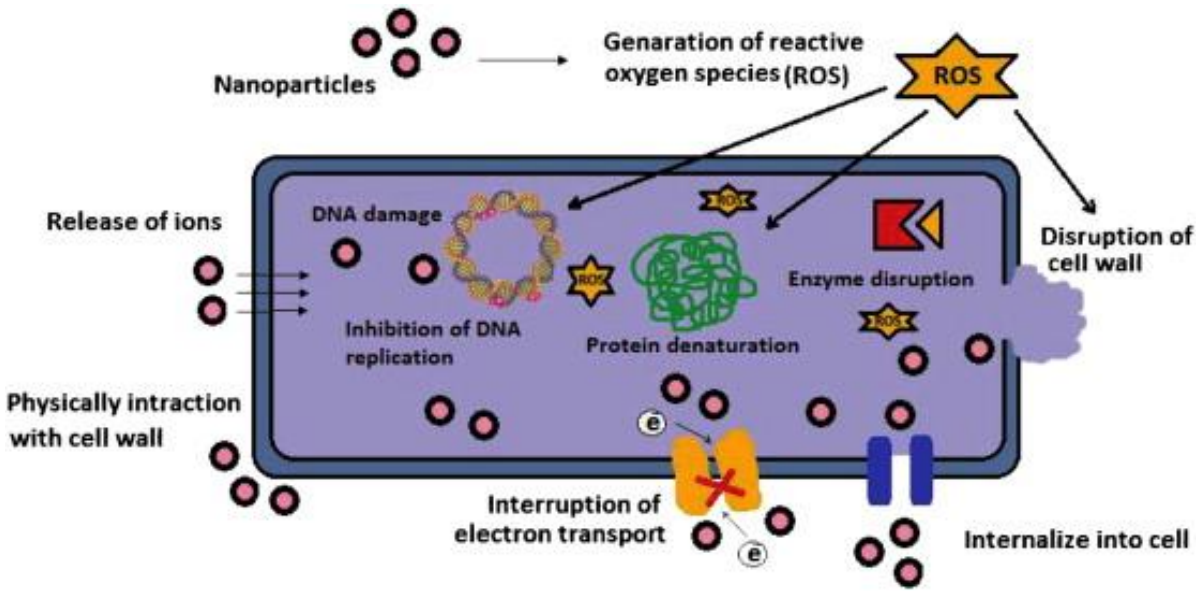

Figure 1.6. Various mechanisms of antimicrobial activity of nanoparticles. Reprint from [57].

species (ROS), releasing irons to the cells, disrupting the enzyme activities, inhibiting the DNA replication, and interrupting electron transportation of the cell membrane, *etc*.[57] Here we will discuss different mechanisms of the inorganic antimicrobial materials. They are classified into three categories, photocatalysts, metal nanoparticles, and metal oxides nanoparticles.

1.2.2.1 Photocatalysts

Since the first report of the photocatalysis of TiO_2 in 1972 [58], thousands of literature have been devoted to the study of photocatalysts. The photocatalytic antimicrobial activity of the TiO_2 against *E. coli* and other strains has been demonstrated by Matsunaga *et al.* in 1985. [26] Antimicrobial photocatalysts are usually semiconductor materials, and their photocatalytic antimicrobial performances is strongly affected by their electronic band structures. In the electronic band structure of a semiconductor, the conduction band and the valance band are close enough to the Fermi level so that the thermally populated electrons or holes can be produced. The photocatalytic activity of a photocatalyst involves three major steps [59-60]: (1) photons with

energy equal to or larger than the band gap energy of the semiconductor is absorbed by the photocatalyst, which leads to the generation of free electron (e^-) - hole (h^+) pairs inside the photocatalyst; (2) the photogenerated electrons and holes separate and migrate to the surface of photocatalysts; (3) the absorbed chemicals on the surface of the photocatalyst are reduced and oxidized by the photogenerated electrons and holes. **Figure 1.7** summarized the photocatalytic activity of TiO_2. As shown in **Figure 1.7**, the TiO_2 nanoparticle can absorb and utilize the UV light that has photon energy greater than its band gap energy (~ 3.2 eV). [61] The absorbed photon energy then excites the electrons from the valance band to the conduction band, then leaves holes on the valance band. The generated electrons on the conduction band can reduce the surface absorbed oxygen to generate the superoxide radical, while the holes on the valance band can oxidize the surface absorbed water molecules to generate hydroxyl radicals. [61] Both the superoxide radicals and the hydroxyl radicals are part of the ROS.

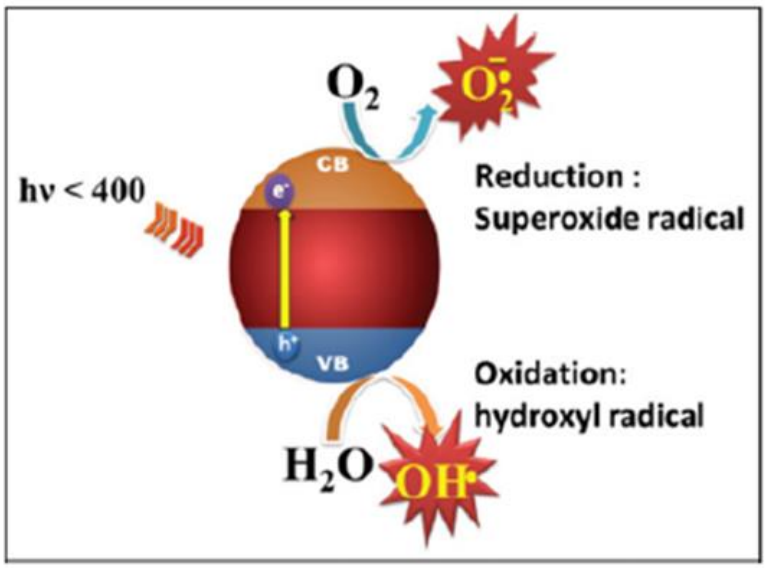

Figure 1.7. The UV-responsive TiO_2 photocatalytic reaction. Reprint from [61].

The ROS generated by photocatalysis can affect the activity of the bacterial cells directly or indirectly. As shown in the scanning electron microscope (SEM) images of **Figure 1.8**, after the treatments with light and photocatalysts, bacterial flagella, parts of the cell wall, and the cell membrane are disappeared. Some 'holes' on the cells have appeared. It indicates the damage of cell integrity by the photocatalysis. More interestingly, the transmission electron microscope (TEM) images (**Figure 1.9**) show that interior damage of the cells also occur after the photocatalytic disinfection. Comparing with the healthy cell, dark mass aggregates have appeared in the 2-hour treated *E. coli* cells. [62]

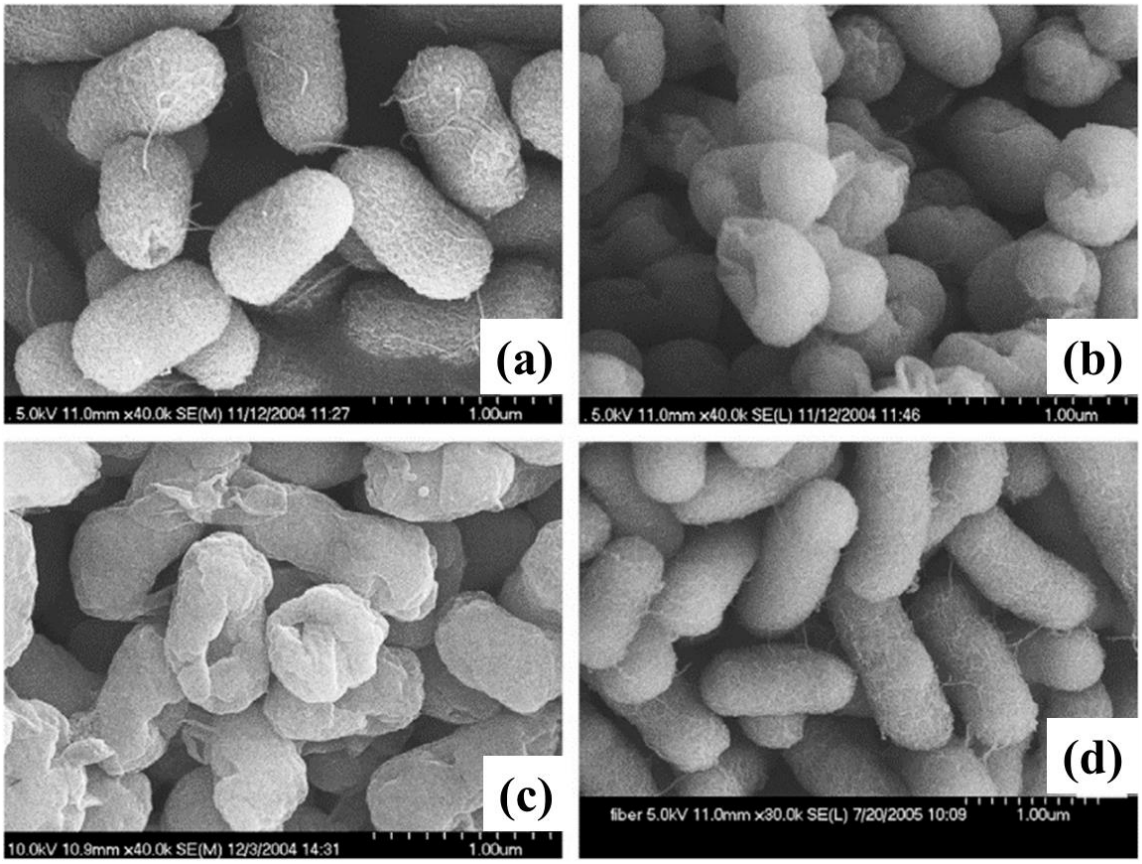

Figure 1.8. SEM images of *E. coli* cells (a) untreated; (b) and (c) after photocatalytic inactivation treatment for 2 h; and, (d) after photocatalytic inactivation treatment for 30 min. Reprint from [62].

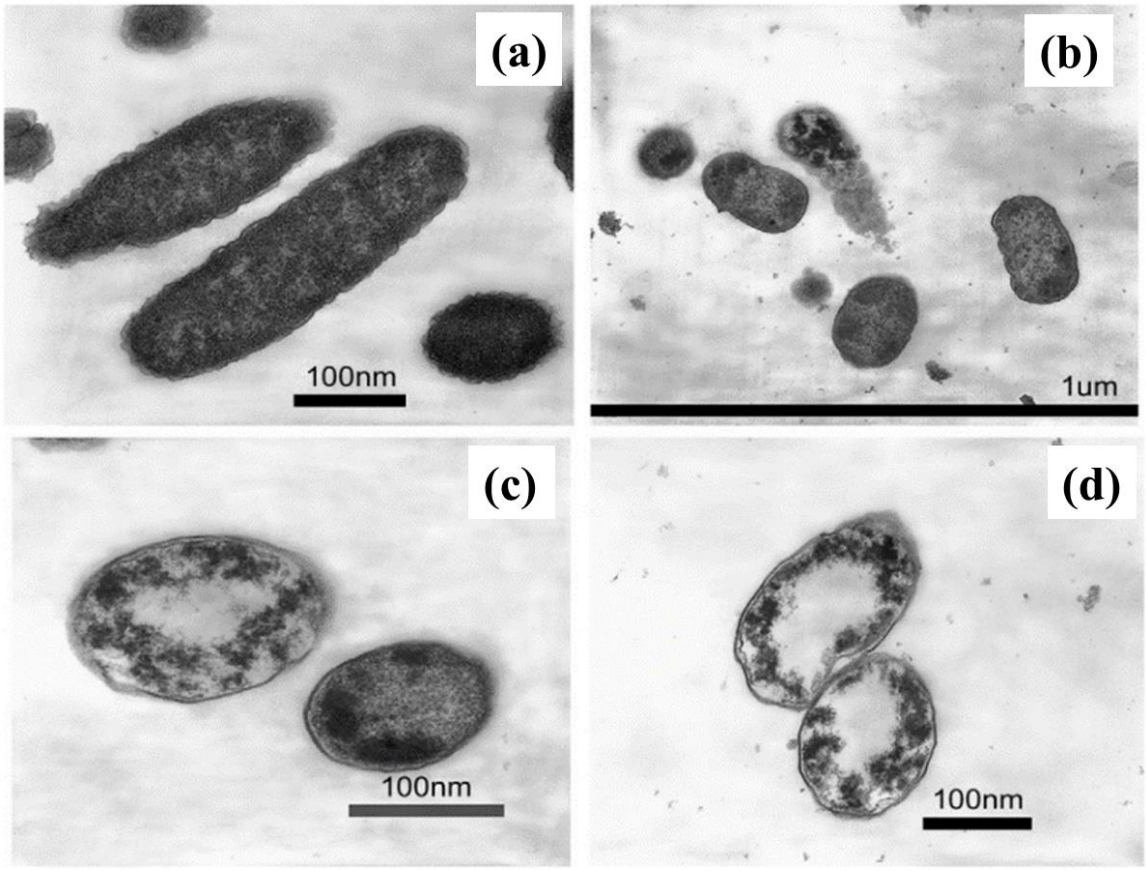

Figure 1.9. TEM images of *E. coli* (a) untreated; (b), (c), and (d) after photocatalytic inactivation treatment for 2 hrs. Reprint from [62].

It is pretty clear that the ROS affects the bacterial cells strongly. The ROS is chemically reactive oxygen forms radicals (e.g. $OH^{\bullet}$ and $O_2^{\bullet-}$) or reactive oxygen forms non-radical molecules (e.g. H_2O_2 and O_3). These ROSs are readily to take parts in the oxidation reactions. Thus, they are potentially toxic to bacterial cells. [63] The ROS can destroy the activities of metalloenzymes and the integrity of DNA in bacterial cells, forcing bacteria to protect themselves with scavenging enzymes and repair systems. [64] In the model of *E. coli*, the cell damage caused by ROS is lead through different steps. The autoxidation of redox enzymes (such as the oxidation of $FADH_2$ (flavin adenine dinucleotide accepted two electrons and two protons) on flavoproteins) leads to continuous hydrogen peroxide (H_2O_2) and superoxide ($O_2^{\bullet-}$) formation. Enzymes such as

catalases, peroxidases, and superoxides dismutases would work to minimize the accumulation of these two oxidants. However, both ROSs can damage [4Fe–4S] dehydratases and mononuclear iron enzymes. On the other hand, H_2O_2 also reacts directly with the unincorporated Fe^{2+}, which is linked with other biomolecules such as DNA. The resultant damage of DNA requires the action of repair enzymes. Once the amount of ROS rises high enough to disable the enzymes, the metabolic pathways fail. Then the bacterial cell recovery cannot be completed. [64] The disabled enzymes are continuously repaired, so their steady-state activities represent the balance between damage and repair processes. As shown in **Figure 1.10**, inorganic nanoparticles can generate and affect the cells in different ways, both through internal and external activities. [63] Other than the photocatalysis, nanoparticles can also introduce ROS through different ways to interact with bacteria. In principle, the ROS generation mechanisms are similar but still differ from material to material. By introducing nanoparticles, ROS can be generated by chemical reactivity of material properties and impurities (crystal lattice, dissolution, Fenton reactions), and/or by direct physical interactions of the nanoparticles with biological redox-catalyzing subcellular structures. [63]

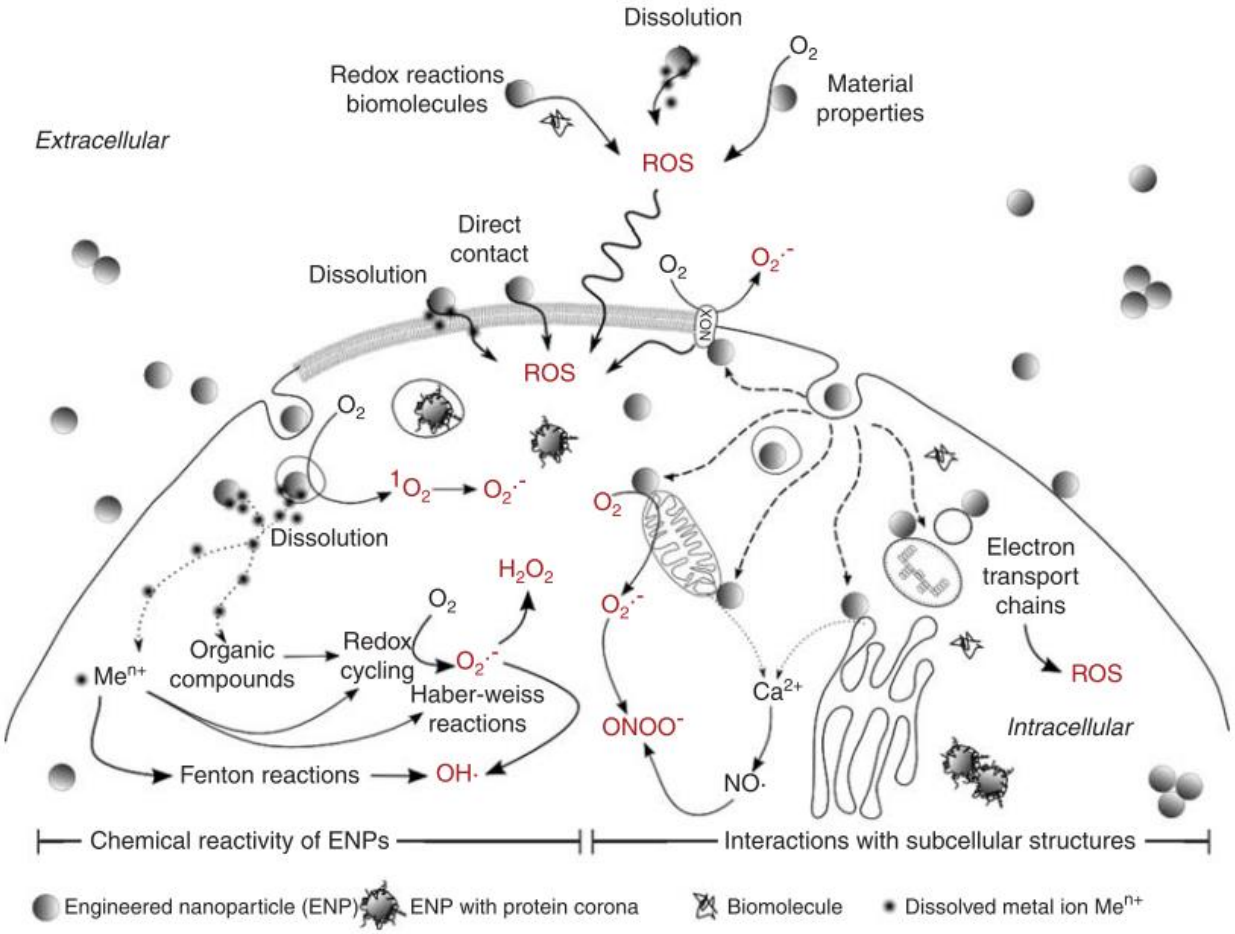

Figure 1.10. Illustration of cellular mechanisms of ROS generation by nanoparticles via extracellular chemical reactivity (top), intracellular chemical reactivity (left-hand side) or via physical interactions with subcellular compartments (right-hand side). Reprint from [63].

1.2.2.2 Metal nanoparticles

Because of the unique optical, electronic, and catalytic properties, metal nanoparticles such as Au, Ag and Cu are explored and can be used in many different areas. In particular, Ag and Cu nanoparticles are considered as novel antimicrobial nanomaterials due to their strong antimicrobial activities against different bacterial strains. [65] The antimicrobial mechanisms of metal nanoparticles are different from that of the photocatalysts. Here, Ag nanoparticles are chosen as a representative example to discuss the detail mechanism.

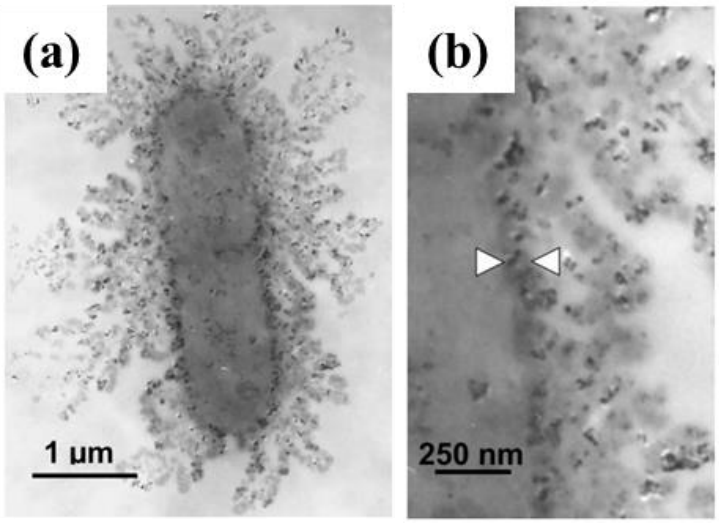

Figure 1.11. TEM images of (a) *E. coli* cell treated with 50 µg cm^{-3} of silver nanoparticles in liquid LB medium for 1 h. (b) Enlarged view of the membrane of this cell. Reprint from [66].

The antimicrobial properties of silver compounds have been used in many applications for years. [67] Now, since Ag nanoparticles have shown antibacterial activity even in the ultra-low concentrations, it has been more and more popular in the antimicrobial studies. The mechanism of the antimicrobial action of Ag nanoparticles is considered related to the amount of silver and the rate of silver released. [68] Thus, the antimicrobial activity of Ag nanoparticles is mainly contributed by the metallic Ag, the Ag ions, and the nano-sized particle. [69] The TEM images in **Figure 1.11** are *E. coli* cell treated with 50 µg/cm^3 of Ag nanoparticles (diameter ~ 12 nm) in liquid lysogeny broth (LB). It confirms that the Ag nanoparticles can invade into the cell and aggregate onto cell wall. And the zoomed-in TEM image shows that the integrity of the cell was compromised because of the treatment with Ag nanoparticles. [66] It is reported that the Ag nanoparticles can also generate ROS, such as OH^-, [70] and this process has also been considered as a primary mode of cytotoxic action of Ag nanoparticles. The high oxidative stress introduced by these Ag nanoparticles can lead to the cell inactivation. [69] On the other hand, the dissolution of the Ag nanoparticles introduces Ag ions (Ag^+) into the treatment system through different ways.

As shown in **Figure 1.12**, Ag ions (Ag^{+}) can be introduced by the surface passivation of the nanoparticle, the ligand replacement (by Ca^{2+}), oxidative dissolution, *etc*. The Ag ions process a very high affinity for organic amines, phosphates, selenol and most notably thiols, with which they forms a quasi-covalent bond. Ag ions can also work as the bridging agent between some of the thiols in bacterial cells to form chains and aggregations of the thiol bearing molecules. [71] So that the activities of a healthy bacterial cell can be disrupted. Surface properties of Ag nanoparticles have a crucial impact on their potency, as they influence both physical (aggregation, affinity for bacterial membrane, *etc*.) activities and chemical (dissolution, passivation, *etc*.) reactions. For example, smaller Ag nanoparticles have been demonstrated exhibiting better antimicrobial properties. [72]

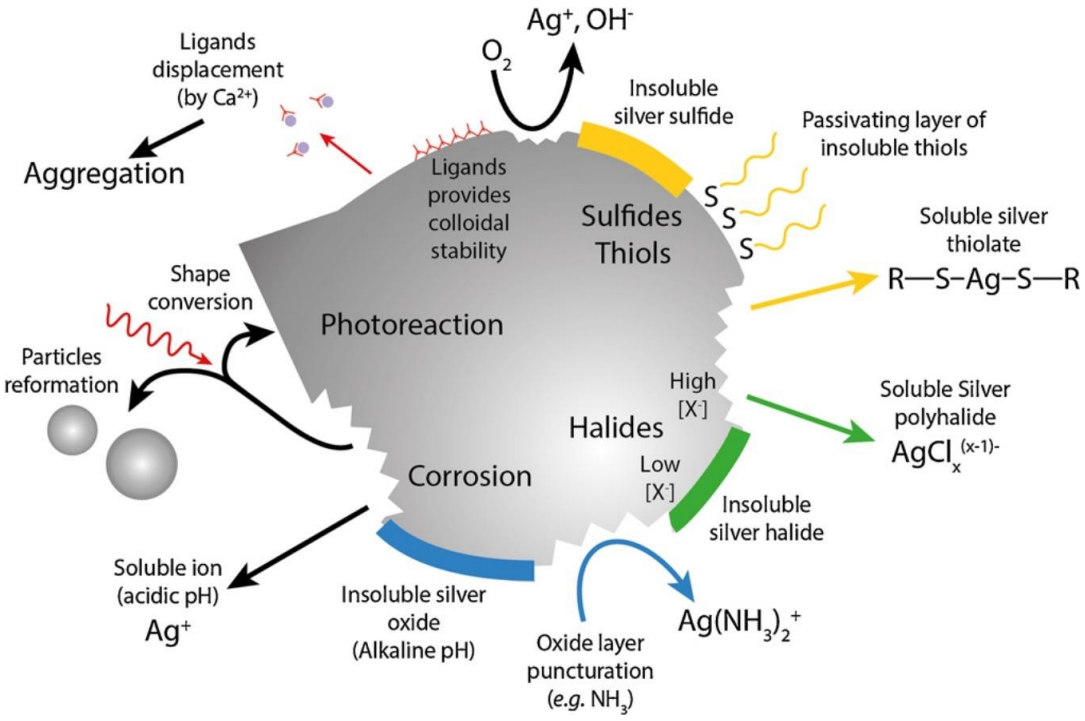

Figure 1.12. Illustration of several phenomena affecting Ag nanoparticles dissolution. Reprint from [69].

1.2.2.3 Metal oxides nanoparticles other than photocatalysts

Various metal oxides nanoparticles such as CuO, MgO, CeO_2, Co_3O_4 and ZnO are reported as effective antimicrobial materials both against the Gram-positive and the Gram-negative bacteria.[57] The underlying antimicrobial mechanisms of these particles are not fully understood yet, and the proposed mechanisms differ from each other. Overall, their antimicrobial activities depend on particle size and concentration. [57] Among all these materials, CuO and ZnO are the most studied materials. The antimicrobial properties of CuO and ZnO are mainly based on the ROS generation on the particle surfaces. And it is also reported that CuO nanoparticles can cross the bacteria cell membrane and then causing damages on enzymes of bacteria. [73] Here CuO nanoparticles are chosen to discuss their antimicrobial activities.

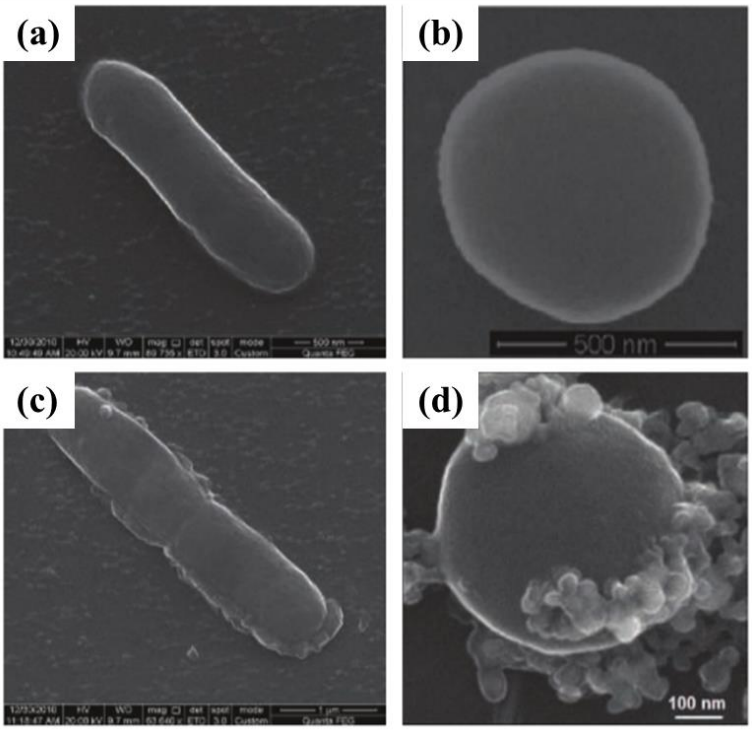

Figure 1.13. Environmental SEM images of CuO targeted bacterial cells. (a) *E. coli* and (b) *S. aureus* untreated cells after overnight growth; (c) *E. coli* and (d) *S. aureus* treated with CuO Nanoparticles. Reprint from [74].

From the environmental SEM images shown in **Figure 1.13**, the morphologies of the same type of bacterial cells are different when treated or untreated with CuO nanoparticles. [74] The treated cells show that the cell membranes and cell walls are damaged. More interestingly, the CuO nanoparticles can accumulate on the surfaces of the cells. The possible antimicrobial mechanisms are shown in **Figure 1.14**. The changes of the bacterial morphologies and inactivation after CuO treatment are demonstrated mainly because of ROS produced. The oxidative stress introduced by the ROS combined with the strong adherence of the CuO nanoparticles on the cell surfaces, the CuO nanoparticles are capable of breaking down the cell wall and cell membrane, then causing the leakage of the cell internal materials and cell death. [74]

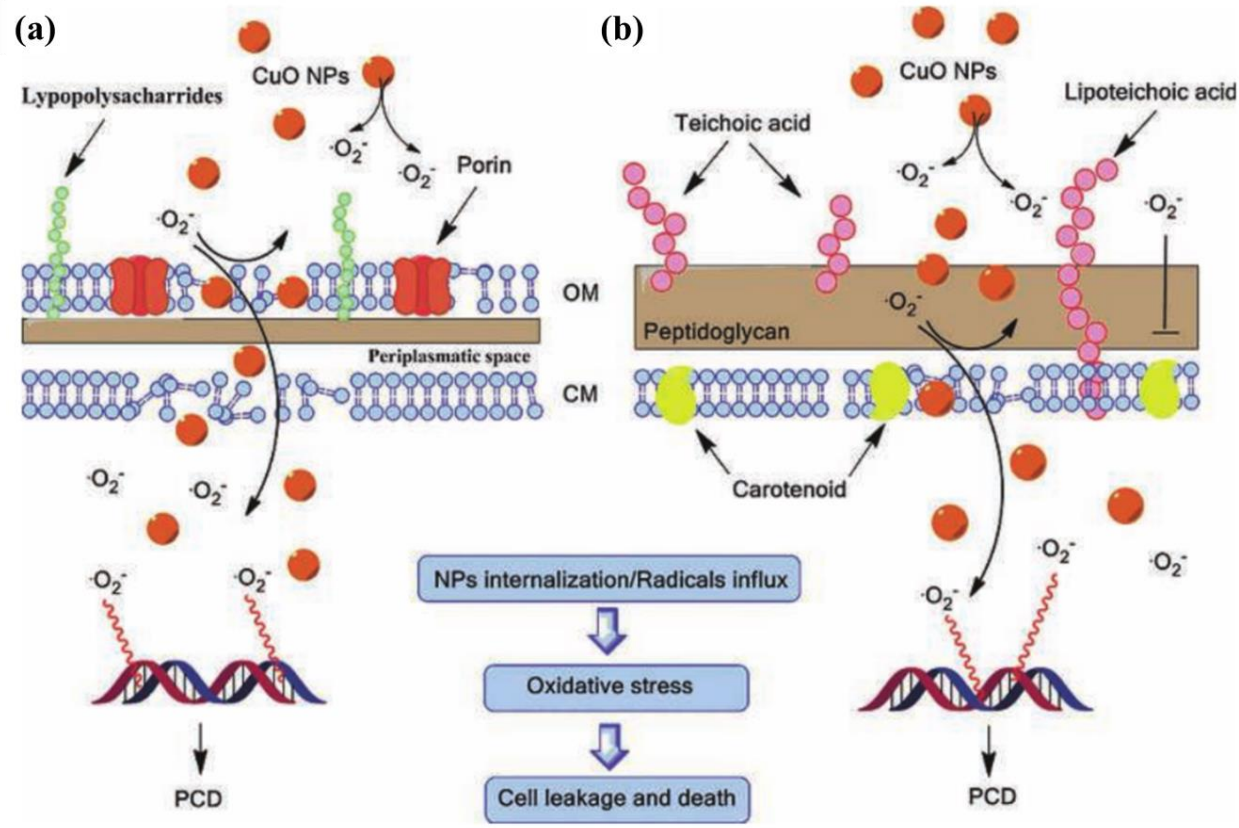

Figure 1.14. Illustration of the antibacterial mechanisms of CuO nanoparticles against (a) Gram-negative bacteria, and (b) Gram-positive bacteria. Reprint from [74].

Other than the activities mentioned above, it has also been found that the leaching of copper ions from CuO nanoparticles by bacterial amino acids is required for their antimicrobial toxicity. [75-76]

1.3 Contents of dissertation

This dissertation is devoted to study and explore new inorganic antimicrobial materials. It consists of six chapters.

Chapter 1 presents the background and development of the antimicrobial materials, especially inorganics. Different antimicrobial agents/ methods are discussed, mainly including the modern antimicrobial technologies based on nanomaterials. The antimicrobial mechanisms of different antimicrobial materials, such as antibiotics, photocatalysts and other inorganic nanomaterials are presented in detail.

Chapter 2 focuses on the experimental techniques used for the material synthesis and characterizations in this dissertation. The development and studies of traditional hydrothermal synthesis and the microwave assisted hydrothermal synthesis are mainly discussed. The material characterization techniques including Zeta-potential measurement, XRD, SEM, TEM, and UV-Vis tests are introduced.

Chapter 3 covers the study of the visible light driven photocatalytic activities of EDA [EDA = 2,2'-(ethylenedioxy)bis(ethylamine)] modified carbon dots. The dye degradation (against methylene blue, MB) and antimicrobial (against *E. coli*) activities of EDA-carbon dots are given.

Chapter 4 introduces the study of the visible light induced photocatalytic activities of $CuBi_2O_4$ nanostructures/microstructures. Five different $CuBi_2O_4$ samples are synthesized by a hydrothermal method. Their morphologies, crystal structures, and optical properties are

characterized. The photoelectrichemical (PEC), visible light induced dye degradation (against methylene blue, MB), and antimicrobial (against *E. coli*) activities are also measured and discussed.

Chapter 5 shows the study of a novel inorganic mixture antimicrobial material $Cu_xFe_yO_z$. Microwaved assisted hydrothermal synthesis method is used to synthesize the nanostructured $Cu_xFe_yO_z$. The morphologies, crystal structures, and dye degradation capabilities (both MB and methyl orange (MO)) of as synthesized samples are characterized. The antimicrobial activities against both the Gram-positive and the Gram-negative bacterial strains, including drug resistant strains, are also carried out. It is demonstrated that the $Cu_xFe_yO_z$ nanoparticles are a highly efficient antimicrobial material.

Chapter 6 briefly summarizes the dissertation and presents the future work.

CHAPTER 2

EXPERIMENTAL TECHNIQUES

2.1 Hydrothermal synthesis

Among numerous nanomaterial synthesis/ fabrication techniques, hydrothermal synthesis stands out as a facile, effective, and low cost method. The term of hydrothermal synthesis refers to the synthesis of materials by chemical reactions of substances in aqueous media above ambient temperature and pressure. [77] In another word, the hydrothermal processing is a heterogeneous reaction in the presence of aqueous solvents or mineralizers under high temperature and pressure, the materials that are relatively insoluble under ambient conditions can be dissolved and recrystallized during the chemical reaction. [78] It provides many advantages in the processing of advanced materials, which have great potential for various applications, such as catalysis, biomedical, energy storage, *etc*. As shown in **Figure 2.1**, various fundamental science and technologies branches can be directly benefited from, or linked with hydrothermal technique. The field of hydrothermal technology has gradually been applied from geo-technology to other fields, such as bio-technology and nano-technology due to its possibilities of processing new advanced nanomaterials. Clearly, the hydrothermal tree would not be limited to the branches shown in **Figure 2.1**, this technique will keep on expanding in the future to serve the interests from geologists, physicists, chemists, ceramists, engineers, biologists, and so on. [78]

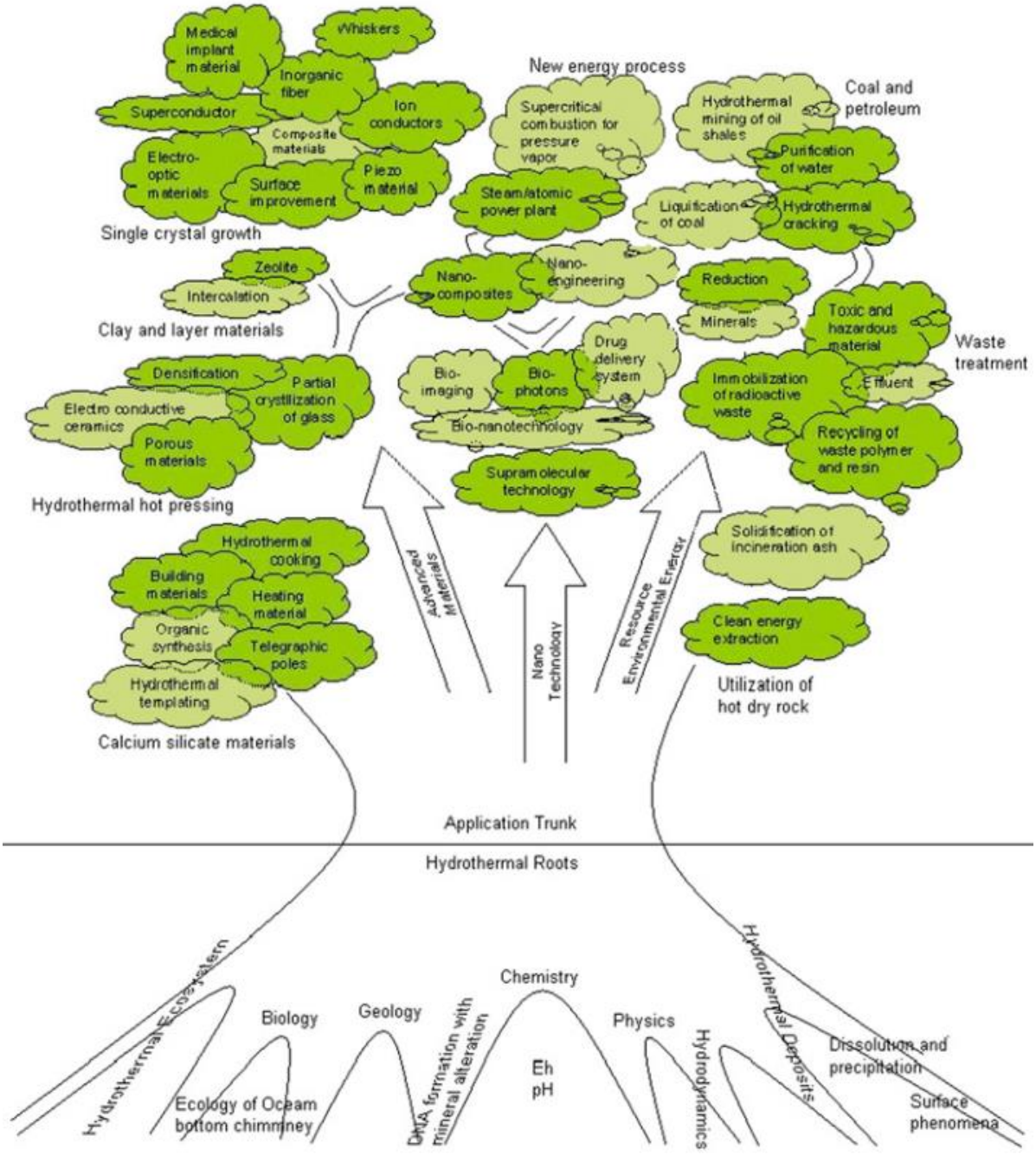

Figure 2.1. Hydrothermal tree showing different branches of science and technology. Reprint from [78].

2.1.1 A brief history of hydrothermal synthesis

As a fascinating fabrication method, hydrothermal synthesis has been initiated from the middle 19th century. [79] The first reported hydrothermal growth of crystals was performed by a geologist named Karl Emil von Schafhäutl in 1845 to fabricate microscopic quartz crystals.[80] Followed by this, the hydrothermal synthesis of various metal oxides began. Commercial application of the hydrothermal technique started in 1908 when K.J. Bayer leached bauxite mineral under hydrothermal conditions to obtain aluminum. [81] In 1982, the first International Hydrothermal Symposium was held at Japan. It brought scientists from different research areas together to promote the further development of hydrothermal technique. [82] Since then, the hydrothermal method became more and more popular in the processing of a wide range of materials, from the bulk material to mesoscopic materials with sizes all the way down to nanoscale with various morphologies.

2.1.2 Hydrothermal synthesis in the development of material science

Due to the specific physical and chemical properties of solvents used in hydrothermal synthesis, different types of reactions for advanced materials can be achieved. Some typical applications of hydrothermal synthesis are listed below.

(a) Synthesis of new crystal phases of new materials.

(b) Crystal growth of different inorganic compounds from one pot to complexes.

(c) Design of materials with desired size and morphology for specific applications.

(d) Decomposition, alternation, corrosion and etching of the bulk materials.

Table 2.1 Comparison of different metal oxides synthesis methods. [82-83]

Parameter	Solid state reactions	Co-precipitation	Sol–gel	Hydrothermal
Cost	Low to moderate	Moderate	High	Moderate
State of development	Commercial	Demonstration/commercial	Research & Development	Research & Development/ demonstration
Composition	Poor	Good	Excellent	Good/excellent
Morphology	Poor	Moderate	Moderate	Good
Purity	<99.5 %	>99.5 %	>99.9 %	>99.5 %
Calcination step	Yes	Yes	Yes	No
Milling step	Yes	Yes	Yes	No

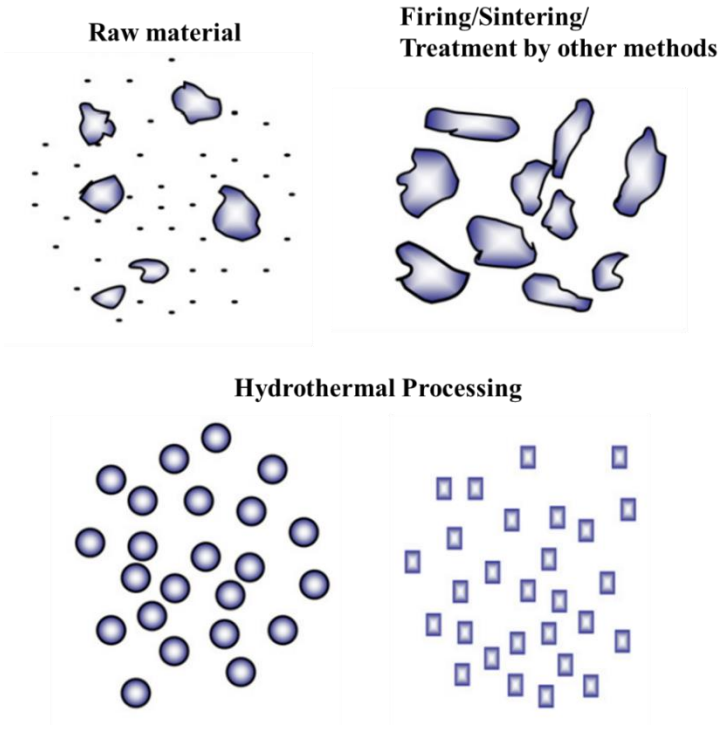

Figure 2.2. Difference in particle processing by hydrothermal and conventional techniques. Reprint from [78, 84].

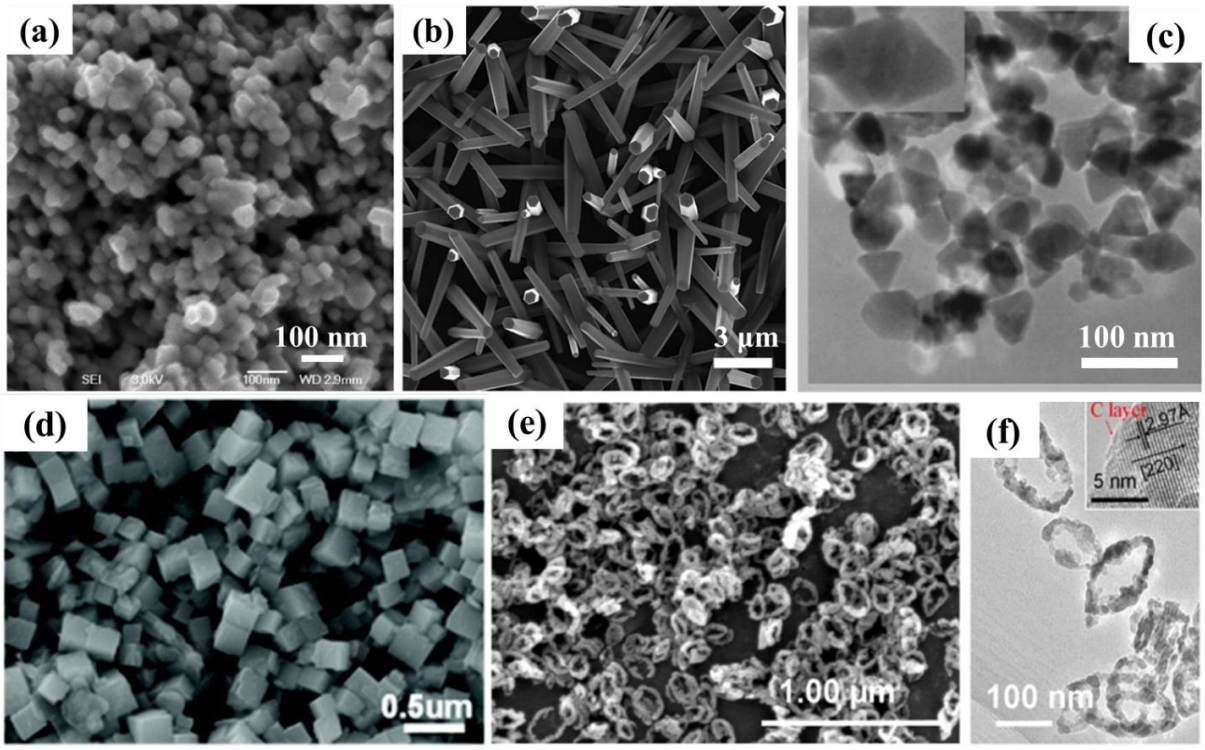

Figure 2.3. Examples of nanomaterials fabricated through hydrothermal synthesis. (a) Monodisperse Fe_3O_4 nanoparticles. Reprint from [85]. (b) ZnO nanowires. Reprint from [86]. (c) ZnO nanotriangles. Reprint from [87]. (d) $KTi_2(PO_4)_3$ nanocubics. Reprint from [88]. (e-f) Fe_3O_4 /C core-shell nanorings. Reprint from [89].

Comparing to other metal oxides synthesis methods, such as solid state reactions, co-precipitation, sintering, firing and sol-gel methods, hydrothermal method shows better control over the composition, morphology, and size of the as-synthesized products (**Table 2.1**, **Figure 2.2**). The excellent control over the crystal structures of the products from hydrothermal synthesis does not require other extra processing steps such as calcination and milling. [82] For example, Wang *et al*. have fabricated α- and β-MnO_2 single crystal nanowires through hydrothermal synthesis. [90] Without expensive equipment, catalysts, or templates, high purity MnO_2 nanowires have been obtained through the low temperature synthesis route. With further development, numerous well defined nanostructures have been synthesized by hydrothermal method. As the SEM images shown in **Figures 2.3 (a)** to **(f)**, uniform Fe_3O_4 nanoparticles,[85] ZnO nanowires,[86] ZnO nanotriangles,

[87] $KTi_2(PO_4)_3$ nanocubics [88] and Fe_3O_4 nanorings [89] have been obtained by hydrothermal methods. In the past decades, hydrothermal synthesis has been successfully used to fabricate materials for different applications, such as energy storage, microwave absorption, drug delivery and optical applications. [87-89, 91] For example, in the work of Meligrana *et al*., high surface $LiFePO_4$ nanomaterials have been synthesized by an easy, quick and low cost hydrothermal method as lithium-ion battery cathode. [92] These high surface area phospho-olivine $LiFePO_4$ nano-powders have shown capacities near the theoretical value. In the work of Yu *et al*., ZnO hollow spheres with porous crystalline shells have been synthesized by a one-pot hydrothermal method with of glucose and $ZnCl_2$ as precursors. [93] The as-fabricated ZnO hollow spheres have shown stable photocatalytic activity of degrading Rhodamine B (RhB), and have the potential in the applications such as solar cell, and catalysis. Mesoporous structures nowadays are also a popular studying subjects due to their ultra-high surface areas. They have attracted a lot of attentions in biomedical applications, for instance, drug delivery. [94-96] As shown in **Figure 2.4**, ordered uniform mesoporous carbon nanospheres (**(a)** – **(b)**) and strontium hydroxyapatite (SrHAp) nanorods (**(c)** – **(d)**) can be both fabricated through hydrothermal synthesis. More interestingly, by using a novel low-concentration hydrothermal approach, the obtained mesoporous carbon nanospheres shown in **Figure 2.4 (a)** and **(b)** are with uniform diameter and body-centered cubic $Im\bar{3}m$ symmetry. And they are low-toxic to cells and the cell permeability is excellent. The mesoporous SrHAp nanorods shown in **Figures 2.4 (c)** and **(d)**, also fabricated by hydrothermal method, have shown self-activated luminescence at room temperature and they are potential candidates as drug carriers with controlled release. [96]

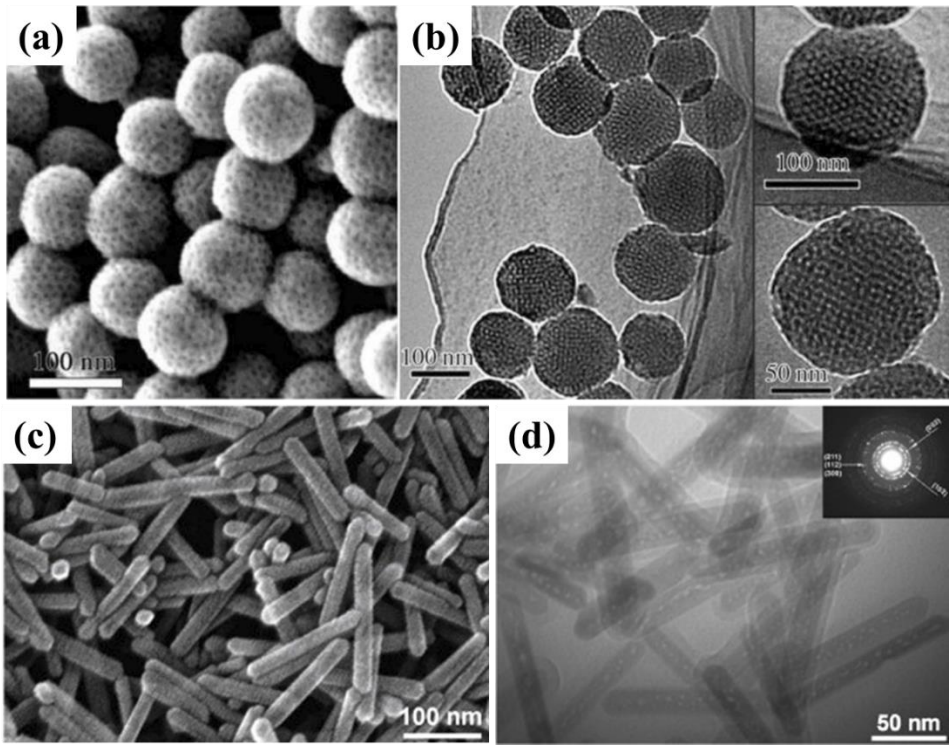

Figure 2.4. Mesoporous nano-structures fabricated through hydrothermal synthesis. (a) and (b) Mesoporous carbon spheres. Reprint from [94]. (c) and (d) Mesoporous strontium hydroxyapatite nanorods. Reprint from [96].

In addition to the precursors used, the synthesis temperature and pressure, the hydrothermal synthesis is also controlled by the solvent. The fundamental understanding of the hydrothermal nowadays are mainly about the behavior of the solvent (such as the pH value, viscosity, density, and so on) under the synthesis conditions. Thermodynamic studies, such as solubility, stability dissolution-precipitation studies help us understand more about the chemistry under hydrothermal conditions. However, so far, the crystallization process under hydrothermal conditions is still not fully understood yet. In recent years, the thermochemical modeling and prediction of the chemical reaction under hydrothermal conditions have been attracted lots of attentions. The thermodynamic models make it possible to select effective and inexpensive precursors, and suitable reaction conditions to achieve a high yield hydrothermal synthesis. [97-98] For example, in the work of

Lencka *et al.*, a comprehensive thermodynamic model has been developed to predict the hydrothermal synthesis of pure phase strontium zirconate. [98] As shown in **Figure 2.5**, the calculated phase stabilities under 25^{o}C and 160^{o}C are compared in (a) and (b). The stability of ZrO_2 under acidic conditions is higher at 160^{o}C than that at 25^{o}C. However, under alkaline conditions, the temperature effect is small. [98]

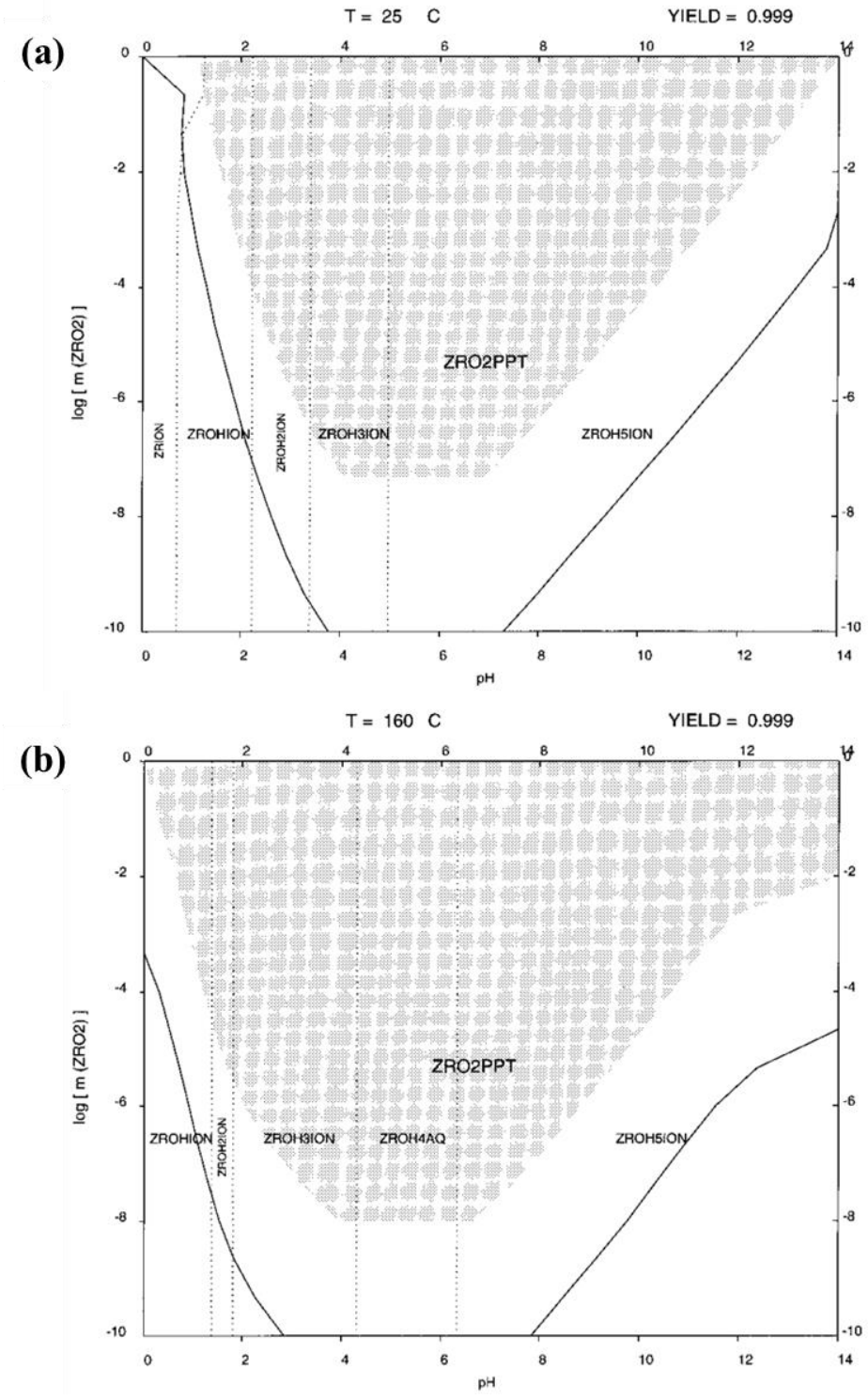

Figure 2.5. (a) Calculated phase stability and yield diagram for the Zr hydrothermal system at 298 K. (b) Calculated phase stability diagram for the Zr hydrothermal system at 433 K. The symbols ZRO2PPT, ZROHION, ZROH2ION, ZROH3ION, ZROH4AQ, and ZROH5ION denote ZrO_2(s), $ZrOH^{3+}$, $Zr(OH)_2^{2+}$, $Zr(OH)_3^{+}$, $Zr(OH)_4$(aq), and $Zr(OH)_5^{-}$, respectively. Reprint from [98].

2.1.3 Hydrothermal synthesis equipment

The definition of the hydrothermal synthesis tells us that it requires a pressure vessel capable of containing a highly corrosive solvent at high temperature and pressure.[78] The hydrothermal synthesis experimental configuration in our lab is shown in **Figure 2.6**. As shown **Figure 2.6(a)**, the forced air electric oven (Fisherbrand™ Isotemp™) is used to create an environment with a constant desired temperature, which can be in the range of 50 ^{o}C to 250 ^{o}C. **Figure 2.6(b)** shows a set of stainless steel hydrothermal reactor (autoclave) for the synthesis. The stainless steel holder of the autoclave help to maintain the appropriate pressure condition required in chemical reactions when sealed. The autoclave liner is made by the Teflon inert material, which can be stable till about 260 ^{o}C. It ensures that the chemical reactions would not be affected by the degrading of the reactor liner.

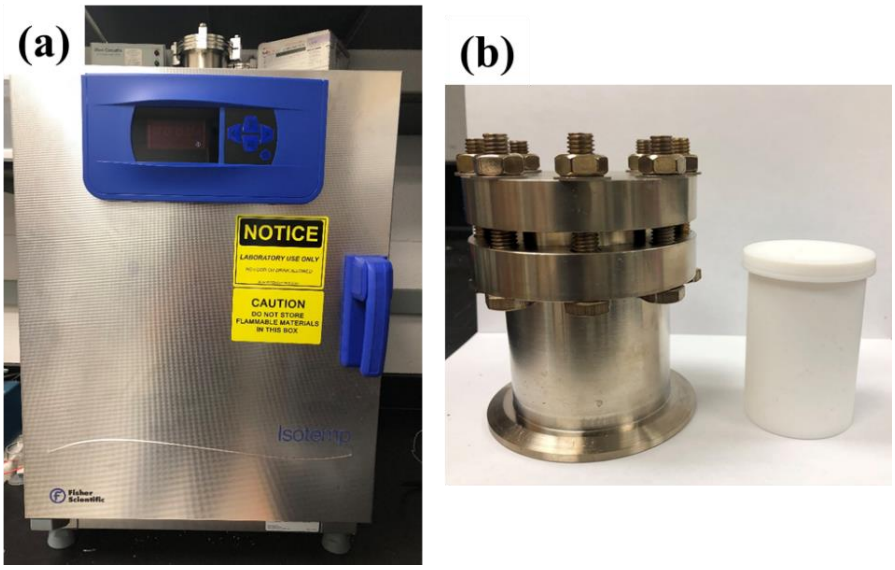

Figure 2.6. The experimental configuration for general hydrothermal synthesis. (a) An electric oven with wide temperature range: 50 ^{o}C to 250 ^{o}C. (b) Stainless steel autoclave with Teflon liner.

2.2 Microwave assisted hydrothermal synthesis

The first report of using microwave ovens for synthesis in modern chemistry was in 1986, and after then it becomes an indispensable tool. [99] Numerous papers of microwave assisted synthesis are reported in the past decades. **Figure 2.7** shows a comparison of conventional and microwave heating assisted chemical reactions. [100] The use of microwave heating has brought many benefits to the chemical synthesis, such as dramatically reduced processing time, increased yield, increased efficient and higher product purity, and better product properties. [101]

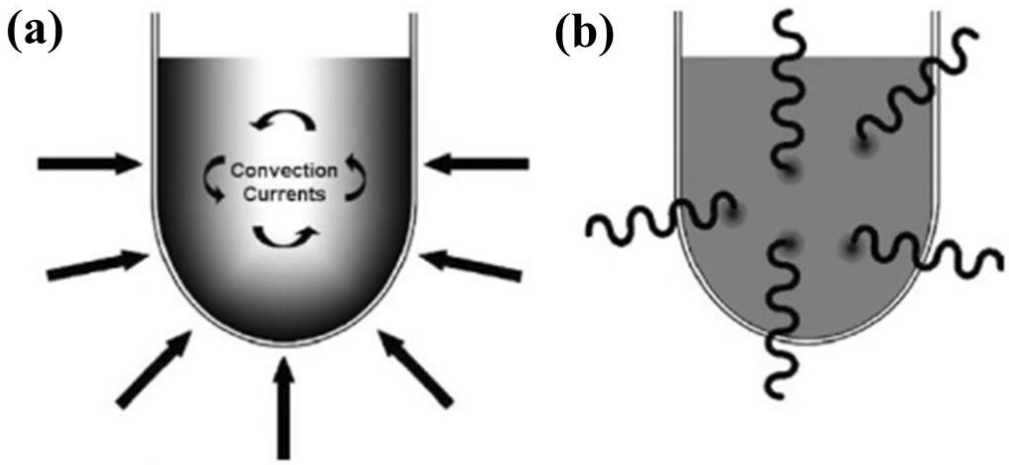

Figure 2.7. (a) Conventional heating. (b) Microwave heating. Reprint from [100].

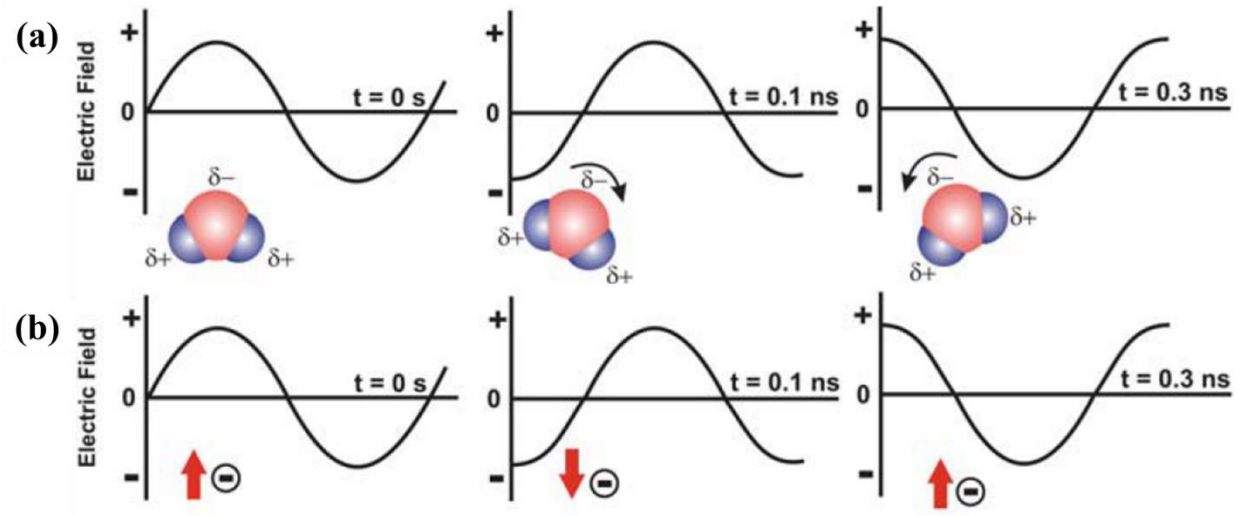

Figure 2.8. Two main heating mechanisms under microwave irradiation: (a) dipolar polarization; (b) ionic conduction. Reprint from [99, 102].

2.2.1 Fundamental of microwave assisted synthesis

Microwaves are electromagnetic radiation with frequencies in the range of 0.3 to 300 MHz. [103] This irradiation can heat up the solvents mainly by two main mechanisms, dipolar polarization and ionic conduction, based on polar/nonpolar solvent or conductive solvent. [101] The heating process is dependent on the characteristics of a particular solvent. [100, 102] As shown in **Figure 2.8(a)**, for the dipolar polarization, the microwave irradiation can result in the alignment of the molecular dipoles of the solvent in the applied electric field. [99] With the oscillation of the electric field, the molecular dipoles then would try to re-align along the alternating electric field. During this process, the applied energy can be lost in the form of heat from molecular friction of the solvent molecules and also dielectric loss. Depending on the time scales of the orientation and disorientation phenomena relative to the frequency of the irradiation, different amounts of heat can be produced. [99] If the dipole does not have enough time to realign (high-frequency irradiation) or reorients too quickly (low-frequency irradiation) with the applied field, no heating will occur. [101] For the ionic conduction (**Figure 2.8(b)**), the microwave irradiation can result alignment of

the ions in the electric field. [99] With the oscillation of the ions caused by the microwave irradiation, more collisions will happen between neighboring molecules or atoms. These collisions then can cause agitation or motion of these molecules or atoms, which eventually results in heating. These ion conductivity heating provides a stronger heat-generating capacity than the dipolar rotation mechanism. However, these effects are only particularly evident in the case of ionic liquids under microwave irradiation. [100-101, 104-105]

2.2.2 Microwave assisted hydrothermal synthesis in nanotechnology

Microwave assisted hydrothermal synthesis can provide a better control in crystal phase, size, shape, topology and composition for the products. [101]

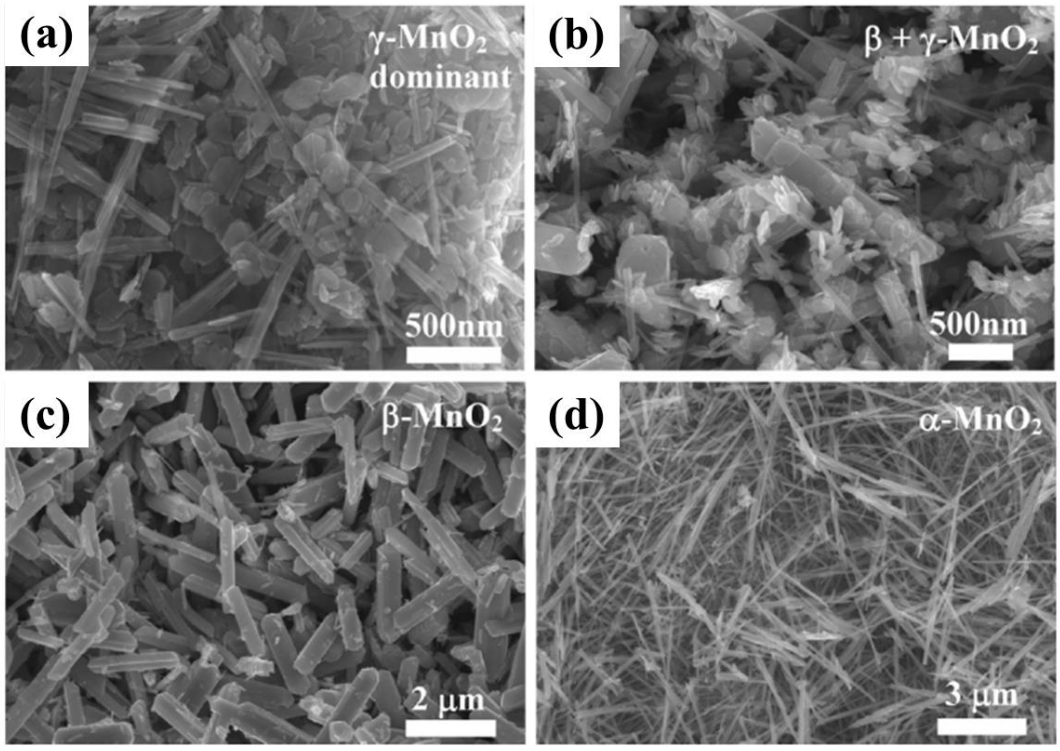

Figure 2.9. SEM images of MnO_2 samples fabricated by microwave−hydrothermal synthesis. (a) γ-MnO_2 + trace β-MnO_2, (b) β- MnO_2 + trace γ-MnO_2, (c) β-MnO_2, and (d) α-MnO_2. Reprint from [106].

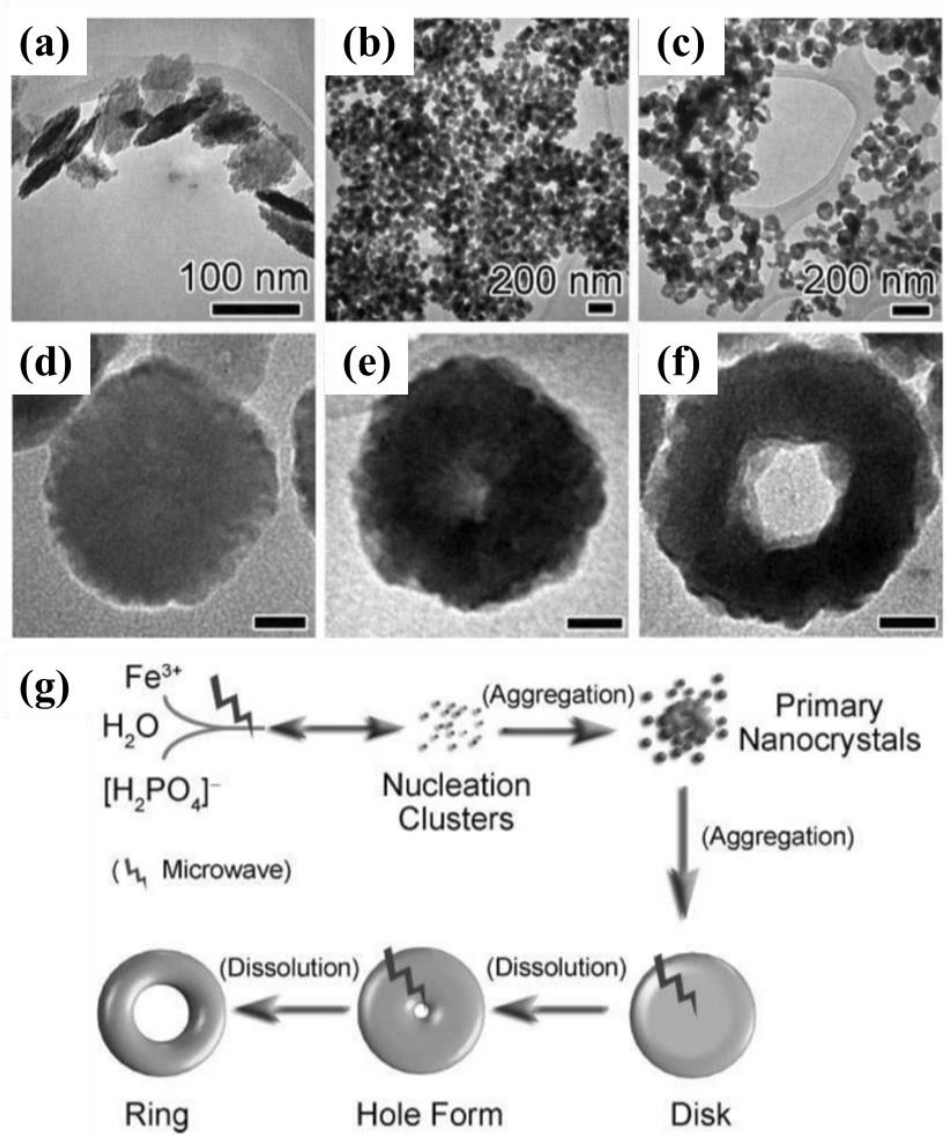

Figure 2.10. Morphology evolution of the α-Fe_2O_3 fabricated by microwave assisted hydrothermal synthesis: TEM images of the products obtained at 220 °C after (a) 10 s, (b) 50 s, and (c) 5 min; High-magnification TEM images of individual disk-like α-Fe_2O_3 with (d) no hole after 50 s, (e) a small hole after 100 s, and (f) a large hole after 25 min. Scale bars in (d)- (f): 20 nm. (e) Schematic illustration of α-Fe_2O_3 nanoring formation through microwave assisted hydrothermal synthesis processes. Reprint from [107].

As shown in **Figure 2.9**, through the microwave assisted hydrothermal synthesis, the crystal phases of MnO_2 can be tuned. The morphologies of α-, β-, and γ-MnO_2 also can be varied from rods, plates to wires. [106] Another example of the control of α-Fe_2O_3 nanorings morphologies

fabricated by microwave assisted hydrothermal synthesis is shown in **Figure 2.10**. With the increasing exposure time to the microwave irradiation, a hole can be gradually formed and expanded in the center of the disk-like α-Fe_2O_3, which eventually would form a nanoring structure after 25 min irradiation. [107] Similar to traditional hydrothermal synthesis, microwave assisted hydrothermal synthesis is applied to fabricated advanced materials for different applications. For example, Wang *et al*., have fabricated a graphene based Au-TiO_2 by microwave assisted hydrothermal method. [108] The product has shown efficient H_2 generation under visible light illumination. In the work of Qi *et al*., a microwave assisted hydrothermal method has been used to fabricate hydroxyapatite hierarchically porous hollow microsphere (**Figure 2.11**). [109] The obtained porous hollow nanostructures consist of nanosheets/nanorods as the building blocks, which have shown high drug (ibuprofen) loading capacity and high protein adsorption ability. [109]

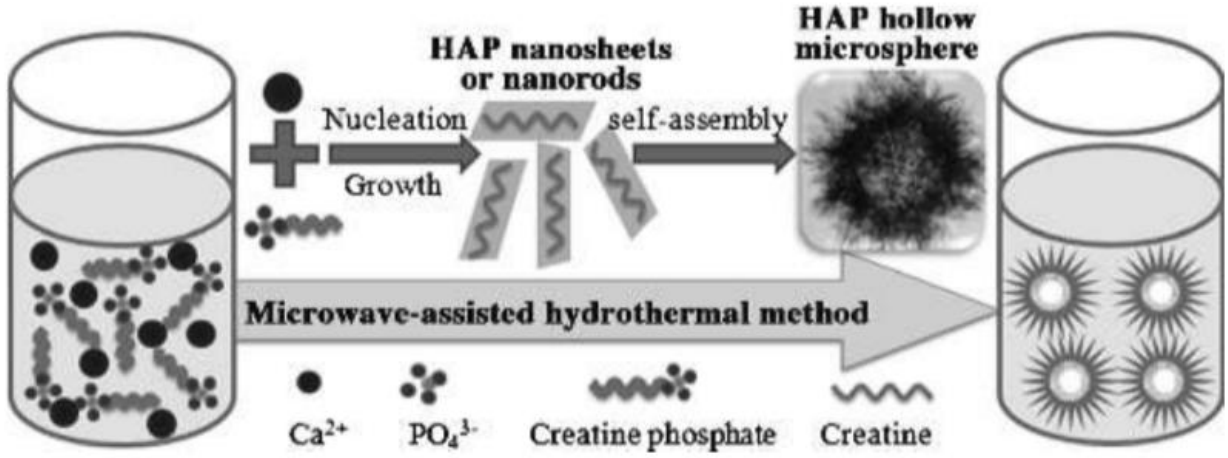

Figure 2.11. Illustration of the microwave assisted hydrothermal method for the fabrication of hydroxyapatite hierarchically nanostructured porous hollow microspheres. Reprint from [109].

2.2.3 Microwave assisted hydrothermal synthesis equipment

Figure 2.12(a) shows a commercially available microwave reactor (Anton Parr Monowave 400) used in our lab, which can provide 850 W unpulsed microwave output. It is equipped with a built-in IR sensor, a fiberoptic sensor, a magnetic stirrer and a camera, which allow in-situ access to the measurementd of temperature and pressure, and even the real-time visual observation of the reaction. **Figure 2.12(b)** shows a 10 ml silicon carbide (SiC) reaction vessel and a 10 ml glass vessel. The SiC vessel is highly corrosion resistant, and the glass vessel allows the microwave interact directly with the reaction reagents. By choosing different solvents, the synthesizing conditions can be varied in a large range. This system can be operated under maximum 30 bar pressure. And the IR temperature can hold up to 300^{o}C.

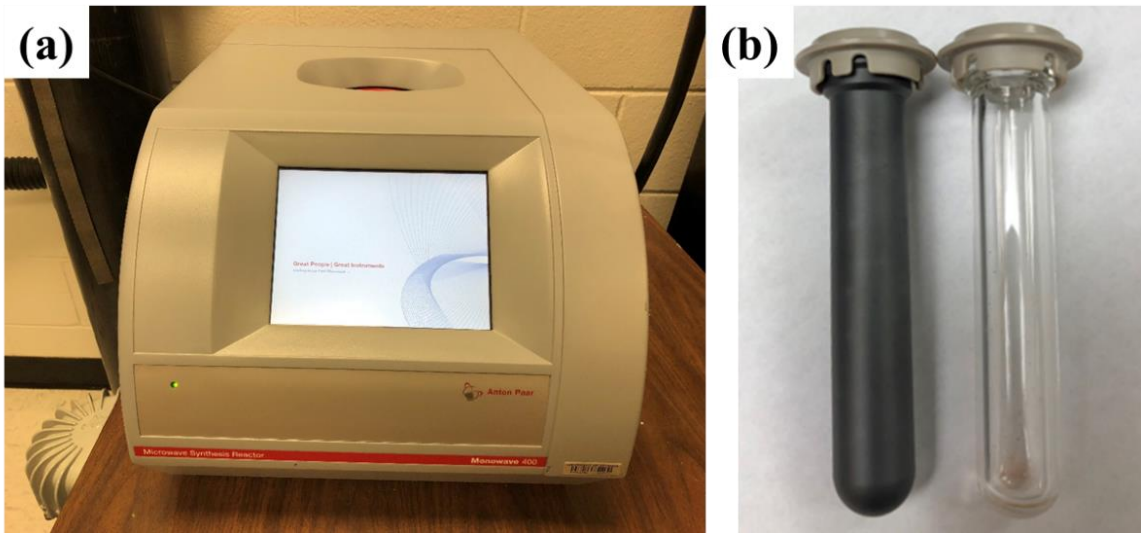

Figure 2.12. The experimental configuration for microwave assisted hydrothermal synthesis. (a) A microwave reactor. (b) A 10 ml SiC reaction vial and a 10 ml glass reaction vial.

2.3 General characterization techniques

For the studies of advanced materials, the characterizations of the as-synthesized materials are important. For example, as mentioned in Chapter 1, an effective photocatalyst requires specific metal oxides phases with proper bandgap energy for utilizing light with different wavelength, the size of the photocatalyst also affects the recombination of the photo-generated electron–hole pairs and the charge transportation distance. Thus, the general characterization methods of the morphology, size, surface property, structure, composition and optical property for the following chapters are discussed as follows.

Morphologies of the samples have been investigated by a field-emission scanning electron microscope (FESEM) equipped with an energy dispersive X-ray spectroscopy (FEI Inspect F). Transmission electron microscopy (TEM)/scanning transmission electron microscope (STEM) analysis and corresponding selected area electron diffraction (SAED) have been carried out using a Hitachi HF-3300 TEM/STEM at 300 kV to further investigate the morphologies and atomic structures of the products. For the electron microscopes, the imaging relies on the interaction between the electron beam and specimen. When an energetic electron strikes the specimen, scattering will occur. The scattering signals can reveal information on the specimen's composition, topography, and crystallography. SEM mainly utilizes the information from the back-scattered electrons and secondary electrons to image the sample. The characteristic X-rays produced during the interaction of electron beam and the sample provides the composition information of the sample. On the other hand, TEM mainly collects the elastically scattered transmitted electrons for imaging and electron diffraction.

The crystal structures of all the as-prepared samples have been characterized by an X-ray diffractometer (XRD; PANalytical X'Pert PRO MRD) with a Cu Ka source (λ = 1.5405980 A) at

45 kV and 40 mA. The diffraction angle scanning range is from 15° to 70° at an angular step of 0.02°. For the fundamental understanding, the crystalline atoms can cause a beam of incident X-rays to diffract into many specific directions. The XRD records the angles and intensities of these diffracted beams to generate an XRD pattern of the sample. On the XRD pattern, the peak shape and width tell the information of the crystallinity, the crystallite size and orientation, strains, and defects of the sample. Locations of diffraction peaks are related to *d*-spacings of lattice planes (related to the size and shape of the unit cell). Relative intensities of diffraction peaks can yield information about the arrangement (atomic position) of atoms in the crystal structure. The fundamental rule of XRD is the Bragg's Law. L. Bragg and W.H. Bragg discovered that the X-ray diffraction could be treated as reflection from evenly spaced planes if monochromatic X-ray radiation was used. In Bragg's Law (**Equation 2.1**), the incoming X-rays are scattered specularly from each crystal plane of the sample. If the path difference for reflection from successive crystal planes is $n\lambda$, then diffraction can occur.

$$2d\sin\theta = n\lambda\,, \tag{2.1}$$

where n is an integer, λ is the X-ray wavelength, d is the spacing between planes, and θ is the diffraction peak angle.

The optical properties of the samples have been characterized by analyzing the UV-Vis transmittance, extinction (absorption and scattering) and diffuse reflectance absorption. The UV-Vis transmittance and extinction of the suspension samples are recorded by a double-beam UV-Vis spectroscopy (JASCO V-570). The fundamental principle for such a measurement is the Beer–Lambert law, where the optical absorbance A of a sample is linearly dependent on the optical depth l and concentration c of the sample,

$$A = \alpha lc\,, \tag{2.2}$$

where α is the molar extinction coefficient, l is the light path length, and c is the concentration of the sample/suspension. The diffuse reflectance absorption spectra of the powder samples are measured by a Shimdzu 2450 UV-Vis spectrometer. To determine the optical band gap energies of a semiconductor, a Tauc plot is used, where $(\alpha h\nu)^{1/r}$ is plotted against the light energy $h\nu$ (here h is the Plank constant and ν is the frequency of light). Here the value of r depends on the type of semiconductor materials. Usually, $r = 1/2$ for a direct-band gap semiconductor and $r = 2$ for an indirect-band gap semiconductor.

Zeta potential of the samples have been measured by a Malvern Zetasizer Nano ZS system at 25^{o}C. The zeta potential is caused by the net electrical charge contained in the interfacial double layer. And it is a measure of the magnitude of the electrostatic or charge repulsion/attraction between particles.

CHAPTER 3

VISIBLE LIGHT ACTIVATED ANTIMICROBIAL FUNCTIONS OF CARBON QUANTUM DOTS

3.1 Introduction

As discussed in Chapter 1, bacterial infections present a major healthcare challenge, especially with the increasing bacterial resistance to antibiotics, [110-111] demanding the development of alternative antimicrobial strategies. Visible light activation considerably broadens the reach of the photochemical antimicrobial agents, enabling potentially their uses under solar irradiation or natural light exposure to inhibit the growth of pathogens and other infectious agents. Our focus has been on exploring the newly developed carbon "quantum" dots, or more appropriately called carbon dots for the lack of the classical quantum confinement behavior,[112] for their visible light-activated bactericidal functions.

Carbon dots (**Figure 3.1**),[112] generally defined as small carbon nanoparticles with various surface passivation schemes,[113] have emerged as a new class of quantum dot-like nanomaterials, with their optical properties and photocatalytic functions resembling those found in conventional nanoscale semiconductors.[113-119] For example, in addition to their bright and colorful fluorescence emissions, carbon dots have been demonstrated as effective visible-light photocatalysts for oxidation and reduction reactions.[119-120] The same photoinduced redox processes responsible for the photocatalytic activities should make carbon dots an excellent candidate as antibacterial agents, for which a major advantage is the broad and strong optical

absorption of carbon dots over the visible spectral region, extending into the near-infrared (IR). Here we report the experimental confirmation on the antimicrobial activities of photoexcited carbon dots. EDA-carbon dots [EDA = 2,2'-(ethylenedioxy)bis(ethylamine)] were selected for their being compact in structure (referring to structurally compact and very small in the overall size) and well-characterized (optical and morphological properties, and NMR) in previously reported study.[121] The evaluation of the antimicrobial properties of EDA-carbon dots were performed under household LED lighting or ambient laboratory light conditions, and the results showed that carbon dots inhibited *E. coli* cells in different experimental settings. These results and their mechanistic implications were discussed in this chapter.

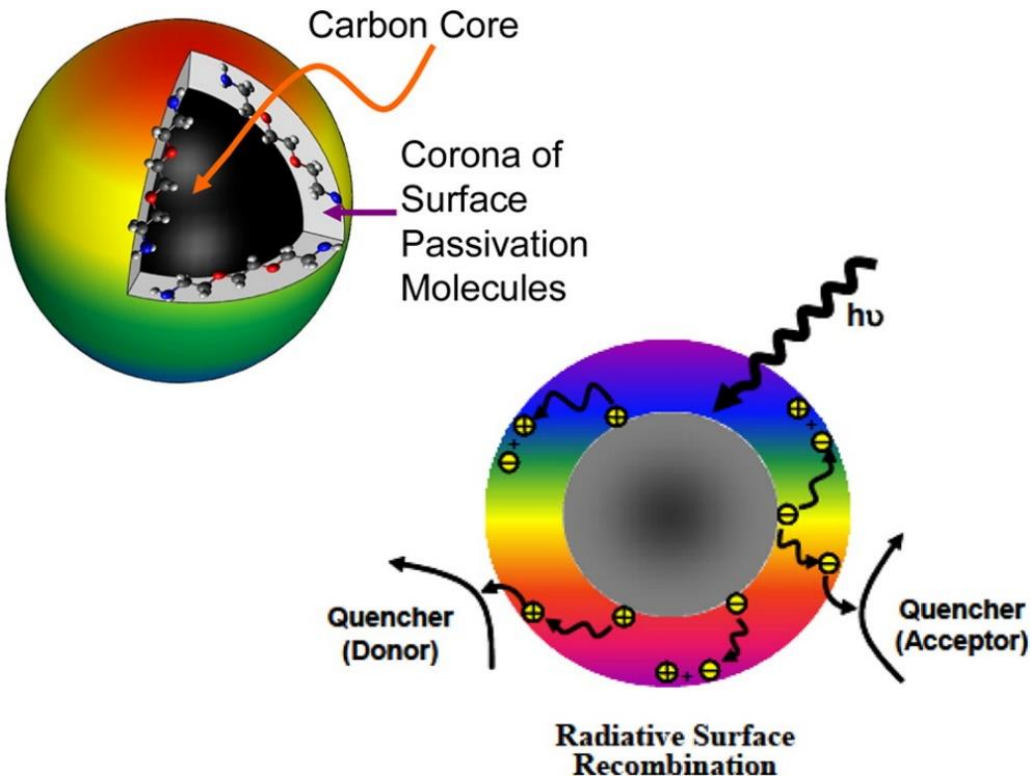

Figure 3.1. Cartoon illustrations of (left) a carbon dot, with a small carbon nanoparticle core and the surface functionalization molecules forming a soft shell; and (right) the photoexcited state species and processes, with the rainbow color showing fluorescence from the dot surface.

3.2 Experimental Methods

Carbon Dots. Carbon nanoparticles were used as the precursor for carbon dots synthesis. An as-supplied carbon nanopowder sample (1 g) was refluxed in an aqueous nitric acid solution (5 M, 90 mL) for 48 h. The reaction mixture was cooled back to ambient temperature and then dialyzed against fresh water for up to 3 days. The post-dialysis mixture was centrifuged at 1,000*g* to retain the supernatant, followed by the removal of water to obtain the desired carbon nanoparticle sample.

In the synthesis of the EDA-carbon dots using a previously reported procedure,[121] the carbon nanoparticle sample obtained from the processing above was refluxed in neat thionyl chloride for 12 h, followed by the removal of excess thionyl chloride under nitrogen. The post-treatment carbon nanoparticle sample (50 mg) was mixed well with carefully dried EDA (500 mg) in a flask, and heated to 120 ºC, and stirred vigorously under nitrogen protection for 3 days. The reaction mixture was cooled to ambient temperature, dispersed in water, and then centrifuged at 20,000*g* to retain the dark supernatant as an aqueous solution of the as-synthesized sample. The solution was dialyzed in a membrane tubing (cutoff molecular weight ~ 500) against fresh water to remove free EDA and other impurities to obtain the EDA-carbon dots in aqueous solution. For microscopy characterization only, the EDA-carbon dots were very lightly coated with gold by visible-light irradiation of the solution with $HAuCl_4$ for a few minutes.[122]

Photocatalytic Dye Degradation. The photocatalytic dye degradation activities against methylene blue (MB) of the EDA-carbon dots samples were carried out with a 250 W Halogen light at an intensity of ~ 65 mW/cm^2. In the test, 1.5 ml EDA-carbon dots with a concentration of 1.0 mM were mixed with 1.5 ml MB solution with a concentration of 30 μM. The degradation of

the MB molecules was recorded by the UV-Vis spectra a desired time interval after exposing to the Halogen light.

Light-Activated Antimicrobial Functions. Three different sets of antimicrobial experiments were performed. For one set of experiments, *E. coli* (K-12) cells were cultured in fresh nutrient broth overnight, and optical density (OD) values at 600 nm (OD600) of these cultures were measured and then standardized to 1 OD/mL. The bacteria suspension at 0.2 OD/mL per well was inoculated in a 12-well plate. Four treatment groups with different concentrations of carbon dots at 0.25 μM, 0.50 μM, 1 μM, and 2 μM were exposed under light in a safety cabinet for a time period t = 0, t = 15, t = 30, and t= 60 min, respectively. Then, the 12-well plate was incubated at 37 °C for 21 h. The OD600 of each well was recorded, and the readings were standardized to that of the T = 0 control plate.

In another set of experiments, fresh grown *E. coli* (K-12) cells in nutrient broth (Fisher Scientific, Pittsburgh, PA) were washed three times and then re-suspended in deionized water. With the use of 96-well plates, to a well was added a bacteria-carbon dots mixture (150 μL), in which the bacteria concentration was fixed at 1.0×10^6 CFU/mL and the concentration of carbon dots was varied (triplicates for each concentration). The plates were either exposed to visible light (12 V 36 W light bulb) or kept in dark for 30 min. The solutions in the wells were then transferred to 1.5 mL centrifuge tubes, followed by centrifugation at 8,000 rpm for 5 min. The supernatants were discarded, and the bacterial pellets were washed with deionized water twice. The cells were re-suspended in 500 μL nutrient broth, with 150 μL distributed into the wells of a 96-well plate for incubation at 37 °C. The growth of the carbon dots-treated bacterial cells and that of the untreated cells (as controls) were monitored by measuring the OD values at 595 nm (OD595) at various time points on a Spectra Max M5 spectrophotometer (Molecular Devices, LLC,

Sunnyvale, CA).

For the viable cell number determination by using the traditional plating method, the suspended *E. coli* cells post-treatment with various concentrations of the carbon dots were centrifuged and washed twice. The cells were re-suspended in phosphate-buffered saline (PBS), and series dilutions were made with PBS. Aliquots of 100 μL appropriate dilutions were surface-plated on Luria-Bertani agar plates (Fisher Scientific, Pittsburgh, PA), and the plates were incubated at 37 °C for 24 h. The number of colonies was counted, and the viable cell numbers of the treated samples and the controls were calculated in CFU/mL.

Last, *E. coli* (Top 10) stock culture was activated in fresh trypticase soy broth (TSB) at 37 °C overnight. The bacteria culture (1 mL) was washed twice by a combination of centrifuging at 4,000 rpm and re-suspended into sterile PBS. The resulting cell suspension was 10-fold serially diluted in PBS. For the detection of cell concentration, aliquots of 100 μL dilutions were plated onto TSB agar (TSA) plates, and incubated at 37 °C overnight before counting. Separately, the *E. coli* suspension (50 μL) at a concentration of 1.3×10^3 CFU/mL was mixed with aqueous solution of EDA-carbon dots (50 μL) at a concentration of 1 mg/mL. The mixture was then plated onto TSA plates, which were exposed to LED light (Osram Sylvania LED A19 lamp, ~10 mW/cm^2) for up to 6 h, along with the dark control (without light exposure), light control (without carbon dots), and negative control (no carbon dots and no light). The carbon dots-treated plates with the light exposure and all control plates were incubated at 37 °C for 24 h before counting to determine the viable cell numbers.

All experiments were performed in triplicates or more. Statistical analysis of experimental results was performed using Student *t* test, with $P < 0.05$ considered as significant difference.

3.3 Optical properties, morphologies, and photocatalytic dye degradation

3.3.1 Optical properties and morphologies

Carbon nanoparticles as precursor to carbon dots were obtained from the commercially supplied carbon nanopowder sample by following an established protocol including the refluxing of the as-supplied sample in an aqueous nitric acid solution, dialysis, centrifuging to retain the supernatant, and then drying to recover the carbon nanoparticles. The nanoparticles were surface-functionalized with 2,2'-(ethylenedioxy)bis(ethylamine) (EDA) under amidation reaction conditions to yield EDA-carbon dots.[121, 123] The EDA-carbon dots solution appeared optically transparent (**Figure 3.2**), stable without any precipitation over an extended period of time (many months). The solubility and solution stability may be expected for these dots being small carbon nanoparticles with the surface well-functionalized by hydrophilic molecules (**Figure 3.1**). According to results from atomic force microscopy and transmission electron microscopy characterizations, the EDA-carbon dots were on the order of 5 nm in diameter (**Figure 3.3**).

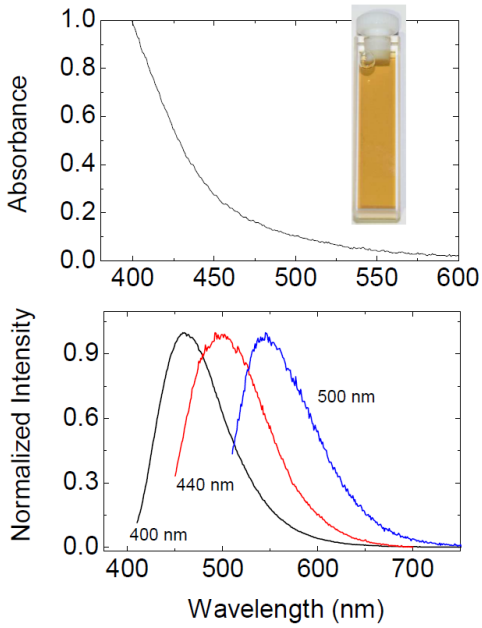

Figure 3.2. Top: The absorption spectrum of the EDA-carbon dots in an aqueous solution (photo in the inset). Bottom: Fluorescence spectra of the EDA-carbon dots in an aqueous solution excited at the indicated wavelengths.

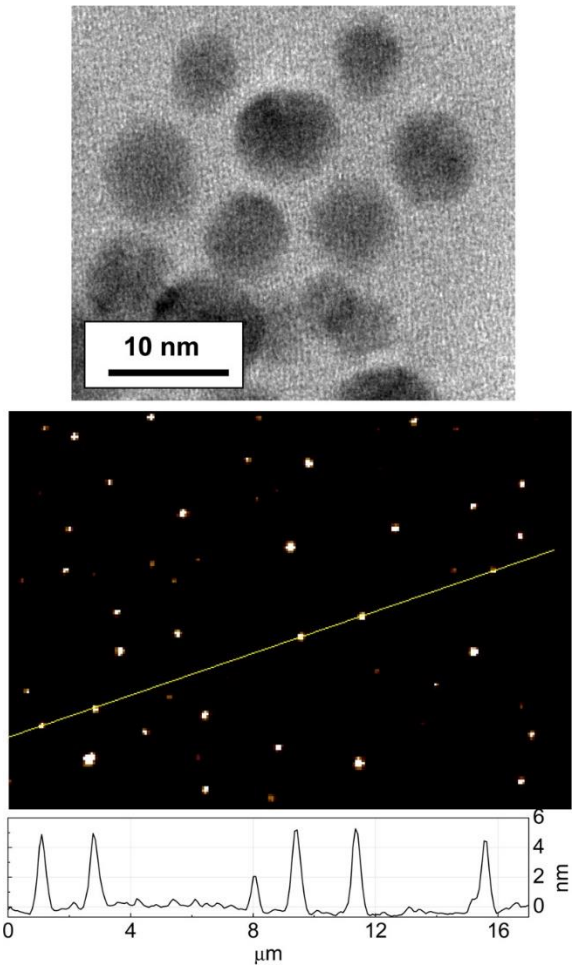

Figure 3.3. TEM (top) and AFM (bottom) images of the EDA-carbon dots on commercial TEM grid and mica, respectively.

The optical absorption of carbon dots is due to π-plasmon transition in the carbon nanoparticle core, with a broad absorption spectrum covering most of the visible region (**Figure 3.2**). The carbon dots in aqueous solution are brightly fluorescent, with the emission colors dependent on the excitation wavelengths (**Figure 3.2**), which along with the broad fluorescence spectra suggests a distribution of emissive excited states. It is known in the literature that the fluorescence emissions of carbon dots could be quenched effectively with either electron donors or acceptors, supporting the notion that the redox characteristics in the photoexcited states of carbon dots is responsible for their observed photocatalytic activities. [113, 124-125] The same

characteristics was exploited in this study for their visible light-activated antimicrobial functions.

3.3.2 Photocatalytic dye degradation

The photocatalytic activity of the EDA-carbon dots was firstly characterized by the MB degradation. As shown in the UV-Vis spectra in **Figure 3.4** (Right), with the exposure to the light illumination, the MB absorption at λ = 664 nm kept decreasing, which indicates the decomposition of MB molecules. The normalized MB absorbance $\alpha(t)/\alpha(0)$ at λ = 664 nm is shown in **Figure 3.4** (Left), where $\alpha(t)$ and $\alpha(0)$ are the absorbance at time t and t = 0 for different samples during the photodegradation process. The absorbance data can be fit into a first-order exponential decay equation,

$$\frac{\alpha(t)}{\alpha(0)} = e^{-\kappa t} \tag{3.1}$$

where κ is the photodegradation rate. The photodecay rate is estimated as κ = 0.307 ± 0.0002 h^{-1} with carbon dots concentraton at 0.5 μM.

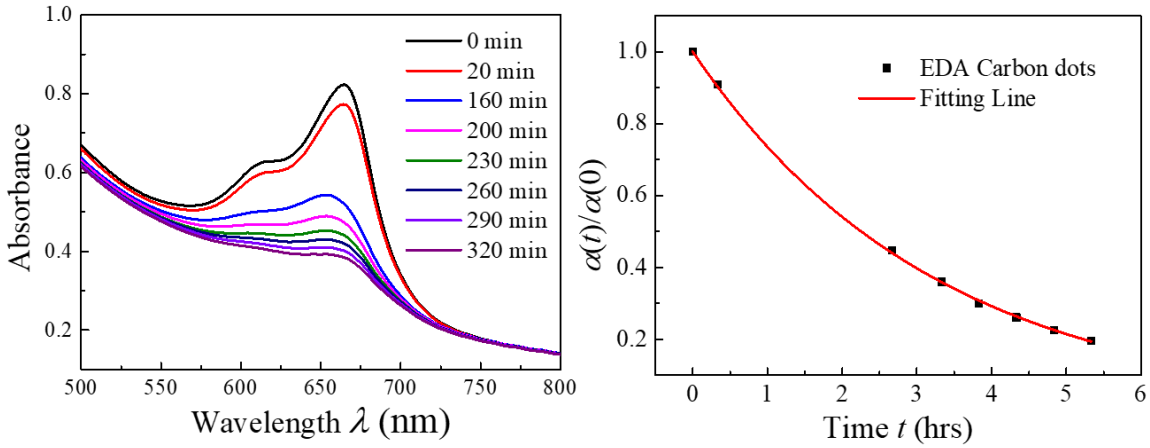

Figure 3.4. Left: The UV-Vis spectra of the MB (15 μM) – carbon dots (0.5 μM) mixture after light treatments. Right: The plot of the normalized MB absorbance α(*t*)/α (0) versus photodecay time *t* for EDA-carbon dots.

3.4 Antimicrobial activities

For the first set of antimicrobial experiments, as shown in **Figure 3.5**, the OD600 values of the *E. coli* K12 cells with or without carbon dots treatments clearly suggest that there were substantial antimicrobial effect of the EDA-carbon dots with light exposure on the *E. coli* cells. In the literature there was a report on some antibacterial activities of the carbon dots obtained from the carbonization of glucose and poly(ethyleneimine), with the dots quaternized with benzyl bromide before bacteria experiments.[126] While no deliberate light exposure was mentioned in that report, the ambient experimental conditions could have contributed to the reported observations.

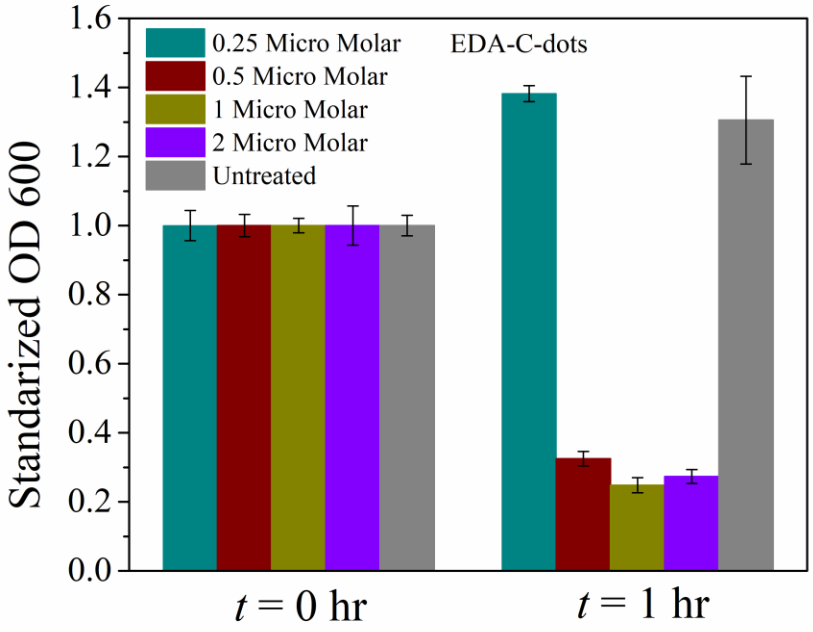

Figure 3.5. Photoinduced bacteria inactivation measured by OD600 for the EDA-carbon dots (presented as mean ± standard deviation of quadruplicate experimental results).

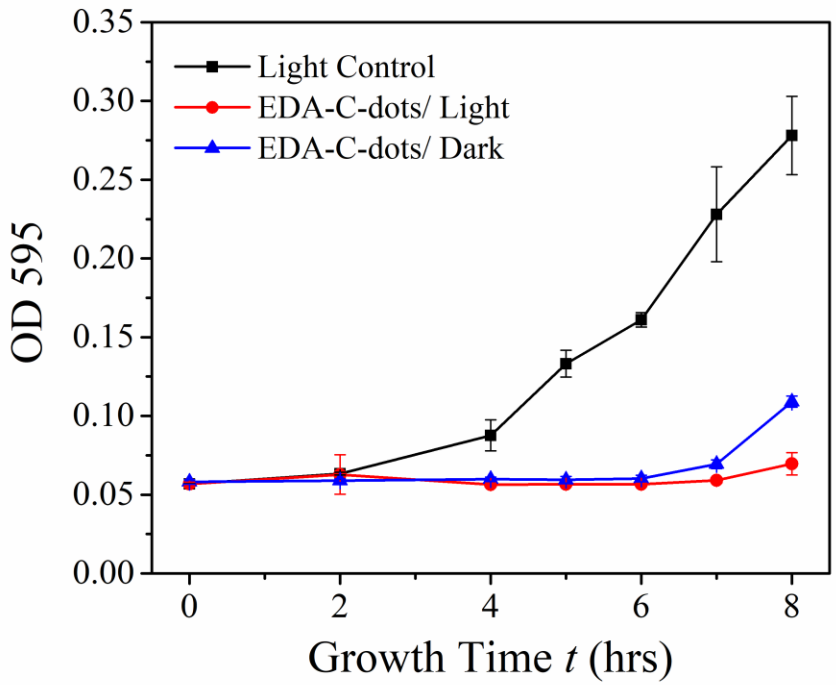

Figure 3.6. Growth curves of *E. coli* cells post-treatment with the EDA-carbon dots for 30 min with or without light, in terms of measuring OD595 values.

Figure 3.6 shows the growth curves of *E. coil* K12 cells in brain heart infusion (BHI) medium post-treatment with EDA-carbon dots, along with the control (untreated cells), based on OD595 values (the second set of antimicrobial experiments). The treated cells exhibited much prolonged lag phases (7-8 h) compared to the control, indicating that the EDA-carbon dots inhibited/inactivated the growth of bacterial cells. The effect was somewhat more pronounced (the lag phase longer by 1 h) when the treatment included exposure to visible light (**Figure 3.6**), but the difference of the light versus dark inhibition was not as obvious as what is shown in **Figure 3.5** (for which the experiments were performed in different laboratories at different times). Therefore, to address the inconsistency issue at the quantitative level for the OD measurement method, separate experiments with the same parameters and conditions were performed for the

inhibition effect probed by the more quantitative method of determining the viable cell numbers post-treatment.

Again the samples of *E. coli* with and without (control) the carbon dots were treated in the light box (12 V, 36W light bulb) or in the dark for 30 min. The viable cell numbers in the treated samples were determined, and according to the results shown in **Figure 3.7**, the EDA-carbon dots treatment coupled with visible light illumination was obviously effective for bacteria killing, with about 4 logs of *E. coli* cells killed. When compared to the results shown in **Figure 3.5**, the bacteria-killing effect seemed more dramatic in these experiments. A significant contributing factor might be the use of a lamp instead of ambient light for the photoexcitation of carbon dots, though more systematic and quantitative experiments are needed in further investigation. Nevertheless, the results are all consistent in terms of confirming the visible light-activated bactericidal functions of EDA-carbon dots.

Figure 3.8 shows the experimental results performed on TSA plates. Upon the exposure of the plates to visible light (~10 mW/cm^2) for up to 6 h, there were obvious differences between the treated plate and the controls (**Figure 3.8**), again suggesting substantial bactericidal effect of carbon dots with visible light illumination. The plates were read for CFU counts, and according to the results, the photoexcited carbon dots were very effective to inactivate the growth of bacteria cells (**Figure 3.8**).

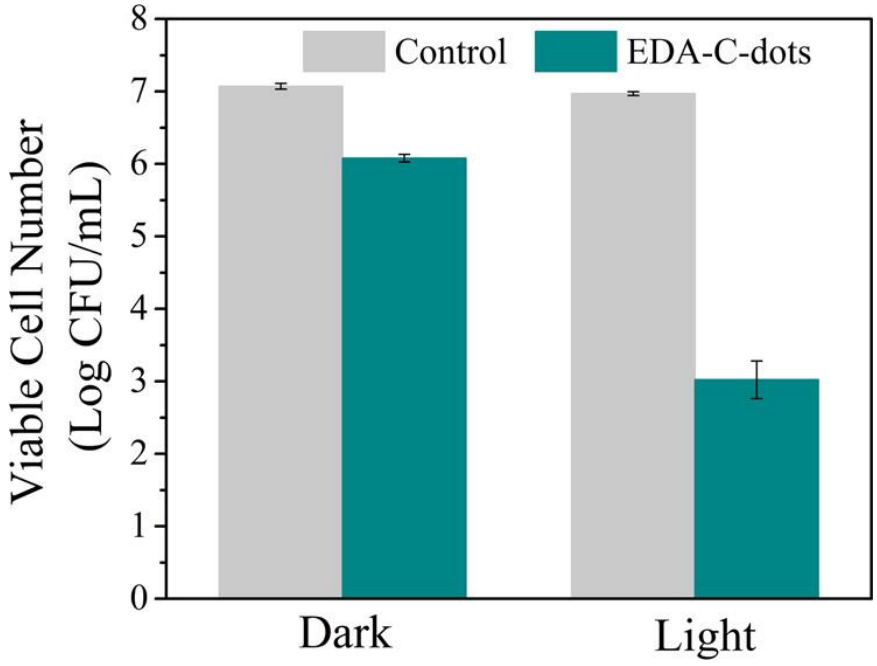

Figure 3.7. Reductions in the viable cell number after *E. coli* cells were treated with the EDA carbon dots for 30 min with or without light (presented as mean ± standard deviation of triplicate experimental results, and the data were also analyzed using the Student *t*-test with $P < 0.05$ as a significant difference).

The results presented above, which were obtained in different laboratories of the participating research groups under various experimental settings, provide consistent and unambiguous evidence for the highly effective bactericidal functions of carbon dots under visible light illumination, including even the common household lighting conditions. Mechanistically, carbon dots have been demonstrated for photodynamic effects on cancer cells,[127-128] and similar effects on bacterial cells might be a logical extension. The current mechanistic framework for the know optical properties of carbon dots is such that upon photoexcitation there are efficient charge separations for the formation of radical anions and cations (electrons and holes in a somewhat different description), which are "trapped" at various passivated surface sites. The radiative recombination of the redox pairs is responsible for the observed fluorescence emissions, with their associated emissive excited states of lifetimes on the order of a few nanoseconds. [129-

131] The redox species and emissive excited states could in principle be responsible for the observed bactericidal functions. However, in the fluorescence decay measurements, the rise time for the fluorescence was generally within the instrumental response function (1 ns or less), suggesting rather fast radiative recombination and short lifetimes of the radical ion species. Therefore, the emissive excited states are more likely being responsible for the photodynamic effects.

There have been no reports in the literature that explicitly describe the apparently effective bactericidal functions of photoexcited carbon dots. As related, there have been a few studies of using "graphene quantum dots" as photodynamic agents.[132-134] In the study by Ristic, *et al*., [132] antibacterial activities were observed with 470 nm light irradiation of the graphene quantum dots obtained from the electrochemical method. Those dots are essentially graphitic nanoparticles, which share similar optical properties with the precursor carbon nanoparticles for carbon dots. [118] However, the surface passivation of the carbon nanoparticles in carbon dots (or similarly in surface-passivated graphene quantum dots) substantially improves the optical properties, as often reflected in the much enhanced fluorescence emissions. [113, 118-119] Since the emissive excited states are likely responsible for the observed bactericidal functions, carbon dots with the more effective surface passivation and correspondingly more fluorescent are likely more desirable in serving as visible light-activated bactericidal agents for a variety of bacteria control applications. In further investigations, steady-state and kinetic studies that correlate optical properties of carbon dots, such as different fluorescence quantum yields and average lifetimes at various emission colors, with their antibacterial performance will be pursued.

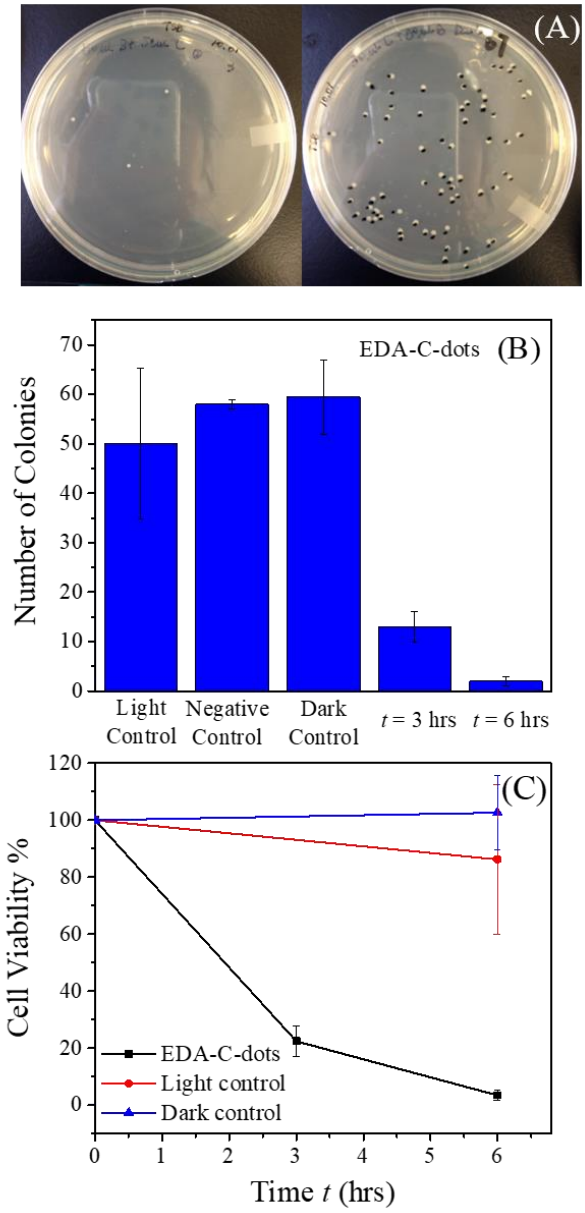

Figure 3.8. Photoinduced bacteria inactivation by the EDA carbon dots: (A) photographs showing colonies on TSA plates (left, 6 h treatment; right, dark control); (B) *E. coli* colony numbers; (C) cell viability ratio. The carbon dots were presented in the dark control.

3.5 Conclusions

The results obtained in this work, while more qualitative than quantitative in some of the experiments, demonstrate unambiguously that carbon dots can readily be activated by visible light (or even under ambient room light conditions) for significant bactericidal functions. The light

sensitivity of the carbon dots is apparently rather high to the degree that would require unusually stringent experimental conditions for the dark control, an issue to be examined more closely and quantitatively in further investigations. Also investigated will be the issues important to the quantification of the light-activated biocidal functions, including their correlations with the properties of carbon dots in various structural and surface configurations.

CHAPTER 4

VISIBLE LIGHT ACTIVITED ANTIMICROBIAL PROPERTIES OF HIERACHICAL $CuBi_2O_4$ BY A HYDROTHERMAL SYNTHESIS

4.1 Introduction

More recently, bismuth metal oxides have emerged as another promising narrow bandgap photocatalyst. The photocatalystic destruction of microorganisms with visible light irradiations by Bi_2WO_6, [135] AgBr-Ag-Bi_2WO_6 nanojunctions,[136] $Bi_2O_2CO_3$/Bi_3NbO_7 composites,[137] and Bi_2MoO_6–reduced graphene oxide composite nanoplates[138] have all been reported. However, compared to the reported Bi_2WO_6, Bi_2MoO_6, Bi_3NbO_7, *etc.*, copper bismuth oxide ($CuBi_2O_4$) is a p-type semiconductor with a narrow energy bandgap of 1.5 eV. [139] It also has suitable energy band positions to convert solar energy when compared to Cu_2O, CuO and Bi_2O_3 as illustrated in **Figure 4.1**. [139] Several groups have shown that $CuBi_2O_4$ can be used as a viable visible light driven photocatalyst. $CuBi_2O_4$/WO_3 can oxidize organic compounds into CO_2 efficiently under visible and UV light irradiation. [139] $CuBi_2O_4$/TiO_2 composites fabricated by *in-situ* sol-gel coating showed improved photocatalytic activity and adsorption performances under visible and UV light compared with pure $CuBi_2O_4$ and TiO_2.[140] Hierarchical $CuBi_2O_4$ microspheres and other microstructures synthesized by hydrothermal methods have been reported as a potential photoelectrode material for solar water splitting.[141-143]

In this chapter, we show that $CuBi_2O_4$ microstructures can be used as an efficient visible light active photocatalyst to kill bacteria. A facile hydrothermal method was used to synthesize

five $CuBi_2O_4$ hierarchical micro- and nano-structures. Their structural, optical, and photocatalytic performances were evaluated and compared. The hierarchical micro-flower $CuBi_2O_4$ samples showed the best antimicrobial performance as well as good solar-energy conversion into electrical energy under a solar simulator at a minimum external bias voltage and at a neutral pH value. The results demonstrate that the stable and non-water soluble $CuBi_2O_4$ microstructures are a promising material for future energy conversion and antimicrobial applications.

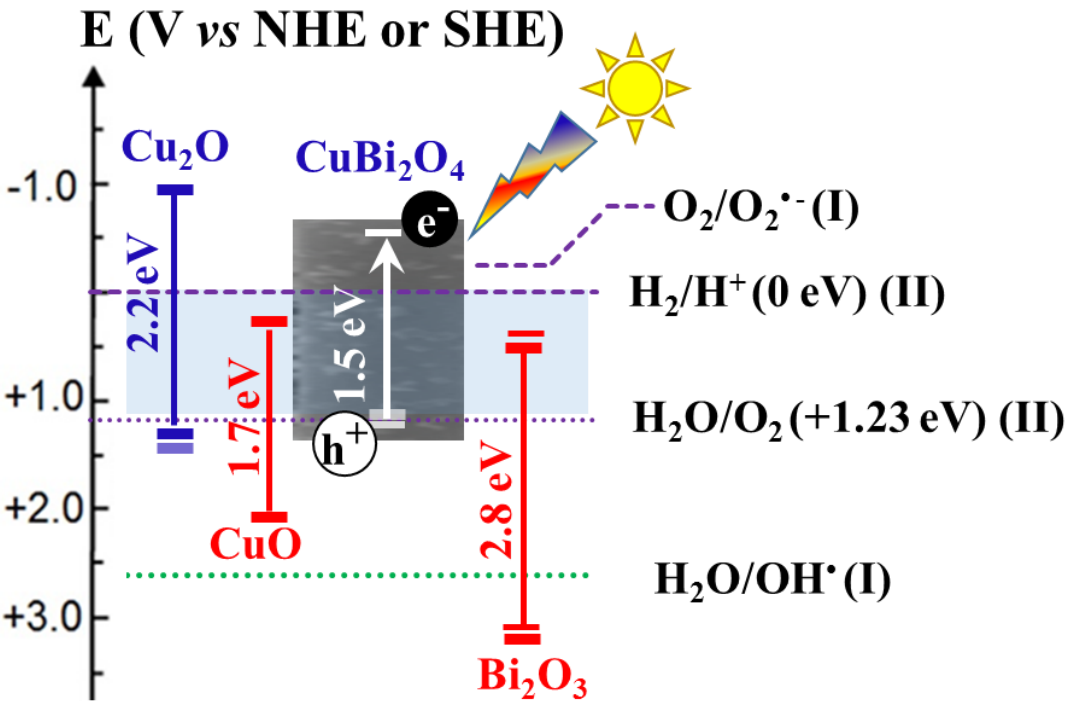

Figure 4.1. Schematics showing electronic potential diagram for Cu_2O, CuO, Bi_2O_3, and $CuBi_2O_4$ to compare (I) reduction/oxidation of organics and (II) solar-water splitting.

4.2 Experimental methods

$CuBi_2O_4$. In a typical synthesis process, $Cu(NO_3)_2 \cdot 3H_2O$ was dissolved in deionized water (DI water) (20 ml) to reach a concentration of 0.02 M. $Bi(NO_3)_3 \cdot 5H_2O$ was dissolved into DI water (20 ml) which contained 1 ml concentrated HNO_3 to achieve a Bi^{3+} concentration of 0.04 M. These two solutions were mixed thoroughly, then NaOH (20 ml) was added dropwise to the desired concentrations, as listed in **Table 4.1**. After stirring and sonicating for an additional 30 min, the mixture was further diluted by DI water and transferred into a 100 ml Teflon-lined autoclave, which was kept at 100 ^oC for 24 hrs. After cooling to room temperature, the products in the autoclave were collected by centrifugation, and then washed with DI water 3 times and dried in an oven at 70 ^oC overnight.

Table 4.1. Synthesis Conditions of different $CuBi_2O_4$ samples.

	C_{NaOH}	Solvent
A	2.40 M	H_2O
B	1.38 M	H_2O
C	1.18 M	H_2O
D	0.98 M	H_2O
E	2.40 M	H_2O / EtOH

Photocatalytic property. Photocatalytic properties of the samples were determined by the degradation of methylene blue (MB) with a 250 W Halogen light at an intensity of ~ 65 mW/cm^2. In each test, 15 mg of $CuBi_2O_4$ sample was dispersed into MB aqueous solution (15 ml, 30 μM). Prior to light irradiation, the suspension was stirred in the dark for 1.5 h to reach the dye adsorption – desorption equilibrium. A water filter was placed in between the light and the reaction vials to block IR irradiation. 2 ml mixture was taken out from the reaction vial at a desired time interval and centrifuged at 12, 000 rpm to remove $CuBi_2O_4$ particles. Then the optical absorption peak at

λ = 664 nm from the residue MB solution was recorded by a spectrometer (Ocean Optics, USB 2000) and used for photodegradation rate determination.

For photocurrent characterization, pre-cleaned indium tin oxide (ITO) coated glass slide (Rs = 8 - 12 Ω; Delta Tech. Ltd.) were used as substrates for film coatings. The spray coated substrates of desired dimension (1 cm × 1 cm) were used as the electrode (also called as a photocathode, in our case). **Figure 4.2** shows the primary three steps used to prepare a photocathode sample. The ITO substrates were cut into the sizes of 1.0 mm × 1.7 cm, and they were cleaned using a 5:1:1 mixture of deionized (DI) water, H_2O_2, and aqueous ammonia (NH_4OH) solution. Specifically, the substrates were boiled in the mixture solutions for 15 minutes before being dried with nitrogen flow. Step (1): The synthesized $CuBi_2O_4$ microflowers suspension of known concentration (5.0 mg/ml) was prepared by mixing it in DI water. Then the suspension was sonicated for an hour in a beaker before loading it into the spray gun (A4305 Airbrush; The Testor Corporation, Rockford, IL). Step (II): The ITO substrates to be coated were pre-heated for about 30 mins on a hot plate by controlling the temperature (= 200 ± 10 °C). Then we sprayed the suspension within the desired area by blocking the unwanted prat by a clean glass slides at an optimized nozzle to substrate distance (= 8 cm) and at about a constant flow rate (= 2 mL/minute). After spraying 20 mL, we left the substrates on the same stage for another hour as a post-coating treatment. Finally turned off the hot plate and took out the samples when cool down to a room temperature. Note that the mass deposited onto the 1 cm × 1 cm ITO substrates were estimated to be 25 ± 6 mg. The film morphologies of the photocathode are shown in Fig. S6. Cyclic voltammetry (CV), linear sweep voltammetry (LSV), and chronoamperometry measurements (I-t curves) were performed in a home-made single compartment photoelectrochemical (PEC) cell. The PEC cell consisted of a quartz window (%T >90% in the visible wavelength range) and

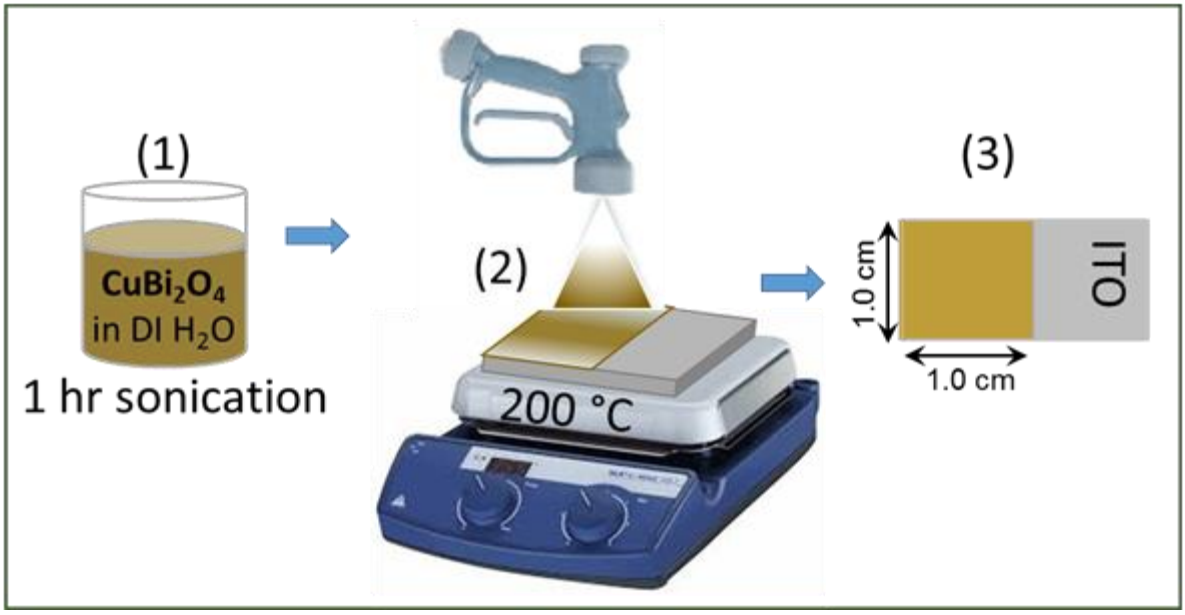

Figure 4.2. Step by step illustration of the film coating of micropowder by using a spray method on a hot plate.

conventional 3-electrode arrangement connected to a Potentiostat (CH Instruments Inc., CHI1040C). The reference and counter electrodes were 3 M Ag/AgCl electrode and platinum wire, and the ITO coated sample served as the working electrode. The electrolyte was prepared by dissolving boric acid (3.2 g, 0.5 M) in DI water (100 mL) and the pH was adjusted to 7 by using potassium hydroxide. The prepared solution was then purged for 30 minutes with N_2 gas to remove the oxygen before use in PEC measurements.

Light-Activated Antimicrobial Functions. The antimicrobial performance of the samples was characterized by using *E. coli* TOP10 strains. The frozen bacteria (kept at -80^{o}C) were activated in 50 ml fresh TSB media overnight (18 hrs) at 37^{o}C with shaking (250 rpm). Then the bacteria were washed twice with phosphate buffered saline (PSB, 1×) to remove TSB media and collected by centrifuging at 4000 rpm for 5 min. The collected bacteria were then re-suspended into PBS and diluted to ~ 2×10^3 CFU/ml.

For the white light induced antimicrobial test, 50 µl (2×10^3 CFU/ml) bacteria suspension was mixed with 50 µl $CuBi_2O_4$ suspension, the final concentration of $CuBi_2O_4$ in the mixture was 2.5 mg/ml. Then the 100 µl mixtures were plated onto a trypticase soy agar (TSA) plate uniformely and exposed to a 14 W Osram Sylvania LED A19 light at an intensity of ~10 mW/cm^2 in a bio-safety carbinet. After every 3 hours light exposure, plates were put into an incubator and incubated at 37 ^oC for 22 ~ 24 hrs. The grown colonies were counted after incubation. Light control was performed using 50 µl bacteria suspension mixed with 50 µl PBS under light illumination, while dark control was using 50 µl bacteria suspension mixed with 50 µl $CuBi_2O_4$ suspension without any illumination. Negative control was performed with 50 µl bacteria suspension mixed with 50 µl PBS in the dark. All three sets of controls were also incubated at 37 ^oC for 22 ~ 24 hrs before counting colony numbers.

4.3 Morphologies and crystal structures

The typical scanning electron microscope (SEM) images of five $CuBi_2O_4$ samples fabricated by different recipes are shown in **Figure 4.3**. It can be seen that the concentration of NaOH, C_{NaOH}, played a key role in the assembly of the hierarchical $CuBi_2O_4$ structures. With the decrease of the C_{NaOH} from 2.4 M to 0.98 M (**Figure 4.3**, Samples A, B, C, D), the morphology of $CuBi_2O_4$ changed from microspheres to nanorods and then micro-flowers. When the C_{NaOH} = 2.4 M, Sample A formed hierarchical $CuBi_2O_4$ microspheres composed of nanorods (**Figure 4.3A**). Those microspheres had a mean diameter of 2.6 ± 0.2 µm. From the zoomed-in SEM image of **Figure 4.3A**, it shows that the microspheres consisted of highly closed-packed nanorods. When the C_{NaOH} was reduced to 1.38 M (Sample B), nanorods with a mean length of 150 ± 30 nm and a mean diameter of 38 ± 9 nm were observed in the products. After removing large particles by

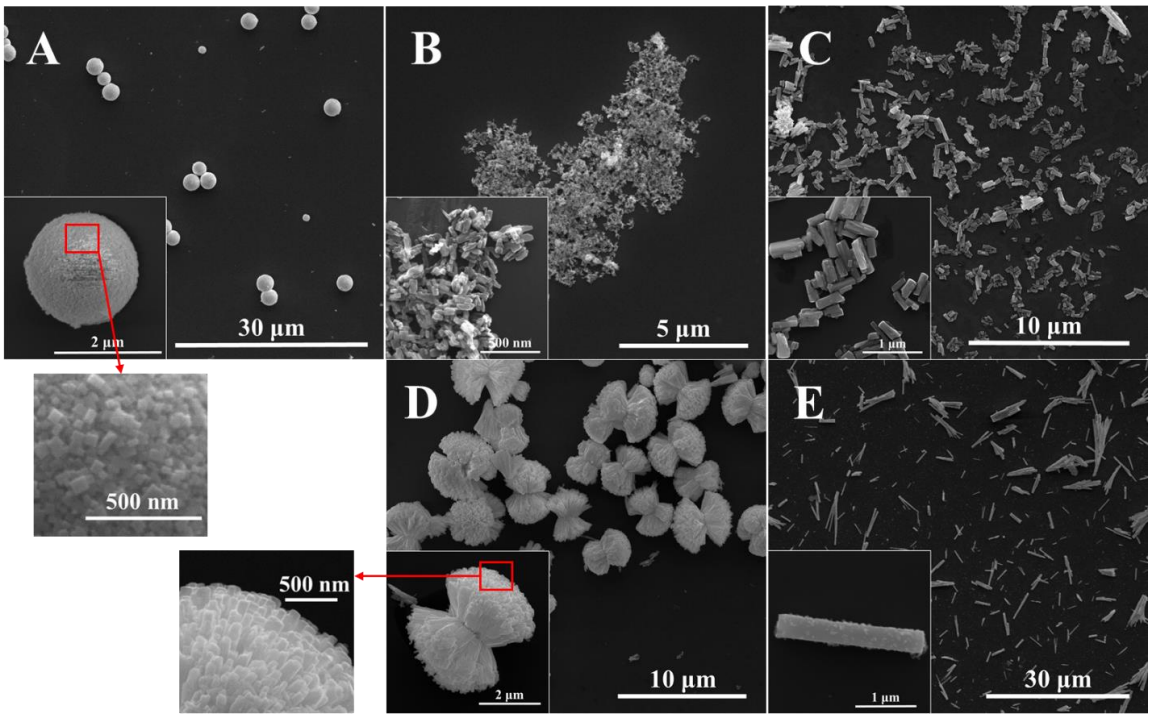

Figure 4.3. Representative SEM images of $CuBi_2O_4$ particles synthesized using 5 different recipes. A: microspheres with nanosquares; B: nanorods; C: nanorods; D: micro-flower with nanoblades; E: microrods.

sedimentation and filtration, a clear brown colored solution was collected. The nanorods remained as a stable colloid in ethanol, while the sedimentation was $CuBi_2O_4$ hierarchical microspheres (**Appendix A, Figure S1**). When the C_{NaOH} was further reduced to 1.18M, the resulting Sample C also had two morphologies: more uniform nanorods (600 ± 200 nm in length and 96 ± 30 nm in diameter) in suspension with clear facets, as shown in **Figure 4.3C**, and the hierarchical microsphere sedimentation (**Appendix A, Figure S1B**). However, the surface morphologies of the hierarchical microspheres from Samples B and C were different: the packing of nanorods in Sample B was closer than those in Sample C. When C_{NaOH} was decreased to 0.98M, nanoblade structures appeared and they assembled into highly dispersed hierarchical micro-flower structures with mean size of 4 ± 1 um from tip to tip (**Figure 4.3D**, measurements are shown as the blue line). Again, the packing of the nanoblades was looser when compared with other samples synthesized

from aqueous solutions. In the case of water-ethanol bi-solvent system, microrod structures (3 ± 2 μm in length and 0.3 ± 0.1 μm in diameter, **Figure 4.3E**) were obtained. The above results demonstrate that both the NaOH concentration and the solvent system contribute to the morphologies of $CuBi_2O_4$ from hydrothermal synthesis. In this reaction system, NaOH promotes the formation of CuO and Bi_2O_3. With higher concentration of NaOH, $Cu(OH)_2$ and $Bi(OH)_3$ formed at the early stage when NaOH was added into the mixture of Cu^{2+} and Bi^{3+}, and then grew into $CuBi_2O_4$. With a low C_{NaOH} in the reaction system, the assembling of $CuBi_2O_4$ hierarchical structure was loose and could be easily broken into its smaller building blocks by sonication. However, further reduction in the C_{NaOH} caused the reaction of CuO and Bi_2O_3 to form blade-like structures and the assembly of those substructures did not form a complete sphere, rather micro-flower structures occurred. By introducing ethanol into the solvent system, the solubility of Bi^{3+} decreases. In a water-ethanol bi-solvent system, the hydrothermal synthesis includes alcoholysis and hydrolysis processes. The formation and dissociation of $[Bi_6O_5(OH)_3](NO_3)_5 \cdot 3H_2O$ complex

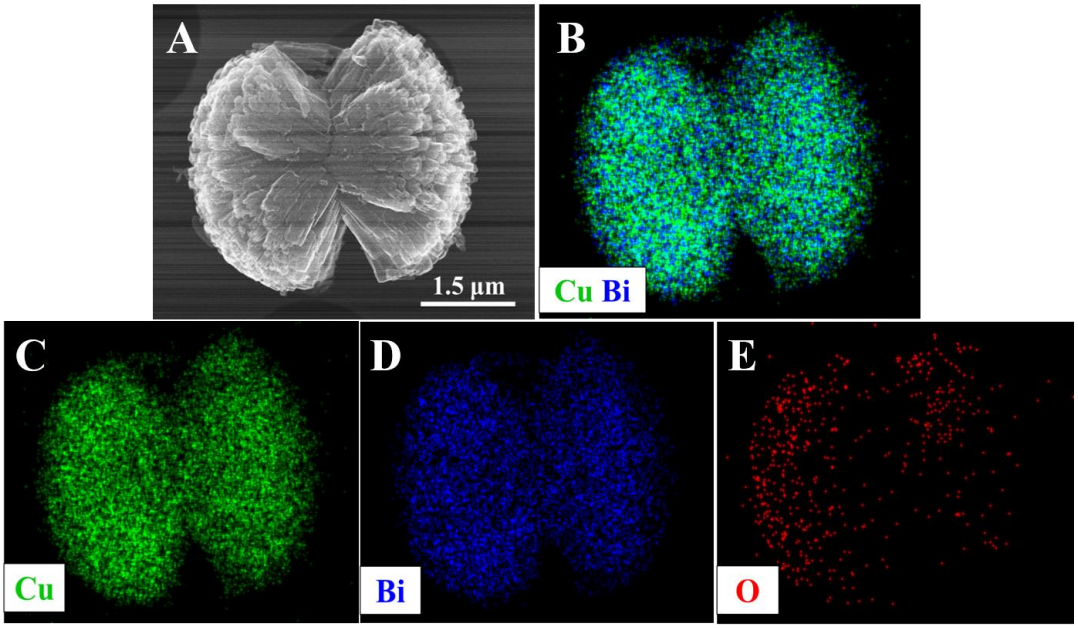

Figure 4.4. A: STEM image, B - E: elemental distribution maps for Cu, Bi and O of the as-prepared $CuBi_2O_4$ micro-flower structure.

controls the free Bi^{3+} concentration. [144] With van der Waals interactions, 1-D crystal microrods formed by the oriented aggregation of $CuBi_2O_4$ nanoparticles through lattice fusion, rather than forming 3D microspheres. [145]

The $CuBi_2O_4$ micro-flower structure was further investigated by energy dispersive spectroscopy (EDS) and high-resolution transmission electron microscopy (HRTEM) to explore its composition distribution and detailed crystal structure. As shown in **Figure 4.4A**, the nanoblades with a mean diameter of 100 ± 20 nm were arraged concentrically. The EDS result (**Figure 4.4B-E**) shows that the microstructure was composed of Cu, Bi and O elements. Both Cu and Bi were uniformly distributed in the structure (**Figure 4.4B-D**). However, as shown in **Figure 4.4E**, the O signal was low and not evenly distributed, which was caused by self-absorption during the EDX measurement due to sample ruggedness (not flat enough). EDS mapping (**Appendix F, Table S1**) showed that the molar ratio between Bi and Cu elements was 1.68 : 1, which is lower than 2 : 1, but such a measurement has a large error bar (see Support Information S7). The HRTEM image shown in **Figure 4.5** demonstrates that the substructure of the $CuBi_2O_4$ micro-flowers was single-crystalline, and there was also a thin amorphous shell with a thickness of ~ 1.1 nm. The 0.315 nm d-spacing between two adjacent lattice planes coresponds to (211) planes of tetragonal $CuBi_2O_4$.

Figure 4.6 shows the X-ray diffraction (XRD) patterns of all five samples. All of the peaks can be indexed to the tetragonal $CuBi_2O_4$ structure (JPCDS No. 01-080-1907) with the space group *P4/ncc* except Sample B. In the XRD patterns of Samples A, C, D and E, no peak from impurities was detected, which indicates the high purity of these $CuBi_2O_4$ samples. For Sample B, two impurity peaks from copper oxides (JPCDS No. 01-080-1916) were observed. The formation of $CuBi_2O_4$ during hydrothermal synthesis involves several steps. First, the Cu^{2+} and Bi^{3+} sources

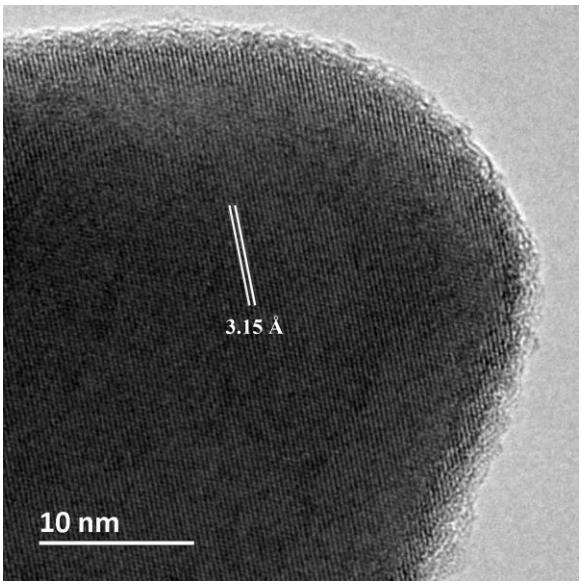

Figure 4.5. A representative HRTEM image of the $CuBi_2O_4$ micro-flower sub-structure.

react with OH^- to form $Cu(OH)_2$ and $Bi(OH)_3$. Then CuO and Bi_2O_3 are formed during the hydrolysis reactions. Finally, the lattice fusion of CuO and Bi_2O_3 under high temperature during the hydrothermal process resulted in the formation of $CuBi_2O_4$ micro/nanostructures. [146] After the formation of substructures, the adjacent nanostructures could share a common crystallographic orientation, and oriented aggregation causes the growth of $CuBi_2O_4$ 3D hierarchical structures. The impurity peaks of Sample B indicate that the reaction during the hydrothermal process was not completed. For these five samples, the XRD peak intensities of each pattern varied. As shown in **Figure 4.6**, the XRD peaks of Sample D were much sharper than those of the others, which indicated that it was highly crystallized. According to Scherrer's equation, the crystal sizes of $CuBi_2O_4$ can be estimated as 46.2 nm, 46.2 nm, 46.2 nm, 32.0 nm, and 41.6 nm for Samples A-E, respectively. For the (211) crystal plane, relative peak intensity ratio of (200) face and (211) face were compared to further understand the crystallization quality of different samples. For all the $CuBi_2O_4$ samples, the ratio of XRD intensities between (200) and (211) are, A: 18.7 %; B: 16.8 %; C: 18.6 %; D: 20.2 % and E: 41.1 %. Comparing these ratios to the same ratio from the XRD

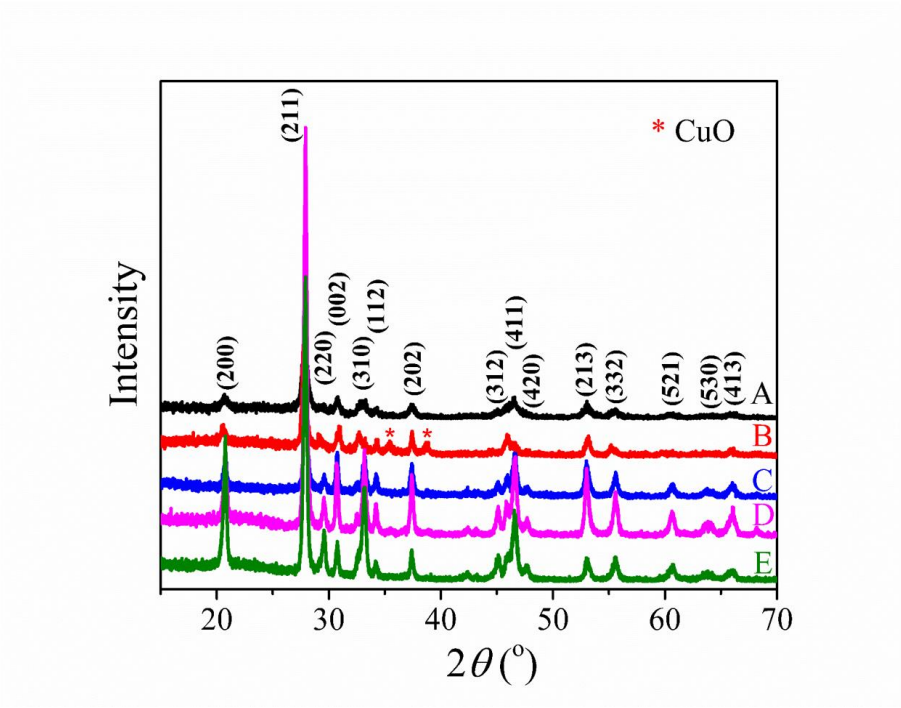

Figure 4.6. XRD patterns of different $CuBi_2O_4$ samples.

reference (JPCDS No. 01-080-1907), which is 18.6%, the quality of crystallization of Sample D is good.

4.4 Optical properties and photocatalytic activites

4.4.1 Optical properties

UV-Vis transmission spectra in the wavelength range of λ ~350 nm to 1100 nm of all five samples are shown in **Figure 4.7**. To ensure a fair comparison, UV-Vis spectra of a series of suspensions with different concentrations of each sample were measured, a constant concentration (*i.e.* ~ 0.19 mg/ml) which lied in the linear region of Beer's law for all the samples (**Appendix B, Figure S2**) was used to obtain spectra in **Figure 4.7**. As shown in **Figure 4.7**, different samples show very different transmission spectra. Sample A has the highest light transmission across the entire wavelength range measured. The transmission slightly increases when the wavelength

increases. Samples E and D have similar optical behaviors. But Samples B and C show very different spectra. Though the absolute transmission coefficients are different, the spectra of Samples B and C show low transmission at $\lambda < 700$ nm and high transmission at $\lambda > 700$ nm. From **Figure 4.3**, Samples A, D, and E are microstructures with characterization length around 2-10 μm, while Samples B and C are nanostructures. For microstructures with dimension close to the wavelength of the probe light, like Samples A, D, and E, their transmission spectra are dominated by Mie scattering: The larger the particle size, the bigger the forward scattering cross-section. Comparing the particle size in Samples A, D, and E, Sample A has a larger size, while Sample D has a porous structure. Thus, Sample A has the largest transmission. However, for Samples B and C, since the structure is on the nanometer scale, the transmission spectra are dominated by the intrinsic property of the material. For example, $CuBi_2O_4$ has a bandgap of ~1.5 eV, which corresponds to a cut-off wavelength of $\lambda = 827$ nm in absorbance. Experimentally one observes that there is a transmission valley when $\lambda < 700$ nm (corresponding to an apparent bandgap of 1.58 eV), which is consistent with the known bandgap value of $CuBi_2O_4$.

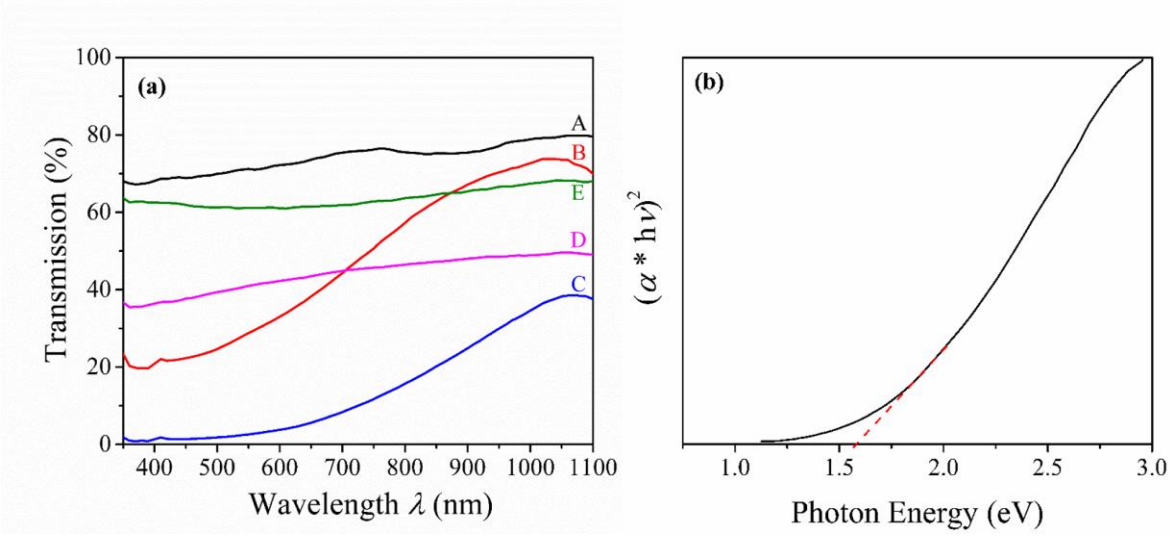

Figure 4.7. (a) UV-Vis transmission spectra of 5 different $CuBi_2O_4$ samples in suspension, and (b) the Tauc plot of Sample C (assuming direct transition).

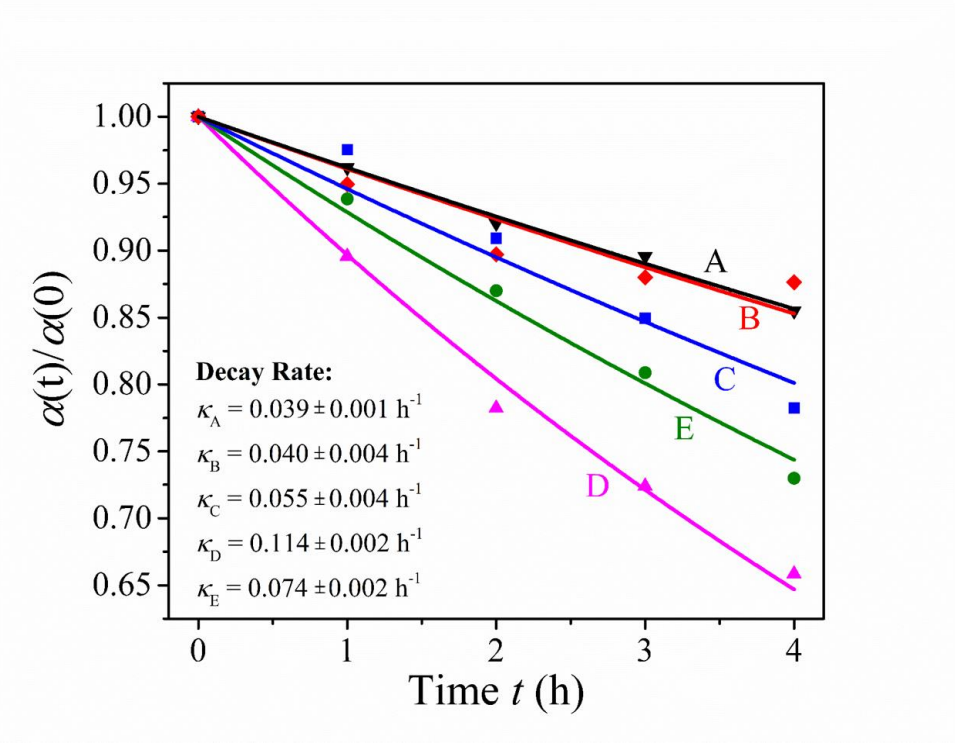

Figure 4.8. The plot of the normalized MB absorbance $\alpha(t)/\alpha(0)$ versus photodecay time t for different $CuBi_2O_4$ samples. The solid curves are fitting results using **Equation 3.1**, and the resulting decay rate κ is summarized in the figure.

4.4.2 Photocatalytic dye degradation activities

Figure 4.8 shows the normalized methylene blue (MB) absorbance $\alpha(t)/\alpha(0)$ at λ = 664 nm, where $\alpha(t)$ and $\alpha(0)$ are the absorbance at time t and t = 0 for different samples during the photodegradation process. When the light illumination is prolonged, the absorbance peak of MB decreases which indicates the decomposition of MB molecules. The absorbance data can be fit into a first-order exponential decay equation (**Equation 3.1**), and the results are summarized in **Figure 4.8**. Sample D shows the highest decay rate with $\kappa_D = 0.114 \pm 0.002$ h^{-1}. The decay rate of Sample A ($\kappa_A = 0.039 \pm 0.001$ h^{-1}) and Sample B ($\kappa_B = 0.040 \pm 0.004$ h^{-1}) are very close, but lower than those of the other samples. The mechanism for the $CuBi_2O_4$ based MB degradation involves three major steps [147]: $CuBi_2O_4$ absorbs photons with the appropriate energy to generate electron-hole

pairs when illuminated by visible light; the photo-generated electrons and holes separate and migrate to the surface of $CuBi_2O_4$; and the photo-induced carriers cause reduction and oxidization of MB in the aqueous solution. During those processes, the total surface area of the $CuBi_2O_4$ samples plays a key role. Using the SEM images shown in **Figure 4.2**, the total surface area A of each sample can be estimated as,

$$A = \frac{M_{total}}{M_{particle}} \times A_{particle} \tag{4.2}$$

where M_{total} is the total mass of $CuBi_2O_4$ sample used for MB photodegradation experiment, M_{total} = 15 mg, $M_{particle}$ is the average mass of a representative micro/nano-particle,

$$M_{particle} = V_{particle} \times \rho \tag{4.3}$$

where ρ is the density of $CuBi_2O_4$, $V_{particle}$ and $A_{particle}$ are the average volume and area of the representative particle. The particles in Sample A can be treated as spheres with a mean diameter of 2.6 μm. Thus, when the sample mass is 15 mg, A_A = 41 cm^2. The particles in Samples B, C and E can be treated as cylindrical rods, and the respective surface areas of 15 mg can be estimated as A_B = 2093 cm^2, A_C = 794 cm^2, A_E = 247 cm^2. For sample D, the surface area is hard to estimate because of its flower-like shape. However, according to SEM measurements, Sample D is made up of nano-blades, which have a similar length (1.4 ± 0.3 μm), which is shorter than the length of the individual particles of Sample E. Thus, Sample D is assumed to have a larger surface area than Sample E. In addition, a smaller total surface area also increases the chance of recombination of the photogenerated electrons and holes, which is another factor affecting photocatalytic activity. The crystallinity of the material is another important factor for the photocatalytic property. According to the XRD results discussed above (**Figure 4.6**), Samples A, C, and D have similar crystal quality while Samples B and E have a very different XRD intensity ratio of (200) and (211).

In additional, Sample D has the smallest crystal size which could significantly contribute to the high photodecay rate.

4.4.3 Photoelectrochemical (PEC) properties

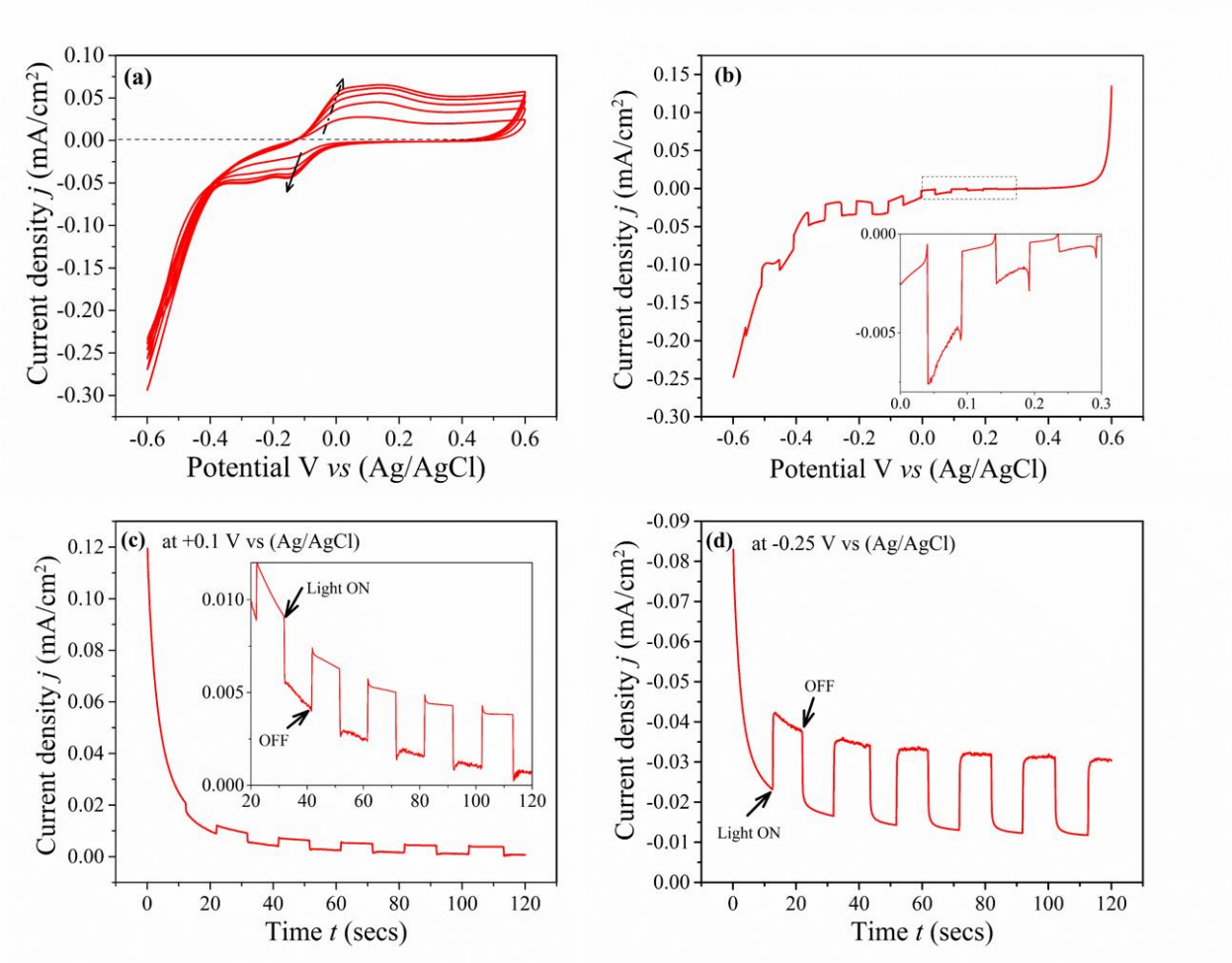

Figure 4.9. PEC properties of sample D: (a) Cyclic voltammetry and (b) linear sweep voltammetry in the voltage range of +0.6 to -0.6 V vs Ag/AgCl with a scan rate of 20 mV/s. Fig. (b) insert shows the onset potential (+0.3 V vs (Ag/AgCl)). (c) Photocurrent response at positive bias voltage and (d) negative bias voltage, details are shown inside the respective figures.

The cyclic voltammetry (CV), linear sweep voltammetry (LSV), and chronoamperometry measurements (*I*-t curves) for sprayed Sample D are shown in **Figure 4.9** (a) to **Figure 4.9** (d). **Figure 4.9** (a) shows five CV cycles recorded at a fixed scan speed (= 20 mV/s) in a potential window ranging from +0.6 to -0.6 V (*vs* Ag/AgCl). All CV curves exhibit distinctive anodic and cathodic peaks at +0.079 and at -0.12 V, respectively. After each CV cycle, the current density at the cathodic and anodic peaks were decreasing and the voltage shifted slowly towards more negative and positive values, respectively. The decreased current density can be attributed to the loss of photocatalysts from the electrode, which could be due to weak binding of the materials onto the substrate. The separation between anodic and cathodic peaks reveals an irreversible process which could be due to the transformation of Bi^{3+} to Bi^{5+} by photogenerated electrons as reported in the literature.[36] This result is consistent with the high antimicrobial activity observed based on the fact that the $CuBi_2O_4$ prepared by this method may generate more radicals to react with the bacteria and MB molecules upon white light illumination **Figure 4.9** (b) shows a LSV curve in the same potential window obtained by chopping the illumination of the solar simulator (of intensity 100 mW/cm^2) manually at a frequency of 0.1 Hz. The onset potential was observed at +0.3 V *vs* (Ag/AgCl) as shown in the inset of **Figure 4.9** (b). The good photoresponse at these lower potentials can be attributed to both the lower bandgap and the favorable CB and VB of $CuBi_2O_4$ as illustrated in Figure 1. The observed photo-induced cathodic currents demonstrate the p-type semiconductor nature of the $CuBi_2O_4$ sample.[148] Lastly, the sample was scanned for I-t curves at low positive and negative bias potentials, and the results are shown in **Figure 4.9** (c) and **Figure 4.9** (d), respectively. The cathodic current at negative bias (-0.25 V) is about 6 times higher (= 0.02 mA/cm^2) than the current at positive bias potential (= 0.003 mA/cm^2), which is as expected. Because of the different experimental parameters and electrochemical systems, it is hard to

compare the results with other reports, however, it is worth noting that the observed cathodic photocurrent at negative bias (-0.25 V) is higher than the reported results for both n- and p-type $CuBi_2O_4$ micro-/nano-structures. For instance, Wang *et. al.* and Sharma *et. al.* recently reported the photocurrent density to be about 6 $\mu A/cm^2$ and 6.45 $\mu A/cm^2$ with n-type hedgehog-like hierarchical microsphere and with p-type nanocrystals, respectively.[149-150] Our result is about 3 times higher than those reported results. It is important to note that Wang *et al*. have used 0.5 M Na_2SO_4 electrolyte, 300 W xenon lamp, and a 0.6 V bias (*vs* SCE; saturated calomel electrolyte), [151] while Sharma *et al.* have used 0.1 M K_2SO_4 / 0.01 M $Na_2S_2O_8$ and 300 W xenon arc lamp and 0.75 V (*vs* NHE; normal hydrogen electrode). [152] It is interesting that the cathodic photocurrents at both positive and negative bias potentials get stabilized in the interval of about 2 minutes. The stability of the photocathode was tested by using UV-Vis (% Transmittance) and XRD measurements before and after the PEC characterizations (**Appendix C and D, Figure S3 (a)-(b) and S4**). No significant changes in the crystal structures and optical absorbance edge (except the slight change in % Transmittance) are observed down to the detection limit of instruments, indicating $CuBi_2O_4$ samples are stable. In contrast, the loss of photocurrent density could be due to the material fall off during the PEC experiments, which further validates the observed results in CV cycles. Specifically, we observed about 27% and 34% loss in absorbance at the wavelengths of λ = 500 nm and λ = 800 nm respectively (**Appendix C, Figure S3**), which is consistent with the observed loss in photocurrent density within 7% error.

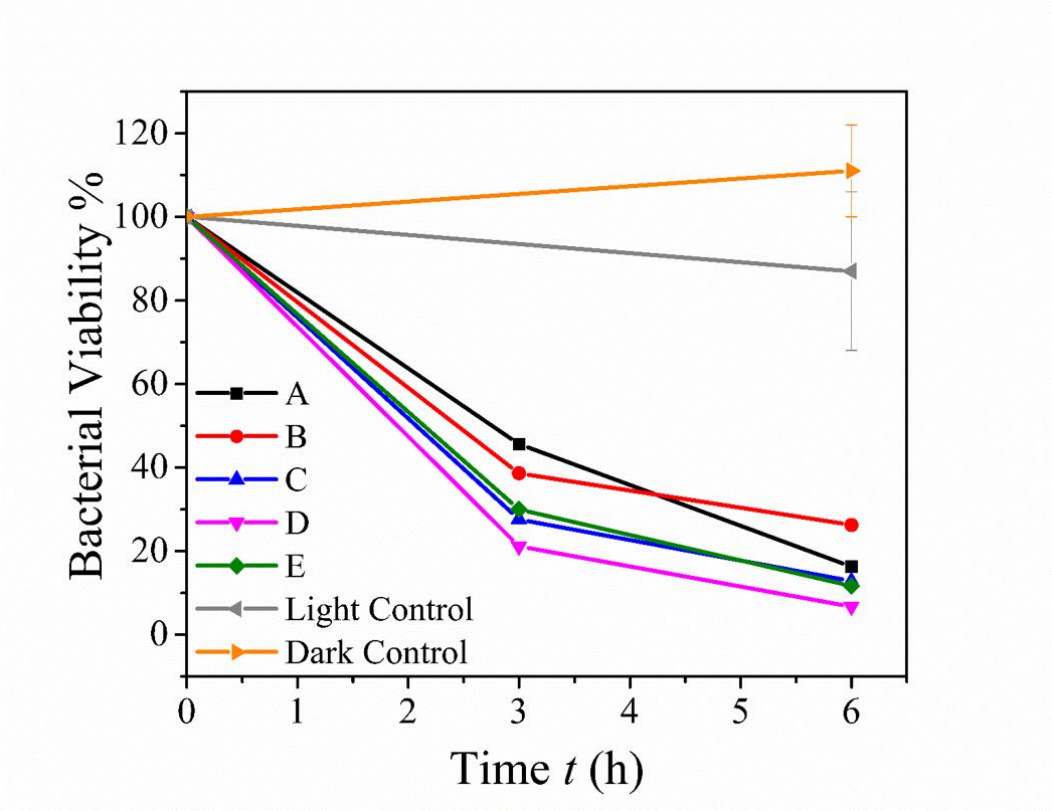

Figure 4.10. The plot of E. coli viability percentage ε measured by TSA plating method versus LED illumination time t for different $CuBi_2O_4$ samples with a fixed $CuBi_2O_4$ concentration of 5 mg/ml.

4.5 Antimicrobial activities

The results of visible light induced antimicrobial activities of $CuBi_2O_4$ samples against *E. coli* on TSA plates are shown in **Figure 4.10**. For all the samples, the bacteria survival ratio decreases dramatically with the addition of $CuBi_2O_4$ after 6 hr. The dark control shows that as synthesized $CuBi_2O_4$ samples have no negative effects for bacteria growth. The light control demonstrates that bacteria were slightly decreased compared to that of dark control after 6 hr LED light exposure. For plates with $CuBi_2O_4$ samples, after light illumination for 3 hr, the bacterial viability ratio $\varepsilon \left(= \frac{\text{\# of alive bacteria after illumination}}{\text{\# of initial alived bacteria}} \right)$ is, ε_A = 45.6%, ε_B = 38.8%, ε_C = 27.7%, ε_D = 21.1%, and ε_E = 30.0%, respectively. For longer duration illumination (6 hrs), ε deceases

further, ε_A = 16.3%, ε_B = 26.3%, ε_C = 12.8%, ε_D = 6.7%, and ε_E = 11.7%, respectively. Roughly, one has $\varepsilon_B < \varepsilon_A < \varepsilon_C < \varepsilon_E < \varepsilon_D$, which is similar to the trend of the dye degradation rate κ. Sample D, the micro-flower $CuBi_2O_4$, again shows the highest antimicrobial activity (93.3% bacteria inactivation) among all five samples.

According to previous reports, the photo-induced antibacterial properties of photocatalysts are caused by reactive oxygen species (ROS), such as ·OH, O_2^-, and H_2O^+. [34, 62, 153] Under visible light irradiation, photogenerated electrons on the surfaces of $CuBi_2O_4$ can be transferred and captured by surface absorbed O_2 molecules then reduced to O_2^- as shown in Fig. 1. The ROS and h^+ can attack the cell wall and cell membrane, which contributes to the changes of cell morphologies and leads to damage of cell integrity. The physical state of the cell membrane strongly affects the viability of bacteria; because of the decomposition of the cell wall and cell membrane, this will cause the leaking of the cell‘s interior components.[62, 154] Without the protection of the cell wall and cell membrane, more severe damages, such as disruption of DNA molecules and decomposition of interior components, would occur.[62, 136-137] Thus, the bacterial cells can be irreversibly de-energized. The hierarchical micro-flower show about 93 % bacteria inactivation with 6-hr visible light irradiation. However, compared with the photocatalytic dye degradation results, the difference among the results of the antimicrobial tests is not significant. This might be attributed to the morphology and size of $CuBi_2O_4$ samples and *E. coli* cells. *E. coli* is rod-shape bacterium with an approximate size of 2 μm in length and 0.5 μm in width, which are comparable or even larger than the size of particles of the $CuBi_2O_4$ samples. According to the antibacterial mechanism, the redox radicals can only atack the cells when the cells touch the $CuBi_2O_4$ particles, i.e., the contact surface area between the cells and $CuBi_2O_4$ particles play the decisive role, while the extended surface areas inside the $CuBi_2O_4$ particles do

not contribute significantly. But for the MB molecules, since the physical size is about 1 nm, they can reach inside small pores of the $CuBi_2O_4$ particles, *i.e.*, the extended surface area plays a key role in dye photodegradation.

4.6 Conclusions

In summary, five $CuBi_2O_4$ samples with different morphologies and structures were successfully synthesized via a facile hydrothermal process. The roles of initial concentration of NaOH and the solvent system were found to be important factors during the growth of the $CuBi_2O_4$ samples. By varying the amount of NaOH, $CuBi_2O_4$ hierarchical micro-structures with different sub-nanostructure could be obtained. The introduction of EtOH as a bi-solvent also changed the oriented growth of $CuBi_2O_4$ to 1D microrods instead of a 3D hierarchical structure. The micro-flower structure with narrow bandgap showed the highest photocatalytic MB degradation and antimicrobial activity against *E. coli*. It also showed an excellent solar-conversion efficiency under a solar simulator and at neutral pH. The obtained $CuBi_2O_4$ material shows the potential application in the fields of water treatment, solar-energy conversion, and antimicrobial packing.

CHAPTER 5

HIGHLY EFFICIENT INORGANIC ANTIMICROBIAL $Cu_xFe_yO_z$ NANOSTRUCTURES

5.1 Introduction

As discussed in previous two chapters, inorganic semiconductors have been explored as antimicrobial materials. For typical materials that have been studied so far, the antimicrobial activities have been summarized in **Table 5.1**. [155-156] As shown in **Table 5.1**, most of these inorganic materials can lead to 3 – 8 log reduction of bacteria with time longer than 3 hrs. Only a few of them (Ag and Cu_2O) can effectively inactivate bacteria in a short period of time. For Ag nanoparticles, they are found to be one of the efficient antimicrobial agents and can react in a low Ag concnetration. [157] It was reported that 50 – 60 μg/mL Ag Nanoparticles can inhibit 10^5 CFU bacteria growing on media plates. [66] However, Ag are expensive and easy to be corroded. For Cu_2O, it might be toxic for the human cells. So that there is still an urgent need to develop biocompatible and high efficient antimicrobial inorganic material for different biomedical applications.

In this chapter, we report the synthesis of a mixture of nanostructured copper oxides (CuO and Cu_2O), iron oxide (Fe_2O_3) and copper iron oxide ($CuFeO_2$) through a microwave assisted hydrothermal method and their highly effective antimicrobial properties. Additionally, the nanostructure can also inhibit the growth of the bacteria in the fresh media. The cytotoxicity test of the $Cu_xFe_yO_z$ nanoparticles against mouse fibroblast cells suggesting that at a lower concentration ($\leq$ 1 mg/ml), the $Cu_xFe_yO_z$ nanoparticles are biocompatible to the mammalian cells.

Table 5.1. Inorganic antimicrobial materials.

Material	*Bacterial Strains*	*Reduction*	*Test Time*	*Reference*
Silver (Ag)	*E. coli/ S. aureus*	5-log	0.5/1.5 hrs	[158]
Coperic oxide (Cu_2O)	*E. coli*	7-log	5 min	[159]
Copper oxide (CuO)	*E. coli*	3-log	3 hrs	[74]
Nitric oxide (NO)	*E. coli/ A. baumannii/ S. aureus*	8-log	24 hrs	[160]
Zinc oxide (ZnO)	*E. coli*	6-log	48 hrs	[161]
Copper (Cu)	*E. coli/ S. aureus*	4-log	24 hrs	[42]

5.2 Experimental methods

$Cu_xFe_yO_z$. In a typical synthesis process, 0.242 g $Cu(NO_3)_2 \cdot 3H_2O$ (ACROS Organics) and 0.404 g $Fe(NO_3)_3 \cdot 9H_2O$ (Alfa Aesar) were thoroughly dissolved into 10 ml deionized (DI) water. 10 ml 1 M NaOH solution was firstly added into the mixture dropwise with constant stirring. Then 200 μl to 500 μl 37% formaldehyde (J.T. Baker) was added into the mixture. 4 ml of the resultant solution was transferred into a 10 ml SiC reaction tube and kept in the microwave chamber at 200 ℃ for 2 hr. After cooling down, as synthesized sample was then collected by centrifugation at 12,000 rpm and washed by DI water for 5 times. The collected sample was then oven dried at 60 ℃ overnight. The as-prepared $Cu_xFe_yO_z$ samples are labeled corresponding to the added CH_2O amount during synthesis. For instance, S200 corresponds to the sample synthesized with 200 μl CH_2O, S500 corresponds to the sample synthesized with 500 μl CH_2O.

Dye degradation. The dye degradation experiments were performed with methyl orange (MO) and MB aqueous solutions with a concentration of 30 μM at room temperature. All experiments were performed with $Cu_xFe_yO_z$ nanoparticles concentration as 0.5 mg/ml, and a fixed

volume V = 20 ml of dye solutions. The reaction systems were kept under dark conditions with constant stirring. At the specific time interval (2, 4, 6, 8, 10 and 24 hrs), an aliquot sample was taken out and centrifuged at 12,000 rpm to remove the nanoparticles and the concentration change of MO and MB in the remaining solution were investigated by UV-Vis spectroscopy (JASCO V-570).

Antimicrobial tests. The antimicrobial performance of the samples was characterized by using multiple bacterial strains (*E. coli* B, *E. Coli* O157:H7, *S. aureus*, *K. Pneumoniae* 148, *K. Pneumoniae* ATCC-BAA-2472, *Listeria monocytogenes*, *Salmonella* MDR-ATCC-700408, *H. pylori*, and *S. flexneri*)s. The bacterial stocks were activated in fresh liquid media (trypticase soy broth (TSB) for *E. coli* B and *S. aureus*; lysogeny broth (LB) for *E. Coli* O157:H7, *K. Pneumoniae* 148, *K. Pneumoniae* ATCC-BAA-2472, *Listeria monocytogenes*, *Salmonella* MDR-ATCC-700408, and *S. flexneri*) overnight at 37 ^{o}C with shaking (250 rpm). *H. pylori* cells were grown and harvested on blood agar (BA) plates.

For the antimicrobial tests with bacterial cells in 1X PBS, the grown bacteria cells were harvested by centrifugation at 4000 rpm for 5 min. Then the cells were washed twice with phosphate buffered saline (PSB, 1×) to remove media and re-suspended into the PBS. For *E. coli* B and *S. aureus*, 1 mg $Cu_xFe_yO_z$ nanoparticles were directly suspended into the bacteria suspension. For other bacterial strains, the cells were firstly standardized to OD600 = 2 in PBS (~ 10^9 to 2×10^9), then 0.25 ml of each cell suspension was diluted with either 0.25 ml of PBS as controls or 0.25 ml 2 mg/ml $Cu_xFe_yO_z$ nanoparticles. The mixtures of bacteria and $Cu_xFe_yO_z$ were incubated at 37 ^{o}C with shaking (200 rpm). At a specific time interval, such as 15 min, 30 min, 60 min, 120 min and 240 min, an aliquot suspension was taken out, then diluted 10-fold in PBS. The

dilutions were plated on media plates and incubated at 37 ºC overnight (except for *H. pylori*, which needs to be incubated on BA plate for a longer time) to count the colonies on the plates.

For the growth inhibition tests, bacterial cells were inoculate into fresh media premixed with $Cu_xFe_yO_z$ nanoparticles. Briefly, for *E. coli* B and *S. aureus,* 10 mg $Cu_xFe_yO_z$ nanoparticles were suspended in 0.1 ml PBS first, then added into 9.9 ml TSB (final nanoparticles concentration was 1 mg/ml). Then 10 µl bacteria suspension was inoculate into the media-NPs mixture and kept at 37 ºC overnight with shaking (250 rpm). For *K. Pneumoniae* ATCC-BAA-2472, *Salmonella* MDR-ATCC-700408, and *S. flexneri*, 2 µl bacteria suspension (~ 2×10^6 cells) was inoculated into 500 µl TSB with 1 mg/ml $Cu_xFe_yO_z$ nanoparticles. For *H. pylori*, 100 µl of the harvested cells in brain heart infusion-β-cyclodextrin (BHI-βc) (~ 10^7 cells) was inoculated into 2 ml BHI-βc with 0.1 ml 20 mg/ml $Cu_xFe_yO_z$ nanoparticles in PBS (final nanoparticles concentration was 1 mg/ml). These bacteria-media-NPs mixtures were then incubated at 37 ºC for 18 hrs with constant rocking. After co-incubating with nanoparticles in media, an aliquot amount of the mixture was taken out of each sample and diluted 10-fold in PBS. Then the dilutions were plated onto media plates, incubated at 37 ºC overnight (*H. pylori* was incubated on BA plates for a longer period) to count the colonies on the plates. Control groups were performed with equal volume of PBS to replace $Cu_xFe_yO_z$ nanoparticles suspension.

Cytotoxicity. Cytotoxicity of the $Cu_xFe_yO_z$ S500 are tested by the 24 hrs nanoparticles exposure at 37 ºC using mouse fibroblast cells. After 24 h of cell culture incubation in a 96-well plate, 10 µL of the $Cu_xFe_yO_z$ S500 (1 mg/ml or 10 mg/ml) in DMEM medium was added to the cells. The cells were allowed to respond to the nanoparticles during a separate 24 h incubation period inside a cell culture incubator at physiological temperature. The relative viability (%) of the cells in response to S500 was reported relative to the control (without S500 exposure).

5.3 Morphologies and crystal structures

With diffentent addtion amounts of CH_2O for the microwave assisted hydrothermal synthesis, 6 different $Cu_xFe_yO_z$ samples were formed. As shown in **Figure 5.1**, both the size and shape of final products varied. With the increasing of the addtion amount of CH_2O, the particle size is generally deceasing. The average size changes from 300 ± 100 nm, 320 ± 60 nm, 290 ± 60 nm, 280 ± 70 nm, 220 ± 40 nm to 100 ± 20 nm when the CH2O amount changes from 200 μl, 250 μl, 300 μl, 350 μl, 400 μl to 500 μl. As shown in the zoomed-in images in **Figure 5.1**, the samples comprise a various shapes of particles such as cubic, flake, and irregular shapes. The high resolution STEM image and the EDS elements mapping of S500 are shown in **Figure 5.2**. The EDS mapping results showed that the O atoms are uniformly distributed on the strucutre. Fe and Cu atoms are also distributed on the nanostructures but not evenly. However, there are more Fe atoms than Cu atoms on the cubics. And on the strip structure, there are mostly Cu atoms and few Fe atoms, which indicates that such amorphous strip structures are copper oxides Cu_xO.

The XRD patterns in **Figure 5.3(A)** reveal the crystalline structures of different $Cu_xFe_yO_z$ samples. Based on the crystal peak analysis, the samples are mixtures of Fe_2O_3, Cu_2O, CuO, and $CuFeO_2$, the results are consitant with the EDS mapping results shown in **Figure 5.2**. However, with the changing of the added amount of CH_2O during synthesis, the relative composition of final products changes. The addition of CH_2O is serving as a reducing agent to reduce Cu^{2+} to Cu^{+}, which means with more CH_2O adding in, more Cu_2O will be produced and less CuO will be present in the produce. For example, the S200 contains no Cu_2O, and S500 contains no CuO according to the XRD patterns. A semi-quantitative anylysis of the XRD data was performed by comparing the XRD intensy of a distiguish peak of each composite ((104) of Fe_2O_3, (111) of CuO and (200) of Cu_2O) to the (012) peak intensity of $CuFeO_2$ of each sample. As shown in **Figure 5.3(B)**, the

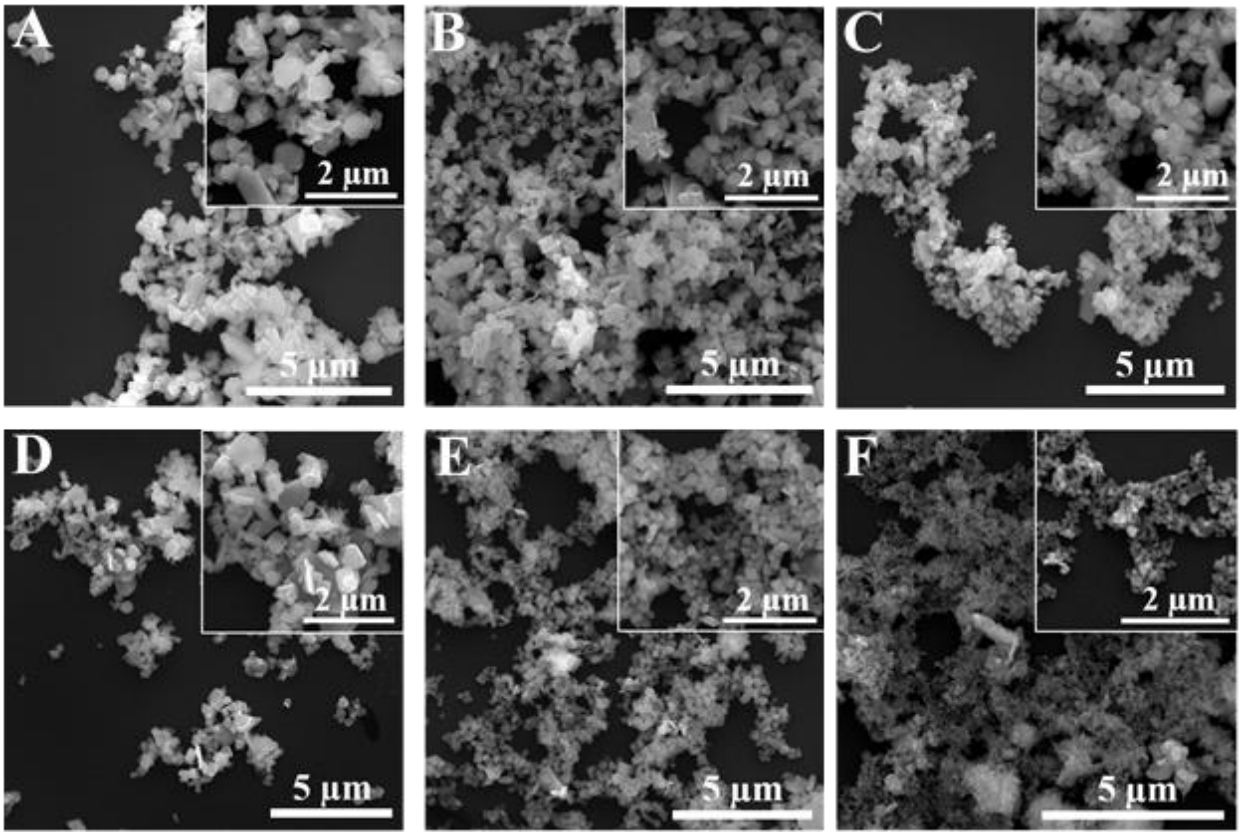

Figure 5.1. SEM Images of $Cu_xFe_yO_z$ nanostructures designated by CH_2O addition in synthesis. A: S200; B: S250; C: S300; D: S350; E: S400; and F: S500.

amount of CH_2O affects the compistion ratio of each sample dramatically. For instance, for S200 sample, the mixture contains 54% $CuFeO_2$, 26% CuO, 0% Cu_2O and 20% Fe_2O_3. For S250, the mixture has 39% $CuFeO_2$, 11% CuO, 17% Cu_2O and 33% Fe_2O_3. S300 has 42% $CuFeO_2$, 22% CuO, 8% Cu_2O and 28% Fe_2O_3. S350 has 30% $CuFeO_2$, 19% CuO, 35% Cu_2O and 16% Fe_2O_3. S400 has 51% $CuFeO_2$, 10% CuO, 10% Cu_2O and 29% Fe_2O_3. And S500 has 36% $CuFeO_2$, 0% CuO, 28% Cu_2O and 36% Fe_2O_3. The overall general trend is that with the increase of CH_2O, the CuO decreases and Cu_2O increases.

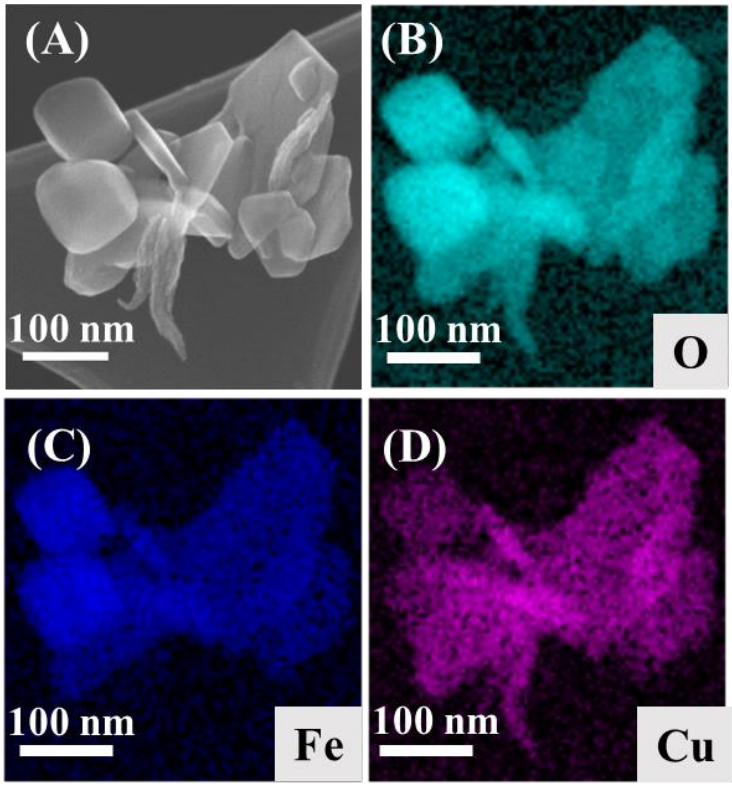

Figure 5.2. STEM image and EDS mapping (elements of O, Fe, and Cu) of the $Cu_xFe_yO_z$ S500 with three different morphologies. (A) The STEM image. (B) – (D) EDS mapping of O, Fe, and Cu.

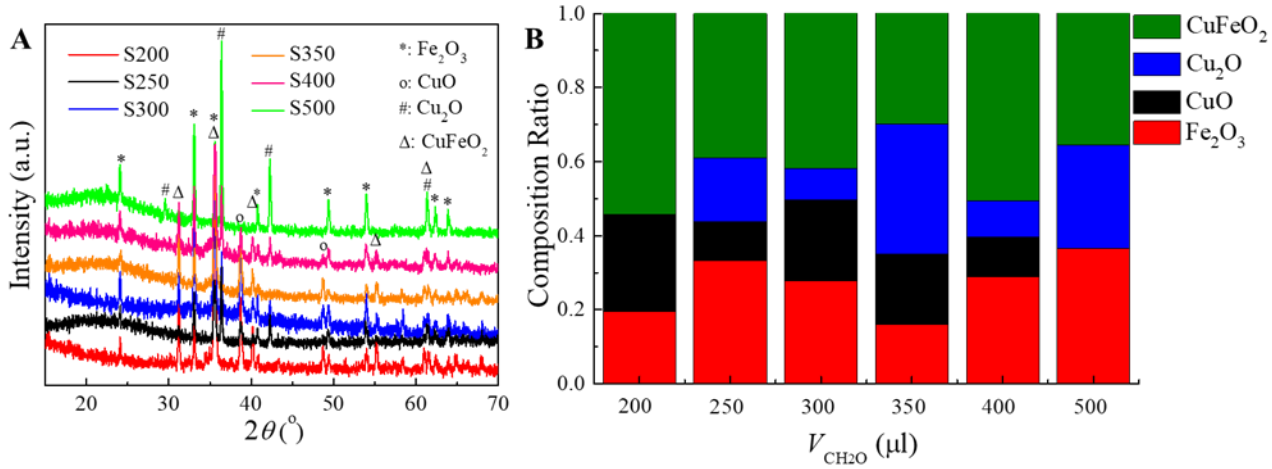

Figure 5.3. (A) XRD patterns of different $Cu_xFe_yO_z$ samples. (B) Relative compositions (CuO, Cu_2O, and Fe_2O_3) with respect to $CuFeO_2$ of different $Cu_xFe_yO_z$ sample.

5.4 Optical properties and dye degradation activities

The oprical properties of the $Cu_xFe_yO_z$ samples were characterized by the diffuse reflectance spectroscopy. **Figure 5.4(A)** shows the modified UV-vis diffuse reflectance spectra of the $Cu_xFe_yO_z$ samples based on the Kubelka-Munk function,

$$F(R) = \frac{(1-R)^2}{2R} \quad , \tag{5.1}$$

where R is the reflectance, and $F(R)$ is proportional to the extinction coefficient. It shows that all of the $Cu_xFe_yO_z$ samples exhibit strong absorption in the range of visible light (wavelength 400 nm to 700 nm). The effective indirect band gaps of these samples were determined by Tauc's plots of $F(R)$. The indirect bandgaps of the $Cu_xFe_yO_z$ samples are summarized and shown in **Figure 5.4(B)**. It shows that with the increasing amount of CH_2O for synthesis, the bandgaps of the as-prepared samples slightly increased from 1.96 eV to 2.07 eV. The bandgap energies of the single-phase CuO, Cu_2O, α-Fe_2O_3 and $CuFeO_2$ are reported as 2.16 eV, [162] 1.94 – 2.02 eV, [162] 2.07 – 2.7 eV [22] and 1.55 eV [163], respectively. Thus, the bandgap energies of the $Cu_xFe_yO_z$ samples are within the bandgap range of all the composites.

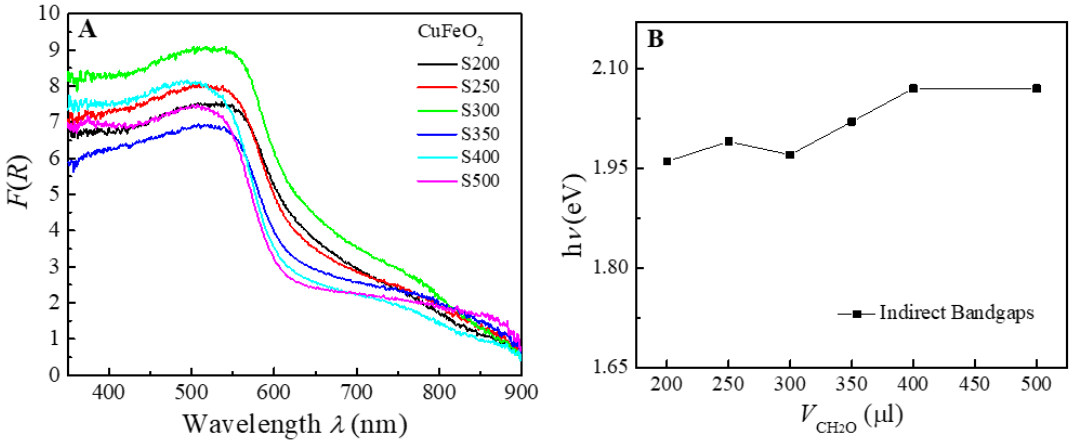

Figure 5.4. (A) UV-vis diffuse reflectance spectra of the $Cu_xFe_yO_z$ samples prepared with different CH_2O amounts. (B) The corresponding indirect bandgaps of the $Cu_xFe_yO_z$ samples from Tauc's plots.

The dye degradation activities of MO for the $Cu_xFe_yO_z$ samples are shown in **Figure 5.5(A)**. **Figure 5.5(A)** shows the time dependent standardized optical absorbance of MO solutions at λ = 463 nm (characteristic absorbance peak of MO) after exposing to different $Cu_xFe_yO_z$ samples at different time periods. According to Beer's Law, the absorbance at λ = 463 nm is propotional to the MO concentrations. It shows that after 24 hrs, S200 degrades 22% of MO, S250 degrads 71% MO, S300 degrads 76% MO, S350 degrads 85% MO, S400 degrades 61% MO and S500 degrades 90%. Clearly, S500 has the best MO degradation performance. Then, S500 was chosen to perform the MB degradation test. However, as shown in **Figure 5.5(B)**, S500 only showed 8% reduction of MB under dark conditions after 24 hrs, which is much lower than the MO reduction (90%). This is due to that the decomposition of MB is mainly through reduction reactions [164], on the other hand, the decomposition of MO is maily due to oxidation reactions [165]. The results suggest that the $Cu_xFe_yO_z$ S500 nanoparticles are a good source of oxidizing agent.

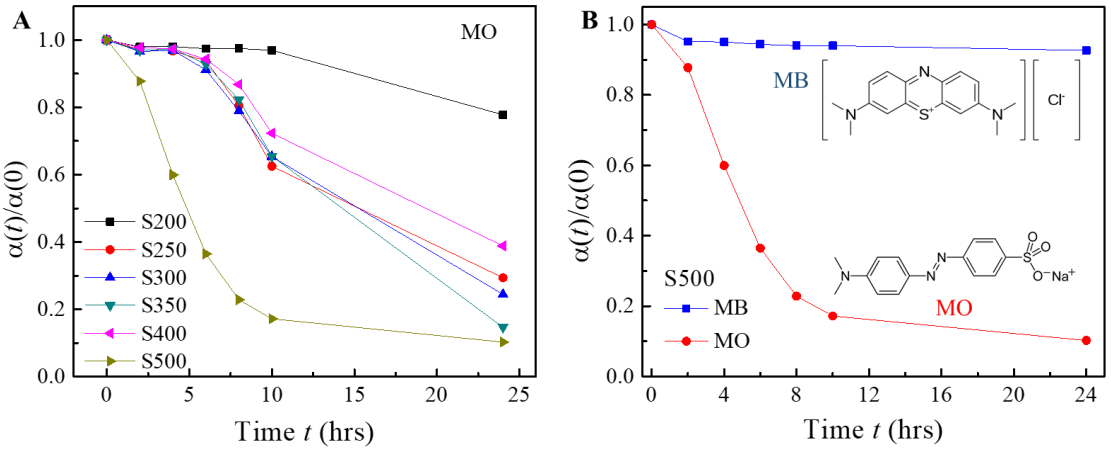

Figure 5.5. (A) The normalized optical absorbance of MO after exposure to different $Cu_xFe_yO_z$ samples at different time *t*. (B) Remaining concentrations of MO and MB after exposure to $Cu_xFe_yO_z$ S500. All the experiments were performed under dark conditions.

5.5 Antimicrobial activities and cytotoxicity

Due to the outstanding MO oxidizing activity, S500 was chosen to perform the antimicrobial tests. 9 different bacterial strains were tested, including Gram positive, Gram negative and drug resistant strains with a fixed S500 nanoparticles concentration of 1 mg/ml. **Figure 5.6** shows the time dependent bacterial survival concentration for different bacterial strains. The S500 shows highly efficient antimicrobial activities over all the strains in the antimicrobial experiments in 1X PBS. The significant bacteria killing results are summarized in **Table 5.2.** First, the tests over Gram-negative *E. coli* B showed 9 log reduction in 0.25 hrs (15 min), and 10 log reduction against Gram-positive *S. aureus* in 1 hr. The results indicate that these nanoparticles can effectively kill the bacterial cells within a very short exposure term. These fast and effective antimicrobial actives of the $Cu_xFe_yO_z$ nanoparticles motivated us to test against the highly infectious drug resistant bacterial strains, such as *K. Pneumoniae* 148 and *Salmonella* MDR-ATCC-700408. As shown in **Figure 5.6** and **Table 5.2**, the S500 also has superior antimicrobial

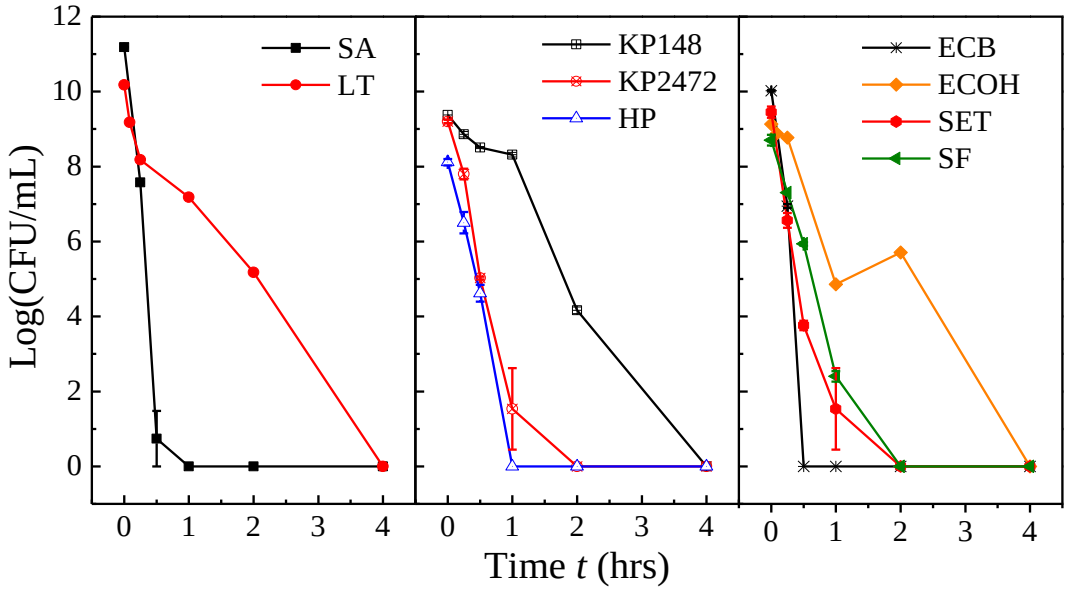

Figure 5.6. Time dependent antimicrobial tests of $Cu_xFe_yO_z$ S500 with nanoparticles concentration of 1 mg/ml in PBS.

activities against these drug resistant bacterial strains, such as 8.38 log reduction against *K. Pneumoniae* 148 and 7.15 log reduction against *Salmonella* MDR-ATCC-700408 in 4 hrs. These results indicate that these $Cu_xFe_yO_z$ nanoparticles are promising sterilizing agents for antimicrobial applications, such as for water treatments and wound treatments.

These nanoparticles can also inhibit the growth of the bacteria. **Figure 5.7** summarizes the result of the growth inhibition tests. It shows that the *H. pylori* cells are completely inhibited after 24 hrs co-culturing with the nanoparticles in the BHI-βc media, while in the control group, the *H. pylori* reaches a concentration as high as 10^8 CFU/ml without exposing to the nanoparticles. For the test against *K. pneumoniae* ATCC-BAA-2472, 4 log reduction is also obtained after 24 hrs growing. The tests gains growing *shigella flexneri*, *S. aureus* and *E. coli* also showed the effective bacterial inhibition property of the $Cu_xFe_yO_z$ nanoparticles. These tests further indicates that the S500 sample is promising as an effective antimicrobial agent.

Table 5.2. Antimicrobial activity of the $Cu_xFe_yO_z$ S500 (bacteria were suspended in 1X PBS).

Bacterial Strains	**Log Reduction**	**Time/ hrs**
E. coli B (ECB)	> 9	0.25
S. aureus (SA)	> 10.18	1
K. Pneumoniae 148 (KP148)	> 8.38	4
E. Coli O157:H7 (ECOH)	> 7.12	4
Listeria (LT)	> 9.18	4
K. pneumoniae ATCC-BAA-2472 (KP2472)	> 6.9	2
Salmonella MDR-ATCC-700408 (SET)	> 7.15	2
H. pylori X47 (HP)	> 5.81	1
S. flexneri (SF)	> 6.4	2

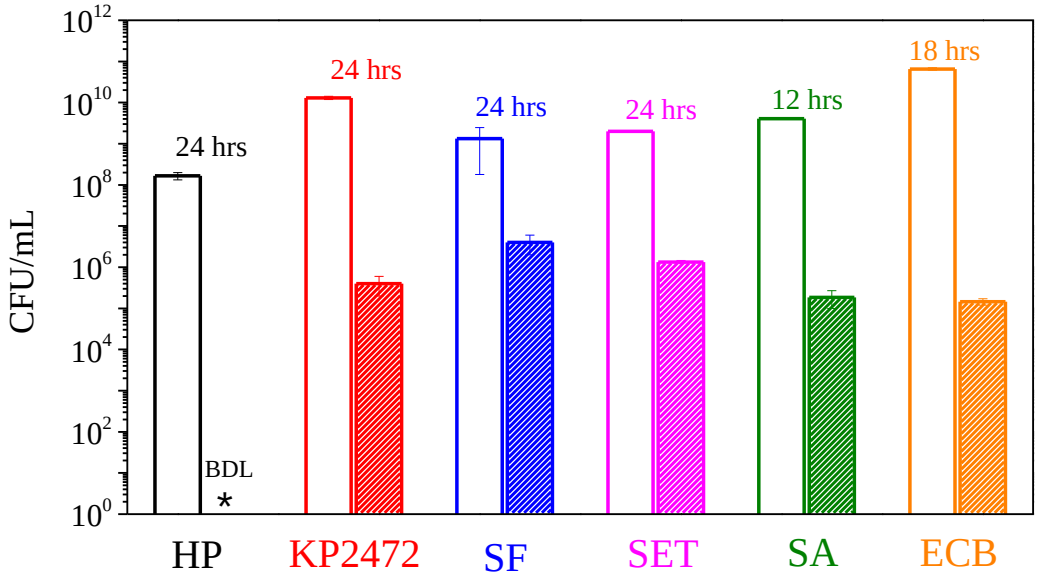

Figure 5.7. Bacterial growth inhibition tests for different bacteria: co-culturing bacteria with 1 mg/ml $Cu_xFe_yO_z$ S500 nanoparticles. BDL: below the detection limit.

The antimicrobial mechanism the $Cu_xFe_yO_z$ nanoparticles is not well understood yet. However, based on the composition in S500, the antimicrobial property might be mostly contributed by the Cu_2O and $CuFeO_2$. For those two materials, the antimicrobial properties are attributed to Cu^+ species in the compounds. [166] It is well-known that copper ions are capable to kill microorganisms effectively by denaturation or an oxidation mechanism. [37] It was reported that Cu_2O nanocrystals could generate ROS through biochemical processes. [167] In general, during these biochemical processes, as a redox-active transition metal, Cu can cycle between two redox states, oxidized cupric and reduced cuprous states. It is suggested that Cu can react with endogenous H_2O_2 to generate hydroxyl radicals in a process analogous to the Fenton reaction, and it can also catalyze the transfer of electrons from a donor biomolecule to an acceptor, such as O_2 to generate $O_2^{-\bullet}$ or hydroxyl radicals (·OH). [167-168] These ROS are toxic to bacterial cells, which can disrupt specific microbial processes. The direct effects of ROS on bacterial cells are

mediated by the increasing production of ROS can lead to the oxidative damage of the cellular compounds. [63] Studies showed that the ROS can cause the damage of cell membrane, cause the leaking of bacterial internals, then lead to the cell death. [62, 74] Furthermore, the ROS can interfere or destroy the activities of enzymes in the bacterial cells. They can also cause damages on the integrity of DNA. [62, 64] It should keep in mind that high concentration of ROS can also trigger the damage on mammalian cells. Thus, the cytotoxicity of the $Cu_xFe_yO_z$ S500 nanoparticles against mammalian cells are necessary to be performed as a condition to explore its potential applications.

Biocompatibility of the $Cu_xFe_yO_z$ S500 nanoparticles are tested by the 24 hrs nanoparticles exposure at 37 ^oC using mouse fibroblast cells. As shown in **Figure 5.8**, fibroblast cells that were treated with 10 mg/ml $Cu_xFe_yO_z$ nanoparticles showed more than 90% cell viability decreasing. However, with the treatment of 1 mg/ml S500 nanoparticles, more than 70 % cell remains viable. Comparing with other antimicrobial inorganic materials, for example CuO nanoparticles, it was reported that at a concentration of 80 μg/ml, the CuO nanoparticles are toxic to the lung cells and can also cause DNA damage to the cells. [169] The presented data suggest that the as-synthesized$Cu_xFe_yO_z$ S500 is toxic to the mouse fibroblasts when used at a high concentration (i.e., 10 mg/ml). However, at a lower nanoparticles concentration of 1 mg/ml, the $Cu_xFe_yO_z$ S500 is biocompatible. At mean time, as described in the previous sections, 1 mg/ml $Cu_xFe_yO_z$ S500 showed highly efficient antimicrobial activities against a wide range of microorganisms.

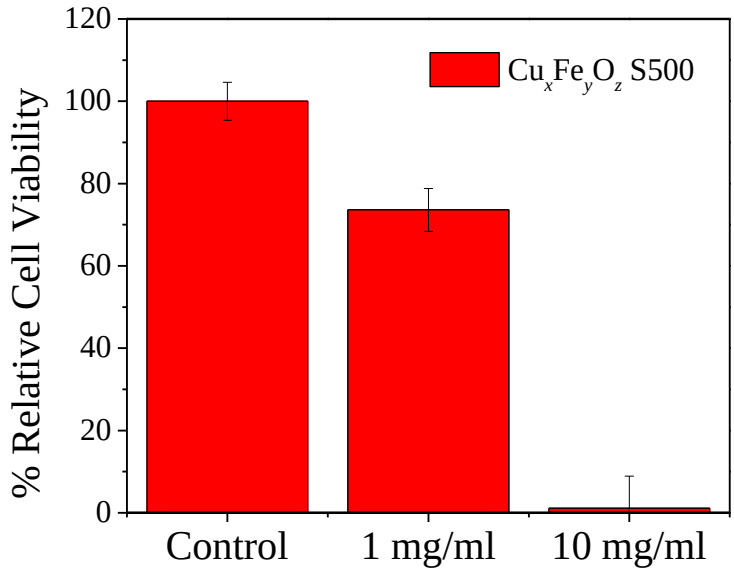

Figure 5.8. Cytotoxicity of the $Cu_xFe_yO_z$ S500 nanoparticles against mouse fibroblast cells: cell viability after cells exposed to $Cu_xFe_yO_z$ S500 particles at 1 mg/ml and 10 mg/ml for 24 hrs.

5.6 Conclusions

In summary, we have synthesized 6 different nanostructured $Cu_xFe_yO_z$ mixtures through a microwave assisted hydrothermal synthesizes. The changing of CH_2O amount during synthesis changes the morphology and the composition of the as-synthesized samples. The EDS and XRD results confirm that the samples are mixtures of CuO, Cu_2O, Fe_2O_3 and $CuFeO_2$ nanostructures. It also shows that with the increasing of CH_2O addition amount, the particle size decreases, while the CuO in the decreases, and Cu_2O increases. The dye degradation tests shows that nanoparticles fabricated with 500 µl CH_2O could degrade 90% MO after 24 hrs under dark conditions, and it is a strong oxidizing agent. This S500 sample also shows highly effective antimicrobial activities against multi bacterial strains. In particular, it can cause 9 log reduction of *E. coli* B in 15 min, and 10 log reduction of *S. aureus* in 1 hr. More importantly, the highly drug-resistant bacterial strains such as *K. Pneumoniae* 148 and *H. pylori* X47 can also be removed within 4 hrs. The inhibition

tests with growing cells and 1 mg/ml S500 nanoparticles in fresh media further demonstrates that this sample is highly antimicrobial effective. The cytotoxicity test against mouse fibroblast cells suggested that the $Cu_xFe_yO_z$ S500 at the concentration of 1 mg/ml are biocompatible.

CHAPTER 6

CONCLUSIONS AND FUTURE WORK

Even though throughout the history, the development of antimicrobial agents has achieved many major breakthroughs, the growing bacterial resistance of antibiotics remains one of the major challenges. As one of the promising materials to solve this problem, inorganic nanomaterials are chosen to study its antimicrobial properties in this dissertation.

In this dissertation, the antimicrobial activities of three inorganic materials, including carbon dots, $CuBi_2O_4$, and $Cu_xFe_yO_z$ are studied. Their morphological, structural, optical, and dye degradation are explored. The visible light induced photocatalytic activities of carbon dots and $CuBi_2O_4$ nanostructures and the antimicrobial activity of the $Cu_xFe_yO_z$ nanostrucutres induced by oxidative stress are further investigated. More specifically, the carbon nano dots with a size ~ 5 nm have been modified with surface passivation EDA molecules first. The photoexited electrons and holes can be trapped at different passivated sites, then to be used to generate ROS to degrade organic dye (MB) molecules. The followed visible light induced antimicrobial activities of the EDA-carbon dots carried out by different methods (OD600, growth inhibition, killing experiment and co-culturing on plates) demonstrate that with the efficient surface passivation, the carbon dots can be served as visible light-activated bactericidal agents for a variety of bacteria control applications. It shows that with visible light, the EDA-carbon dots can cause 4 logs of *E. coli* reduction after 30 min treatment. For the case of $CuBi_2O_4$ nanostructures, with the different hydrothermal synthesis recipes, the morphologies of the resulted samples are varied. The photocatalytic properties of these materials are closely related to the crystallinity, total active

surface area, and other factors. The crystallinity and total active surface area can affect the light absorption and charge generation properties, charge diffusion length, and transportation on the surfaces of the material. For better photocatalytic activity, the electron–hole pairs should be efficiently separated, and charges should be rapidly transferred across the surface/interface to restrain the recombination. Increasing the surface area of the photocatalyst, can help reduce the electron–hole recombination and shorten the transportation distance to the photocatalyst surface, a larger surface area can also contribute to more reaction sites. As demonstrated by the experimental results, the hierarchical micro-flower $CuBi_2O_4$ samples out of five samples has the largest surface area, and it has demonstrated the best visible light induced antimicrobial performance as well as good solar-energy conversion into electrical energy under a solar simulator at a minimum external bias voltage and at a neutral pH value. A high antibacterial effect against *Escherichia coli* (*E. coli*), with ~ 93% bacteria reduction after 6 h illumination by a commercial white LED light (10 mW/cm^2), is obtained with the $CuBi_2O_4$ micro-flowers. Thus, future work of the carbon dots can be focused on more effective surface modification. In the case of $CuBi_2O_4$, works on designing smaller particle size might be able to help further improve the photocatalytic properties.

Other than the photogenerated ROS, some of the metal oxides can also directly induce oxidative stress to inhibit bacterial growth. Six different $Cu_xFe_yO_z$ samples are synthesized by microwave-assisted hydrothermal synthesis method. Their morphological, structural, and other properties are characterized. The results indicate that with the increasing of CH_2O for synthesis, the particle size of the products decreases, the composition of the products also varies. Their abilities of dye (MO) degradation (oxidation) are investigated and the results show that sample S500 has the best MO degradation ability (90% reduction in 24 hrs). The antimicrobial tests with

S500 at a concentration of 1mg/ml demonstrate that it is a highly effective antimicrobial agent against multi-bacterial strains. It shows that *E. coli* B with a concentration of 10^9 CFU/ml in PBS can be terminated in 15 min, and *S. aureus* with a concentration of 10^{10} CFU/ml can be eliminated in 1 hr. Highly drug-resistant bacterial strains such as *K. Pneumoniae* 148 and *H. pylori* X47 can also be removed within 4 hrs. With 1 mg/ml S500 in the fresh media, the growth of different bacterial strains are also inhibited effectively. We also find that the $Cu_xFe_yO_z$ S500 sample at the concentration of 1 mg/ml are biocompatible. All of these works indicate that inorganic nanomaterials are promising to solve the problems caused by the increasing the bacterial resistance of antibiotics. The future work of the $Cu_xFe_yO_z$ can be directed to fabricate smaller particles and exploring its applications. For example, it is important to study how to incorporate these materials into fabrics, plastics, gels or coat these materials onto surfaces to create sterile environment. Furthermore, since biofilm is one of the major threatens to human health, the capabilities to control the biofilm formation of these inorganic antimicrobial materials are important to justify their value in practical applications, such as wound treatments and medical device coating. On the other hand, by using the hydrothermal method, other inorganic antimicrobial nanomaterials can be explored and studied.

REFERENCES

1. Fauci, A. S., Infectious diseases: considerations for the 21st century. *Clinical Infectious Diseases* **2001,** *32* (5), 675-685.
2. Organization, W. H., *The world health report 2000: health systems: improving performance*. World Health Organization: 2000.
3. Pinner, R. W.; Teutsch, S. M.; Simonsen, L.; Klug, L. A.; Graber, J. M.; Clarke, M. J.; Berkelman, R. L., Trends in infectious diseases mortality in the United States. *Jama* **1996,** *275* (3), 189-193.
4. Scallan, E.; Hoekstra, R. M.; Angulo, F. J.; Tauxe, R. V.; Widdowson, M. A.; Roy, S. L.; Jones, J. L.; Griffin, P. M., Foodborne Illness Acquired in the United States-Major Pathogens. *Emerg. Infect. Dis* **2011,** *17* (1), 7-15.
5. Dillow, A. K.; Dehghani, F.; Hrkach, J. S.; Foster, N. R.; Langer, R., Bacterial inactivation by using near-and supercritical carbon dioxide. *Proceedings of the National Academy of Sciences* **1999,** *96* (18), 10344-10348.
6. Saga, T.; Yamaguchi, K., History of antimicrobial agents and resistant bacteria. JMAJ: 2009; pp 103-108.
7. FY15 Detect and Protect Against Antibiotic Resistance Budget Initiative. Centers for Disease Control and Prevention: Atlanta, G., Ed. 2003.
8. Hamblin, M. R.; Hasan, T., Photodynamic therapy: a new antimicrobial approach to infectious disease? *Photochemical & Photobiological Sciences* **2004,** *3* (5), 436-450.

9. Furno, F.; Morley, K. S.; Wong, B.; Sharp, B. L.; Arnold, P. L.; Howdle, S. M.; Bayston, R.; Brown, P. D.; Winship, P. D.; Reid, H. J., Silver nanoparticles and polymeric medical devices: a new approach to prevention of infection? *Journal of Antimicrobial Chemotherapy* **2004,** *54* (6), 1019-1024.

10. Marambio-Jones, C.; Hoek, E. M., A review of the antibacterial effects of silver nanomaterials and potential implications for human health and the environment. *Journal of Nanoparticle Research* **2010,** *12* (5), 1531-1551.

11. Dastjerdi, R.; Montazer, M., A review on the application of inorganic nano-structured materials in the modification of textiles: focus on anti-microbial properties. *Colloids and Surfaces B: Biointerfaces* **2010,** *79* (1), 5-18.

12. Wang, W.; Huang, G.; Yu, J. C.; Wong, P. K., Advances in photocatalytic disinfection of bacteria: Development of photocatalysts and mechanisms. *Journal of environmental sciences (China)* **2015,** *34*, 232-47.

13. Nararom, M.; Thepa, S.; Kongkiattikajorn, J.; Songprakorp, R., Disinfection of water containing Escherichia coli by use of a compound parabolic concentrator: effect of global solar radiation and reactor surface treatment. *Research on Chemical Intermediates* **2015,** *41* (9), 6543-6558.

14. Marugan, J.; van Grieken, R.; Pablos, C.; Lucila Satuf, M.; Cassano, A. E.; Alfano, O. M., Photocatalytic inactivation of Escherichia coli aqueous suspensions in a fixed-bed reactor. *Catalysis Today* **2015,** *252*, 143-149.

15. Markowska-Szczupak, A.; Ulfig, K.; Morawski, A. W., The application of titanium dioxide for deactivation of bioparticulates: An overview. *Catalysis Today* **2011,** *169* (1), 249-257.

16. Liou, J.-W.; Chang, H.-H., Bactericidal Effects and Mechanisms of Visible Light-Responsive Titanium Dioxide Photocatalysts on Pathogenic Bacteria. *Archivum Immunologiae Et Therapiae Experimentalis* **2012,** *60* (4), 267-275.

17. Li, Q.; Mahendra, S.; Lyon, D. Y.; Brunet, L.; Liga, M. V.; Li, D.; Alvarez, P. J. J., Antimicrobial nanomaterials for water disinfection and microbial control: Potential applications and implications. *Water Research* **2008,** *42* (18), 4591-4602.

18. Janpetch, N.; Vanichvattanadecha, C.; Rujiravanit, R., Photocatalytic disinfection of water by bacterial cellulose/N-F co-doped TiO2 under fluorescent light. *Cellulose* **2015,** *22* (5), 3321-3335.

19. Bogdan, J.; Zarzynska, J.; Plawinska-Czarnak, J., Comparison of Infectious Agents Susceptibility to Photocatalytic Effects of Nanosized Titanium and Zinc Oxides: A Practical Approach. *Nanoscale Research Letters* **2015,** *10*.

20. Amin, M. T.; Alazba, A. A., A review of nanomaterials based membranes for removal of contaminants from polluted waters. *Membrane Water Treatment* **2014,** *5* (2), 123-146.

21. Hossain, F.; Perales-Perez, O. J.; Hwang, S.; Roman, F., Antimicrobial nanomaterials as water disinfectant: Applications, limitations and future perspectives. *Science of The Total Environment* **2014,** *466*, 1047-1059.

22. Basnet, P.; Larsen, G. K.; Jadeja, R. P.; Hung, Y.-C.; Zhao, Y., α-Fe2O3 Nanocolumns and Nanorods Fabricated by Electron Beam Evaporation for Visible Light Photocatalytic and Antimicrobial Applications. *ACS Applied Materials & Interfaces* **2013,** *5* (6), 2085-2095.

23. Liu, S.; Huang, G.; Yu, J.; Ng, T. W.; Yip, H. Y.; Wong, P. K., Porous Fluorinated SnO2 Hollow Nanospheres: Transformative Self-assembly and Photocatalytic Inactivation of Bacteria. *Acs Applied Materials & Interfaces* **2014,** *6* (4), 2407-2414.

24. Daneshvar, N.; Salari, D.; Khataee, A. R., Photocatalytic degradation of azo dye acid red 14 in water on ZnO as an alternative catalyst to TiO2. *Journal of Photochemistry and Photobiology a-Chemistry* **2004,** *162* (2-3), 317-322.

25. Fujishima, A.; Honda, K., Electrochemical photolysis of water at a semiconductor electrode. *Nature* **1972,** *238* (5358), 37-38.

26. Matsunaga, T.; Tomoda, R.; Nakajima, T.; Wake, H., PHOTOELECTROCHEMICAL STERILIZATION OF MICROBIAL-CELLS BY SEMICONDUCTOR POWDERS. *Fems Microbiology Letters* **1985,** *29* (1-2), 211-214.

27. Liu, M.; Qiu, X.; Miyauchi, M.; Hashimoto, K., Energy-Level Matching of Fe(III) Ions Grafted at Surface and Doped in Bulk for Efficient Visible-Light Photocatalysts. *Journal of the American Chemical Society* **2013,** *135* (27), 10064-10072.

28. Wong, M.-S.; Chu, W.-C.; Sun, D.-S.; Huang, H.-S.; Chen, J.-H.; Tsai, P.-J.; Lin, N.-T.; Yu, M.-S.; Hsu, S.-F.; Wang, S.-L.; Chang, H.-H., Visible-light-induced bactericidal activity of a nitrogen-doped titanium photocatalyst against human pathogens. *Applied and Environmental Microbiology* **2006,** *72* (9), 6111-6116.

29. Xu, J.-W.; Gao, Z.-D.; Han, K.; Liu, Y.; Song, Y.-Y., Synthesis of Magnetically Separable Ag3PO4/TiO2/Fe3O4 Heterostructure with Enhanced Photocatalytic Performance under Visible Light for Photoinactivation of Bacteria. *Acs Applied Materials & Interfaces* **2014,** *6* (17), 15122-15131.

30. Kang, J.; Kuang, Q.; Xie, Z.-X.; Zheng, L.-S., Fabrication of the SnO2/alpha-Fe2O3 Hierarchical Heterostructure and Its Enhanced Photocatalytic Property. *Journal of Physical Chemistry C* **2011,** *115* (16), 7874-7879.

31. Chen, C.; Cai, W.; Long, M.; Zhou, B.; Wu, Y.; Wu, D.; Feng, Y., Synthesis of Visible-Light Responsive Graphene Oxide/TiO2 Composites with p/n Heterojunction. *Acs Nano* **2010,** *4* (11), 6425-6432.

32. Yu, X.; Liu, J.; Yu, Y.; Zuo, S.; Li, B., Preparation and visible light photocatalytic activity of carbon quantum dots/TiO2 nanosheet composites. *Carbon* **2014,** *68*, 718-724.

33. Zhou, X.; Jin, B.; Li, L.; Peng, F.; Wang, H.; Yu, H.; Fang, Y., A carbon nitride/TiO2 nanotube array heterojunction visible-light photocatalyst: synthesis, characterization, and photoelectrochemical properties. *Journal of Materials Chemistry* **2012,** *22* (34), 17900-17905.

34. Qiu, X.; Miyauchi, M.; Sunada, K.; Minoshima, M.; Liu, M.; Lu, Y.; Li, D.; Shimodaira, Y.; Hosogi, Y.; Kuroda, Y.; Hashimoto, K., Hybrid CuxO/TiO2 Nanocomposites As Risk-Reduction Materials in Indoor Environments. *Acs Nano* **2012,** *6* (2), 1609-1618.

35. Yi, Z.; Ye, J.; Kikugawa, N.; Kako, T.; Ouyang, S.; Stuart-Williams, H.; Yang, H.; Cao, J.; Luo, W.; Li, Z.; Liu, Y.; Withers, R. L., An orthophosphate semiconductor with photooxidation properties under visible-light irradiation. *Nature Materials* **2010,** *9* (7), 559-564.

36. Yang, X.; Qin, J.; Jiang, Y.; Chen, K.; Yan, X.; Zhang, D.; Li, R.; Tang, H., Fabrication of P25/Ag3PO4/graphene oxide heterostructures for enhanced solar photocatalytic degradation of organic pollutants and bacteria. *Applied Catalysis B-Environmental* **2015,** *166*, 231-240.

37. Bai, H.; Liu, Z.; Sun, D. D., Hierarchical ZnO/Cu “corn-like” materials with high photodegradation and antibacterial capability under visible light. *Physical Chemistry Chemical Physics* **2011,** *13* (13), 6205-6210.

38. Gao, P.; Liu, J.; Sun, D. D.; Ng, W., Graphene oxide–CdS composite with high photocatalytic degradation and disinfection activities under visible light irradiation. *Journal of hazardous materials* **2013,** *250*, 412-420.

39. Xiang, Q.; Yu, J.; Jaroniec, M., Preparation and enhanced visible-light photocatalytic H2-production activity of graphene/C3N4 composites. *The Journal of Physical Chemistry C* **2011,** *115* (15), 7355-7363.

40. Zhu, M.; Chen, P.; Liu, M., Graphene oxide enwrapped Ag/AgX (X= Br, Cl) nanocomposite as a highly efficient visible-light plasmonic photocatalyst. *ACS nano* **2011,** *5* (6), 4529-4536.

41. Baker, C.; Pradhan, A.; Pakstis, L.; Pochan, D. J.; Shah, S. I., Synthesis and antibacterial properties of silver nanoparticles. *Journal of nanoscience and nanotechnology* **2005,** *5* (2), 244-249.

42. Esteban-Cubillo, A.; Pecharromán, C.; Aguilar, E.; Santarén, J.; Moya, J. S., Antibacterial activity of copper monodispersed nanoparticles into sepiolite. *Journal of Materials Science* **2006,** *41* (16), 5208-5212.

43. Jia, B.; Mei, Y.; Cheng, L.; Zhou, J.; Zhang, L., Preparation of copper nanoparticles coated cellulose films with antibacterial properties through one-step reduction. *ACS applied materials & interfaces* **2012,** *4* (6), 2897-2902.

44. Delgado, K.; Quijada, R.; Palma, R.; Palza, H., Polypropylene with embedded copper metal or copper oxide nanoparticles as a novel plastic antimicrobial agent. *Letters in applied microbiology* **2011,** *53* (1), 50-54.

45. Perelshtein, I.; Applerot, G.; Perkas, N.; Wehrschuetz-Sigl, E.; Hasmann, A.; Guebitz, G.; Gedanken, A., CuO–cotton nanocomposite: Formation, morphology, and antibacterial activity. *Surface and Coatings Technology* **2009,** *204* (1-2), 54-57.

46. Saravanan, R.; Khan, M. M.; Gupta, V. K.; Mosquera, E.; Gracia, F.; Narayanan, V.; Stephen, A., ZnO/Ag/Mn 2 O 3 nanocomposite for visible light-induced industrial textile effluent degradation, uric acid and ascorbic acid sensing and antimicrobial activity. *RSC Advances* **2015,** *5* (44), 34645-34651.

47. Rogers, K., *Bacteria and Viruses*. Britannica Educational Publishing: 2010.

48. Koch, A. L., *The bacteria: their origin, structure, function and antibiosis*. Springer Science & Business Media: 2007.

49. Meroueh, S. O.; Bencze, K. Z.; Hesek, D.; Lee, M.; Fisher, J. F.; Stemmler, T. L.; Mobashery, S., Three-dimensional structure of the bacterial cell wall peptidoglycan. *Proceedings of the National Academy of Sciences of the United States of America* **2006,** *103* (12), 4404-4409.

50. Silhavy, T. J.; Kahne, D.; Walker, S., The bacterial cell envelope. *Cold Spring Harbor perspectives in biology* **2010,** *2* (5), a000414.

51. Blancou, J., History of disinfection from early times until the end of the 18th century. *Revue Scientifique et Technique-Office International des Epizooties* **1995,** *14*, 31-31.

52. Jayaraman, R., Antibiotic resistance: an overview of mechanisms and a paradigm shift. *Current Science* **2009**, 1475-1484.

53. Pelaez, F., The historical delivery of antibiotics from microbial natural products—can history repeat? *Biochemical pharmacology* **2006,** *71* (7), 981-990.

54. Yocum, R. R.; Rasmussen, J. R.; Strominger, J. L., The mechanism of action of penicillin. Penicillin acylates the active site of Bacillus stearothermophilus D-alanine carboxypeptidase. *Journal of Biological Chemistry* **1980,** *255* (9), 3977-3986.

55. Penicillin. https://en.wikipedia.org/wiki/Penicillin.

56. Blair, J. M.; Webber, M. A.; Baylay, A. J.; Ogbolu, D. O.; Piddock, L. J., Molecular mechanisms of antibiotic resistance. *Nature Reviews Microbiology* **2015,** *13* (1), 42-51.

57. Dizaj, S. M.; Lotfipour, F.; Barzegar-Jalali, M.; Zarrintan, M. H.; Adibkia, K., Antimicrobial activity of the metals and metal oxide nanoparticles. *Materials Science and Engineering: C* **2014,** *44*, 278-284.

58. Fujishima, A.; Honda, K., TiO2 photoelectrochemistry and photocatalysis. *Nature* **1972,** *238* (5358), 37-38.

59. Ismail, A. A.; Bahnemann, D. W., Photochemical splitting of water for hydrogen production by photocatalysis: A review. *Solar Energy Materials and Solar Cells* **2014,** *128*, 85-101.

60. Abe, R., Recent progress on photocatalytic and photoelectrochemical water splitting under visible light irradiation. *Journal of Photochemistry and Photobiology C-Photochemistry Reviews* **2010,** *11* (4), 179-209.

61. Yadav, H. M.; Kim, J.-S.; Pawar, S. H., Developments in photocatalytic antibacterial activity of nano TiO2: A review. *Korean Journal of Chemical Engineering* **2016,** *33* (7), 1989-1998.

62. Wu, P.; Imlay, J. A.; Shang, J. K., Mechanism of Escherichia coli inactivation on palladium-modified nitrogen-doped titanium dioxide. *Biomaterials* **2010,** *31* (29), 7526-7533.

63. von Moos, N.; Slaveykova, V. I., Oxidative stress induced by inorganic nanoparticles in bacteria and aquatic microalgae–state of the art and knowledge gaps. *Nanotoxicology* **2014,** *8* (6), 605-630.

64. Imlay, J. A., The molecular mechanisms and physiological consequences of oxidative stress: lessons from a model bacterium. *Nature Reviews Microbiology* **2013,** *11* (7), 443-454.

65. Ingle, A. P.; Duran, N.; Rai, M., Bioactivity, mechanism of action, and cytotoxicity of copper-based nanoparticles: a review. *Applied microbiology and biotechnology* **2014,** *98* (3), 1001-1009.

66. Sondi, I.; Salopek-Sondi, B., Silver nanoparticles as antimicrobial agent: a case study on E. coli as a model for Gram-negative bacteria. *Journal of colloid and interface science* **2004,** *275* (1), 177-182.

67. Li, Q.; Mahendra, S.; Lyon, D. Y.; Brunet, L.; Liga, M. V.; Li, D.; Alvarez, P. J., Antimicrobial nanomaterials for water disinfection and microbial control: potential applications and implications. *Water research* **2008,** *42* (18), 4591-4602.

68. Rai, M.; Yadav, A.; Gade, A., Silver nanoparticles as a new generation of antimicrobials. *Biotechnology advances* **2009,** *27* (1), 76-83.

69. Le Ouay, B.; Stellacci, F., Antibacterial activity of silver nanoparticles: a surface science insight. *Nano Today* **2015,** *10* (3), 339-354.

70. Carlson, C.; Hussain, S. M.; Schrand, A. M.; K. Braydich-Stolle, L.; Hess, K. L.; Jones, R. L.; Schlager, J. J., Unique cellular interaction of silver nanoparticles: size-dependent generation of reactive oxygen species. *The journal of physical chemistry B* **2008,** *112* (43), 13608-13619.

71. Parikh, A.; Gillmor, S.; Beers, J.; Beardmore, K.; Cutts, R.; Swanson, B., Characterization of chain molecular assemblies in long-chain, layered silver thiolates: a joint infrared spectroscopy and X-ray diffraction study. *The Journal of Physical Chemistry B* **1999,** *103* (15), 2850-2861.

72. Zhang, W.; Yao, Y.; Sullivan, N.; Chen, Y., Modeling the primary size effects of citrate-coated silver nanoparticles on their ion release kinetics. *Environmental science & technology* **2011,** *45* (10), 4422-4428.

73. Ahamed, M.; Alhadlaq, H. A.; Khan, M.; Karuppiah, P.; Al-Dhabi, N. A., Synthesis, characterization, and antimicrobial activity of copper oxide nanoparticles. *Journal of Nanomaterials* **2014,** *2014*.

74. Applerot, G.; Lellouche, J.; Lipovsky, A.; Nitzan, Y.; Lubart, R.; Gedanken, A.; Banin, E., Understanding the antibacterial mechanism of CuO nanoparticles: revealing the route of induced oxidative stress. *Small* **2012,** *8* (21), 3326-3337.

75. Gunawan, C.; Teoh, W. Y.; Marquis, C. P.; Amal, R., Cytotoxic origin of copper (II) oxide nanoparticles: comparative studies with micron-sized particles, leachate, and metal salts. *ACS nano* **2011,** *5* (9), 7214-7225.

76. Lemire, J. A.; Harrison, J. J.; Turner, R. J., Antimicrobial activity of metals: mechanisms, molecular targets and applications. *Nature Reviews Microbiology* **2013,** *11* (6), 371-384.

77. Feng, S.; Xu, R., New materials in hydrothermal synthesis. *Accounts of chemical research* **2001,** *34* (3), 239-247.

78. Byrappa, K.; Adschiri, T., Hydrothermal technology for nanotechnology. *Progress in Crystal Growth and Characterization of Materials* **2007,** *53* (2), 117-166.

79. Suchanek, W. L.; Riman, R. E. In *Hydrothermal synthesis of advanced ceramic powders*, Advances in Science and Technology, Trans Tech Publ: 2006; pp 184-193.

80. Byrappa, K.; Yoshimura, M., *Handbook of hydrothermal technology*. William Andrew: 2012.

81. Habashi, F., *A textbook of hydrometallurgy*. Métallurgie Extractive Québec: 1999.

82. Yoshimura, M.; Byrappa, K., Hydrothermal processing of materials: past, present and future. *Journal of Materials Science* **2008,** *43* (7), 2085-2103.

83. Yoshimura, M.; Suchanek, W. L.; Byrappa, K., Soft solution processing: a strategy for one-step processing of advanced inorganic materials. *MRS Bulletin* **2000,** *25* (9), 17-25.

84. Byrappa, K.; Namratha, K.; Byrappa, N. M., Hydrothermal Technology for Processing of Advanced Functional Materials. *Kirk-Othmer Encyclopedia of Chemical Technology* **2005**.

85. Daou, T.; Pourroy, G.; Bégin-Colin, S.; Greneche, J.; Ulhaq-Bouillet, C.; Legaré, P.; Bernhardt, P.; Leuvrey, C.; Rogez, G., Hydrothermal synthesis of monodisperse magnetite nanoparticles. *Chemistry of Materials* **2006,** *18* (18), 4399-4404.

86. Diao, K.; Zhang, J.; Zhou, M.; Tang, Y.; Wang, S.; Cui, X., Highly controllable and reproducible ZnO nanowire arrays growth with focused ion beam and low-temperature hydrothermal method. *Applied Surface Science* **2014,** *317*, 220-225.

87. Salavati-Niasari, M.; Mir, N.; Davar, F., ZnO nanotriangles: Synthesis, characterization and optical properties. *Journal of Alloys and Compounds* **2009,** *476* (1-2), 908-912.

88. Han, J.; Niu, Y.; Bao, S.-j.; Yu, Y.-N.; Lu, S.-Y.; Xu, M., Nanocubic KTi 2 (PO 4) 3 electrodes for potassium-ion batteries. *Chemical Communications* **2016,** *52* (78), 11661-11664.

89. Wu, T.; Liu, Y.; Zeng, X.; Cui, T.; Zhao, Y.; Li, Y.; Tong, G., Facile hydrothermal synthesis of Fe3O4/C core–shell nanorings for efficient low-frequency microwave absorption. *ACS applied materials & interfaces* **2016,** *8* (11), 7370-7380.

90. Wang, X.; Li, Y., Selected-control hydrothermal synthesis of α-and β-MnO2 single crystal nanowires. *Journal of the American Chemical Society* **2002,** *124* (12), 2880-2881.

91. Zhao, Q.; Wang, T.; Wang, J.; Zheng, L.; Jiang, T.; Cheng, G.; Wang, S., Template-directed hydrothermal synthesis of hydroxyapatite as a drug delivery system for the poorly water-soluble drug carvedilol. *Applied Surface Science* **2011,** *257* (23), 10126-10133.

92. Meligrana, G.; Gerbaldi, C.; Tuel, A.; Bodoardo, S.; Penazzi, N., Hydrothermal synthesis of high surface LiFePO4 powders as cathode for Li-ion cells. *Journal of Power Sources* **2006,** *160* (1), 516-522.

93. Yu, J.; Yu, X., Hydrothermal synthesis and photocatalytic activity of zinc oxide hollow spheres. *Environmental science & technology* **2008,** *42* (13), 4902-4907.

94. Fang, Y.; Gu, D.; Zou, Y.; Wu, Z.; Li, F.; Che, R.; Deng, Y.; Tu, B.; Zhao, D., A Low‐Concentration Hydrothermal Synthesis of Biocompatible Ordered Mesoporous Carbon Nanospheres with Tunable and Uniform Size. *Angewandte Chemie International Edition* **2010,** *49* (43), 7987-7991.

95. Charnay, C.; Bégu, S.; Tourné-Péteilh, C.; Nicole, L.; Lerner, D.; Devoisselle, J.-M., Inclusion of ibuprofen in mesoporous templated silica: drug loading and release property. *European Journal of Pharmaceutics and Biopharmaceutics* **2004,** *57* (3), 533-540.

96. Zhang, C.; Li, C.; Huang, S.; Hou, Z.; Cheng, Z.; Yang, P.; Peng, C.; Lin, J., Self-activated luminescent and mesoporous strontium hydroxyapatite nanorods for drug delivery. *Biomaterials* **2010,** *31* (12), 3374-3383.

97. Lencka, M. M.; Anderko, A.; Riman, R. E., Hydrothermal precipitation of lead zirconate titanate solid solutions: thermodynamic modeling and experimental synthesis. *Journal of the American Ceramic Society* **1995,** *78* (10), 2609-2618.

98. Lencka, M. M.; Nielsen, E.; Anderko, A.; Riman, R. E., Hydrothermal synthesis of carbonate-free strontium zirconate: thermodynamic modeling and experimental verification. *Chemistry of materials* **1997,** *9* (5), 1116-1125.

99. Bilecka, I.; Niederberger, M., Microwave chemistry for inorganic nanomaterials synthesis. *Nanoscale* **2010,** *2* (8), 1358-1374.

100. Kappe, C. O.; Dallinger, D.; Murphree, S. S., *Practical microwave synthesis for organic chemists: strategies, instruments, and protocols*. John Wiley & Sons: 2008.

101. Baghbanzadeh, M.; Carbone, L.; Cozzoli, P. D.; Kappe, C. O., Microwave‐assisted synthesis of colloidal inorganic nanocrystals. *Angewandte Chemie International Edition* **2011,** *50* (48), 11312-11359.

102. Kappe, C.; Dallinger, D.; Murphree, S., Practical microwave synthesis for organic chemists 2009. Wiley-VCH: Weinheim.

103. Faraji, S.; Ani, F. N., Microwave-assisted synthesis of metal oxide/hydroxide composite electrodes for high power supercapacitors–a review. *Journal of Power Sources* **2014,** *263*, 338-360.

104. Kappe, C. O., Kontrolliertes Erhitzen mit Mikrowellen in der modernen organischen Synthese. *Angewandte Chemie* **2004,** *116* (46), 6408-6443.

105. Kappe, C. O., Controlled microwave heating in modern organic synthesis. *Angewandte Chemie International Edition* **2004,** *43* (46), 6250-6284.

106. Chen, K.; Dong Noh, Y.; Li, K.; Komarneni, S.; Xue, D., Microwave–hydrothermal crystallization of polymorphic MnO2 for electrochemical energy storage. *The Journal of Physical Chemistry C* **2013,** *117* (20), 10770-10779.

107. Hu, X.; Yu, J. C.; Gong, J.; Li, Q.; Li, G., α‐Fe2O3 nanorings prepared by a microwave‐assisted hydrothermal process and their sensing properties. *Advanced Materials* **2007,** *19* (17), 2324-2329.

108. Wang, Y.; Yu, J.; Xiao, W.; Li, Q., Microwave-assisted hydrothermal synthesis of graphene based Au–TiO 2 photocatalysts for efficient visible-light hydrogen production. *Journal of Materials Chemistry A* **2014,** *2* (11), 3847-3855.

109. Qi, C.; Zhu, Y. J.; Lu, B. Q.; Zhao, X. Y.; Zhao, J.; Chen, F.; Wu, J., Hydroxyapatite Hierarchically Nanostructured Porous Hollow Microspheres: Rapid, Sustainable Microwave‐Hydrothermal Synthesis by Using Creatine Phosphate as an Organic Phosphorus Source and Application in Drug Delivery and Protein Adsorption. *Chemistry-A European Journal* **2013,** *19* (17), 5332-5341.

110. Rodriguez-Rojas, A.; Rodriguez-Beltran, J.; Couce, A.; Blazquez, J., Antibiotics and Antibiotic Resistance: A Bitter Fight Against Evolution. *Int. J. Med. Microbiol.* **2013,** *303*, 293-297.

111. Laxminarayan, R.; Duse, A.; Wattal, C.; Zaidi, A. K. M.; Wertheim, H. F.; Sumpradit, N.; Vlieghe, E.; Hara, G. L.; Gould, I. M.; Goossens, H.; Greko, S.; So, A. D.; Bigdeli, M.; Tomson, G.; Woodhouse, W.; Ombaka, E.; Peralta, A. Q.; Qamar, F. N.; Mir, F.; Kariuki, S.; Bhutta, Z. A.; Coates, A.; Bergstrom, R.; Wright, G. D.; Brown, E. D.; Cars, O., Antibiotic Resistance – The Need for Global Solutions. *Lancet Infect. Dis.* **2013,** *13*, 1057-1098.

112. Sun, Y. P.; Zhou, B.; Lin, Y.; Wang, W.; Fernando, K. A. S.; Pathak, P.; Meziani, M. J.; Harruff, B. A.; Wang, X.; Wang, H.; Luo, P. G.; Yang, H.; Kose, M. E.; Chen, B.; Veca, L. M.; Xie, S. Y., Quantum-Sized Carbon Dots for Bright and Colorful Photoluminescence. *J. Am. Chem. Soc.* **2006,** *128*, 7756-7757.

113. Luo, P. G.; Sonkar, S. K.; Yang, S. T.; Yang, F.; Yang, L.; Broglie, J. J.; Liu, Y.; Sun, Y. P., Carbon-Based Quantum Dots for Fluorescence Imaging of Cells and Tissues. *RSC Adv.* **2014,** *4*, 10791-10807.

114. Wang, Y.; Hu, A., Carbon Quantum Dots: Synthesis, Properties and Applications. *J. Mater. Chem. C* **2014,** *2*, 6921-6939.

115. Lim, S. Y.; Shen, W.; Gao, Z., Carbon Quantum Dots and Their Applications. *Chem. Soc. Rev.* **2015,** *44*, 362-381.

116. Miao, P.; Han, K.; Tang, Y.; Wang, B.; Lin, T.; Cheng, W., Recent Advances in Carbon Nanodots: Synthesis, Properties and Biomedical Applications. *Nanoscale* **2015,** *7*, 1586-1595.

117. Zhao, A.; Chen, Z.; Zhao, C.; Gao, N.; Ren, J.; Qu, X., Recent Advances in Bioapplications of Carbon Dots. *Carbon* **2015,** *85*, 309-327.

118. Cao, L.; Meziani, M. J.; Sahu, S.; Sun, Y. P., Photoluminescent Properties of Graphene versus Other Carbon Nanomaterials. *Acc. Chem. Res.* **2013,** *46*, 171-180.

119. Fernando, K. A. S.; Sahu, S.; Liu, Y.; Lewis, W. K.; Guliants, E. A.; Jafariyan, A.; Wang, P.; Bunker, C. E.; Sun, Y. P., Carbon Quantum Dots and Applications in Photocatalytic Energy Conversion. *ACS Appl. Mater. Interfaces* **2015,** *7*, 8363-8376.

120. Cao, L.; Sahu, S.; Anilkumar, P.; Bunker, C. E.; Xu, J.; Fernando, K. A. S.; Wang, P.; Guliants, E. A.; Tackett, K. N.; Sun, Y. P., Carbon Nanoparticles as Visible-Light Photocatalysts for Efficient CO2 Conversion and Beyond. *J. Am. Chem. Soc.* **2011,** *133*, 4754-4757.

121. LeCroy, G. E.; Sonkar, S. K.; Yang, F.; Veca, L. M.; Wang, P.; Tackett, K. N.; Yu, J. J.; Vasile, E.; Qian, H.; Liu, Y.; Luo, P. G.; Sun, Y. P., Toward Structurally Defined Carbon Dots as Ultracompact Fluorescent Probes. *ACS Nano* **2014,** *8*, 4522-4529.

122. Xu, J.; Sahu, S.; Cao, L.; Bunker, C. E.; Peng, G.; Liu, Y.; Fernando, K. A. S.; Wang, P.; Guliants, E. A.; Meziani, M. J.; Qian, H.; Sun, Y. P., Efficient Fluorescence Quenching in Carbon Dots by Surface-Doped Metals - Disruption of Excited State Redox Processes and Mechanistic Implications. *Langmuir* **2012,** *28*, 16141-16147.

123. Wang, Y.; Anilkumar, P.; Cao, L.; Liu, J. H.; Luo, P. G.; Tackett, K. N.; Sahu, S.; Wang, P.; Wang, X.; Sun, Y. P., Carbon Dots of Different Composition and Surface Functionalization: Cytotoxicity Issues Relevant to Fluorescence Cell Imaging. *Exp. Biol. Med.* **2011,** *236*, 1231-1238.

124. Wang, X.; Cao, L.; Lu, F.; Meziani, M. J.; Li, H.; Qi, G.; Zhou, B.; Harruff, B. A.; Sun, Y. P.; Kermarrec, F., Photoinduced Electron Transfer with Carbon Dots. *Chem. Commun.* **2009**, 3774-3776.

125. Zhang, H.; Huang, H.; Ming, H.; Li, H.; Zhang, L.; Liu, Y.; Kang, Z., Carbon Quantum Dots/Ag3PO4 Complex Photocatalysts with Enhanced Photocatalytic Activity and Stability Under Visible Light. *J. Mater. Chem.* **2012,** *22*, 10501-10506.

126. Dou, Q.; Fang, X.; Jiang, S.; Chee, P. L.; Lee, T. C.; Loh, X. J., Multi-Functional Fluorescent Carbon Dots with Antibacterial and Gene Delivery Properties. *RSC Adv.* **2015,** *5*, 46817-46822.

127. Kleinauskas, A.; Rocha, S.; Sahu, S.; Sun, Y. P.; Juzenas, P., Carbon-Core Silver-Shell Nanodots as Sensitizers for Phototherapy and Radiotherapy. *Nanotechnology* **2013,** *24*, 325103-325113.

128. Juzenas, P.; Kleinauskas, A.; Luo, P. G.; Sun, Y. P., Photoactivatable Carbon Nanodots for Cancer Therapy. *Appl. Phys. Lett.* **2013,** *103* (063701).

129. Wang, X.; Cao, L.; Yang, S. T.; Lu, F.; Meziani, M. J.; Tian, L.; Sun, K. W.; Bloodgood, M. A.; Sun, Y. P., Bandgap-Like Strong Fluorescence in Functionalized Carbon Nanoparticles. *Angew. Chem., Int. Ed.* **2010,** *49*, 5310-5314.

130. Strauss, V.; Margraf, J. T.; Dolle, C.; Butz, B.; Nacken, T. J.; Walter, J.; Bauer, W.; Peukert, W.; Spiecker, E.; Clark, T.; Guldi, D. M., Carbon Nanodots: Toward a Comprehensive Understanding of Their Photoluminescence. *J. Am. Chem. Soc.* **2014,** *136*, 17308-17316.

131. Wang, L.; Zhu, S. J.; Wang, H. Y.; Qu, S. N.; Zhang, Y. L.; Zhang, J. H.; Chen, Q. D.; Xu, H. L.; Han, W.; Yang, B.; Sun, H. B., Common Origin of Green Luminescence in Carbon Nanodots and Graphene Quantum Dots. *ACS Nano* **2014,** *8*, 2541-2547.

132. Ristic, B. Z.; Milenkovic, M. M.; Dakic, I. R.; Todorovic-Markovic, B. M.; Milosavljevic, M. S.; Budimir, M. D.; Paunovic, V. G.; Dramicanin, M. D.; Markovic, Z. M.; Trajkovic, V. S., Photodynamic Antibacterial Effect of Graphene Quantum Dots. *Biomaterials* **2014,** *35*, 4428-4435.

133. Markovic, Z. M.; Ristic, B. Z.; Arsikin, K. M.; Klisic, D. G.; Harhaji-Trajkovic, L. M.; Todorovic-Markovic, B. M.; Kepic, D. P.; Kravic-Stevovic, T. K.; Jovanovic, S. P.; Milenkovic, M. M.; Milivojevic, D. D.; Bumbasirevic, V. Z.; Dramicanin, M. D.; Trajkovic, V. S., Graphene Quantum Dots as Autophagy-Inducing Photodynamic Agents. *Biomaterials* **2012,** *33*, 7084-7092.

134. Ge, J.; Lan, M.; Zhou, B.; Liu, W.; Guo, L.; Wang, H.; Jia, Q.; Niu, G.; Huang, X.; Zhou, H.; Meng, X.; Wang, P.; Lee, C. S.; Zhang, W.; Han, X., A Graphene Quantum Dot Photodynamic Therapy Agent with High Singlet Oxygen Generation. *Nat. Commun.* **2014,** *5*, 4596.

135. Ren, J.; Wang, W.; Zhang, L.; Chang, J.; Hu, S., Photocatalytic inactivation of bacteria by photocatalyst Bi2WO6 under visible light. *Catalysis Communications* **2009,** *10* (14), 1940-1943.

136. Zhang, L.-S.; Wong, K.-H.; Yip, H.-Y.; Hu, C.; Yu, J. C.; Chan, C.-Y.; Wong, P.-K., Effective Photocatalytic Disinfection of E. coli K-12 Using AgBr-Ag-Bi2WO6 Nanojunction System Irradiated by Visible Light: The Role of Diffusing Hydroxyl Radicals. *Environmental Science & Technology* **2010,** *44* (4), 1392-1398.

137. Gan, H.; Zhang, G.; Huang, H., Enhanced visible-light-driven photocatalytic inactivation of Escherichia coli by Bi2O2CO3/Bi3NbO7 composites. *Journal of Hazardous Materials* **2013,** *250*, 131-137.

138. Zhang, Y.; Zhu, Y.; Yu, J.; Yang, D.; Ng, T. W.; Wong, P. K.; Yu, J. C., Enhanced photocatalytic water disinfection properties of Bi2MoO6-RGO nanocomposites under visible light irradiation. *Nanoscale* **2013,** *5* (14), 6307-6310.

139. Arai, T.; Yanagida, M.; Konishi, Y.; Iwasaki, Y.; Sugihara, H.; Sayama, K., Efficient complete oxidation of acetaldehyde into CO2 over CuBi2O4/WO3 composite photocatalyst under visible and UV light irradiation. *The Journal of Physical Chemistry C* **2007,** *111* (21), 7574-7577.

140. Zhang, Y.; Xie, Y.; Li, J.; Bai, T.; Wang, J., Photocatalytic activity and adsorption performance of p-CuBi2O4/n-TiO2 p-n heterojunction composites prepared by in situ sol-gel coating method. *Journal of Sol-Gel Science and Technology* **2014,** *71* (1), 38-42.

141. Zhang, Y.; Li, G.; Zhao, H.; Tian, F.; Xiao, S.; Chen, R., Controllable synthesis of hierarchical Bi2CuO4 microspheres in aqueous solution and their highly efficient visible-light-driven photocatalytic activities. *Crystengcomm* **2013,** *15* (40), 8159-8165.

142. Park, H. S.; Lee, C.-Y.; Reisner, E., Photoelectrochemical reduction of aqueous protons with a CuO vertical bar CuBi2O4 heterojunction under visible light irradiation. *Physical Chemistry Chemical Physics* **2014,** *16* (41), 22462-22465.

143. Patil, R.; Kelkar, S.; Naphadeab, R.; Ogale, S., Low temperature grown CuBi2O4 with flower morphology and its composite with CuO nanosheets for photoelectrochemical water splitting. *Journal of Materials Chemistry A* **2014,** *2* (10), 3661-3668.

144. Ren, L.; Jin, L.; Wang, J.-B.; Yang, F.; Qiu, M.-Q.; Yu, Y., Template-free synthesis of BiVO4 nanostructures: I. Nanotubes with hexagonal cross sections by oriented attachment and their photocatalytic property for water splitting under visible light. *Nanotechnology* **2009,** *20* (11), 115603-115612.

145. Abdulkarem, A. M.; Li, J.; Aref, A. A.; Ren, L.; Elssfah, E. M.; Wang, H.; Ge, Y.; Yu, Y., CuBi2O4 single crystal nanorods prepared by hydrothermal method: Growth mechanism and optical properties. *Materials Research Bulletin* **2011,** *46* (9), 1443-1450.

146. Oh, W.-D.; Lua, S.-K.; Dong, Z.; Lim, T.-T., A novel three-dimensional spherical CuBi2O4 consisting of nanocolumn arrays with persulfate and peroxymonosulfate activation functionalities for 1H-benzotriazole removal. *Nanoscale* **2015,** *7* (17), 8149-8158.

147. Yang, J.; Wang, D.; Han, H.; Li, C., Roles of Cocatalysts in Photocatalysis and Photoelectrocatalysis. *Accounts of Chemical Research* **2013,** *46* (8), 1900-1909.

148. Basnet, P.; Zhao, Y., Tuning the CuxO nanorod composition for efficient visible light induced photocatalysis. *Catalysis Science & Technology* **2016,** *6* (7), 2228-2238.

149. Wang, M.; Zai, J.; Wei, X.; Chen, W.; Liang, N.; Xu, M.; Qi, R.; Qian, X., N-type hedgehog-like CuBi2O4 hierarchical microspheres: room temperature synthesis and their photoelectrochemical properties. *Crystengcomm* **2015,** *17* (21), 4019-4025.

150. Geetu Sharma, Z. Z., Pranab Sarker, Benjamin A. Nail, Jiarui Wang, Muhammad N. Huda, and Frank E. Osterloh, Electronic structure, photovoltage, and photocatalytic hydrogen evolution with p-CuBi2O4 nanocrystals. *Journal of Material Chemistry A* **2016,** *4*, 2936–2942.

151. Wang, M.; Zai, J.; Wei, X.; Chen, W.; Liang, N.; Xu, M.; Qi, R.; Qian, X., N-type hedgehog-like CuBi 2 O 4 hierarchical microspheres: room temperature synthesis and their photoelectrochemical properties. *CrystEngComm* **2015,** *17* (21), 4019-4025.

152. Sharma, G.; Zhao, Z.; Sarker, P.; Nail, B. A.; Wang, J.; Huda, M. N.; Osterloh, F. E., Electronic structure, photovoltage, and photocatalytic hydrogen evolution with p-CuBi 2 O 4 nanocrystals. *Journal of Materials Chemistry A* **2016,** *4* (8), 2936-2942.

153. Lin, H.; Deng, W.; Zhou, T.; Ning, S.; Long, J.; Wang, X., Iodine-modified nanocrystalline titania for photo-catalytic antibacterial application under visible light illumination. *Applied Catalysis B-Environmental* **2015,** *176*, 36-43.

154. Yatvin, M. B., EVIDENCE THAT SURVIVAL OF GAMMA-IRRADIATED ESCHERICHIA-COLI IS INFLUENCED BY MEMBRANE FLUIDITY. *International Journal of Radiation Biology* **1976,** *30* (6), 571-575.

155. Hassan, I. A.; Parkin, I. P.; Nair, S. P.; Carmalt, C. J., Antimicrobial activity of copper and copper (I) oxide thin films deposited via aerosol-assisted CVD. *Journal of Materials Chemistry B* **2014,** *2* (19), 2855-2860.

156. Zhu, L.; Basnet, P.; Larson, S. R.; Jones, L. P.; Howe, J. Y.; Tripp, R. A.; Zhao, Y., Visible Light‐Induced Photoeletrochemical and Antimicrobial Properties of Hierarchical CuBi2O4 by Facile Hydrothermal Synthesis. *ChemistrySelect* **2016,** *1* (8), 1518-1524.

157. Xiu, Z.-m.; Zhang, Q.-b.; Puppala, H. L.; Colvin, V. L.; Alvarez, P. J., Negligible particle-specific antibacterial activity of silver nanoparticles. *Nano letters* **2012,** *12* (8), 4271-4275.

158. Jung, W. K.; Koo, H. C.; Kim, K. W.; Shin, S.; Kim, S. H.; Park, Y. H., Antibacterial activity and mechanism of action of the silver ion in Staphylococcus aureus and Escherichia coli. *Applied and environmental microbiology* **2008,** *74* (7), 2171-2178.

159. Ren, J.; Wang, W.; Sun, S.; Zhang, L.; Wang, L.; Chang, J., Crystallography facet-dependent antibacterial activity: the case of Cu2O. *Industrial & Engineering Chemistry Research* **2011,** *50* (17), 10366-10369.

160. Pegalajar-Jurado, A.; Wold, K. A.; Joslin, J. M.; Neufeld, B. H.; Arabea, K. A.; Suazo, L. A.; McDaniel, S. L.; Bowen, R. A.; Reynolds, M. M., Reprint of: Nitric oxide-releasing polysaccharide derivative exhibits 8-log reduction against Escherichia coli, Acinetobacter baumannii and Staphylococcus aureus. *Journal of Controlled Release* **2015,** *220*, 617-623.

161. Jin, T.; Sun, D.; Su, J.; Zhang, H.; Sue, H. J., Antimicrobial efficacy of zinc oxide quantum dots against Listeria monocytogenes, Salmonella enteritidis, and Escherichia coli O157: H7. *Journal of food science* **2009,** *74* (1), M46-M52.

162. Basnet, P.; Zhao, Y., Tuning the Cu x O nanorod composition for efficient visible light induced photocatalysis. *Catalysis Science & Technology* **2016,** *6* (7), 2228-2238.

163. Read, C. G.; Park, Y.; Choi, K.-S., Electrochemical synthesis of p-type CuFeO2 electrodes for use in a photoelectrochemical cell. *The journal of physical chemistry letters* **2012,** *3* (14), 1872-1876.

164. Edison, T. J. I.; Sethuraman, M., Instant green synthesis of silver nanoparticles using Terminalia chebula fruit extract and evaluation of their catalytic activity on reduction of methylene blue. *Process Biochemistry* **2012,** *47* (9), 1351-1357.

165. Brown, G. T.; Darwent, J. R., Methyl orange as a probe for photooxidation reactions of colloidal titanium dioxide. *The Journal of Physical Chemistry* **1984,** *88* (21), 4955-4959.

166. Qiu, X.; Liu, M.; Sunada, K.; Miyauchi, M.; Hashimoto, K., A facile one-step hydrothermal synthesis of rhombohedral CuFeO 2 crystals with antivirus property. *Chemical Communications* **2012,** *48* (59), 7365-7367.

167. Fan, W.; Wang, X.; Cui, M.; Zhang, D.; Zhang, Y.; Yu, T.; Guo, L., Differential oxidative stress of octahedral and cubic Cu2O micro/nanocrystals to Daphnia magna. *Environmental science & technology* **2012,** *46* (18), 10255-10262.

168. Macomber, L.; Imlay, J. A., The iron-sulfur clusters of dehydratases are primary intracellular targets of copper toxicity. *Proceedings of the National Academy of Sciences* **2009,** *106* (20), 8344-8349.

169. Midander, K.; Cronholm, P.; Karlsson, H. L.; Elihn, K.; Möller, L.; Leygraf, C.; Wallinder, I. O., Surface characteristics, copper release, and toxicity of nano‐and micrometer‐sized copper and copper (II) oxide particles: a cross‐disciplinary study. *Small* **2009,** *5* (3), 389-399.

APPENDIX A

SEM IMAGES OF $CuBi_2O_4$ MICROSPHERES IN SEDIMENTATION

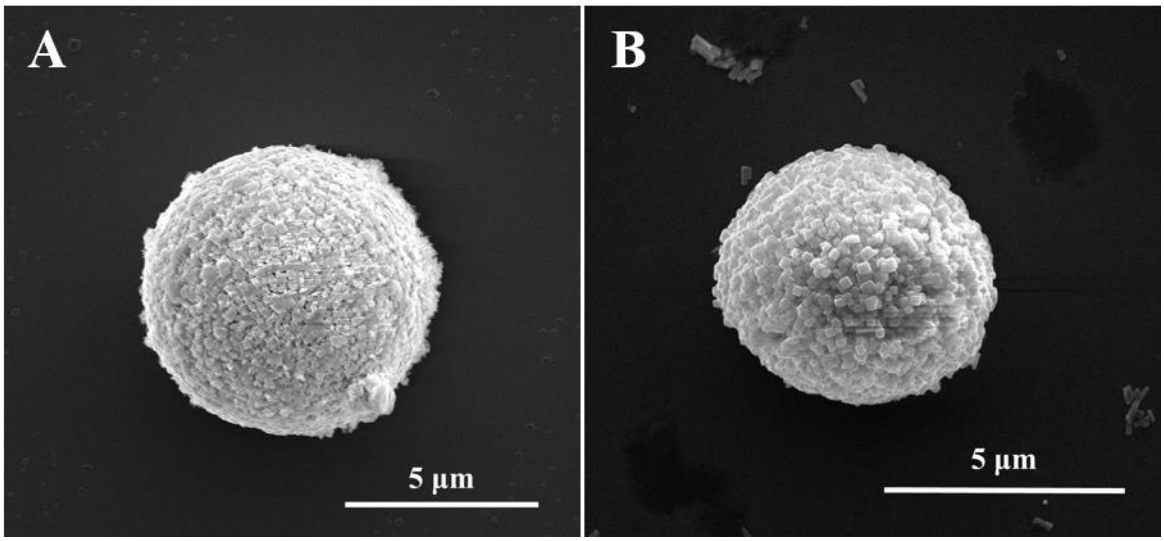

Figure S1. SEM images of microspheres in sedimentation. A: From Sample B, C_{NaOH} = 1.38 M; B: From Sample C, C_{NaOH} = 1.18 M.

APPENDIX B

UV-VIS SPECTRA AND BEER'S LAW PLOTS OF $CuBi_2O_4$ SAMPLES

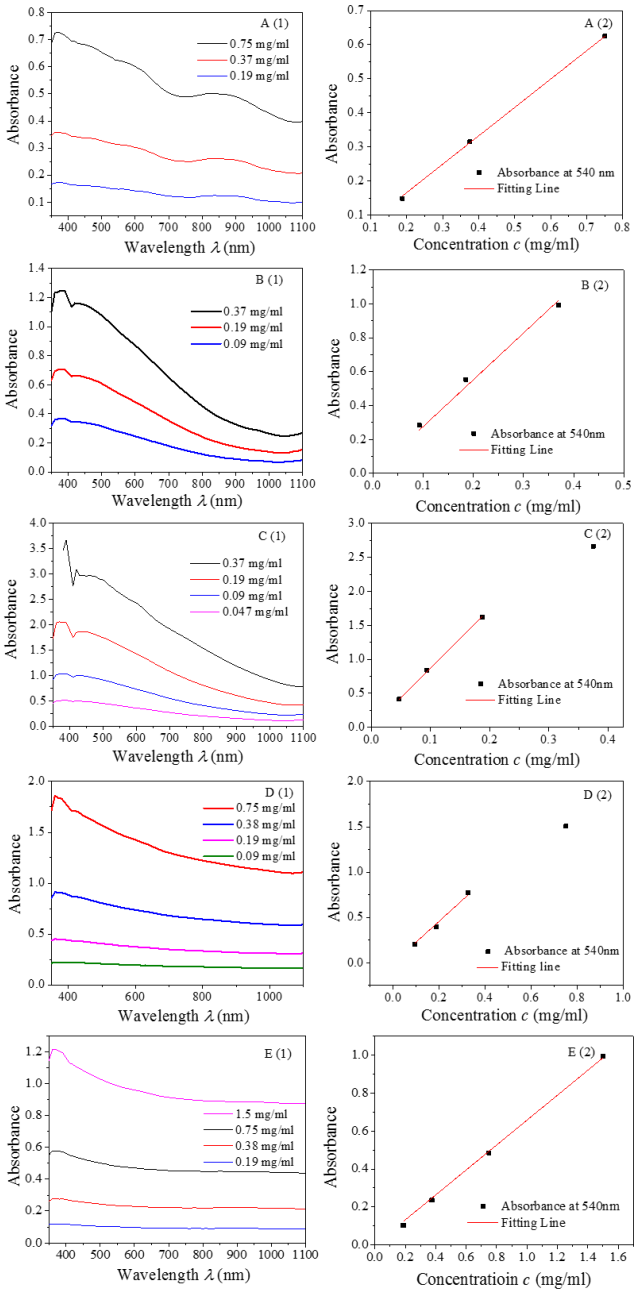

Figure. S2. UV-Vis spectra of different $CuBi_2O_4$ samples (A (1) to E (1)) and their corresponding Beer's Law plots (A (2) to E (2)).

APPENDIX C

UV-VIS SPECTRA BEFORE AND AFTER THE PEC TEST

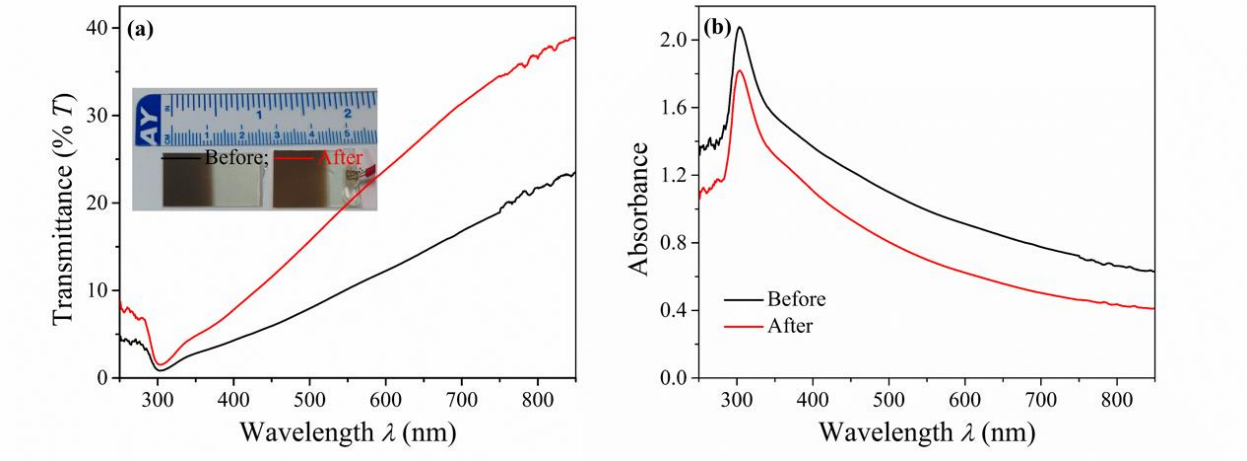

Figure. S3. UV-Vis spectra of a representative $CuBi_2O_4$ sample before and after PEC tests: (a) % Transmittance (%T) and (b) estimated Absorbance from (%T) (i.e. by ignoring the reflectance).

APPENDIX D

XRD PATTERNS BEFORE AND AFTER THE PEC TEST

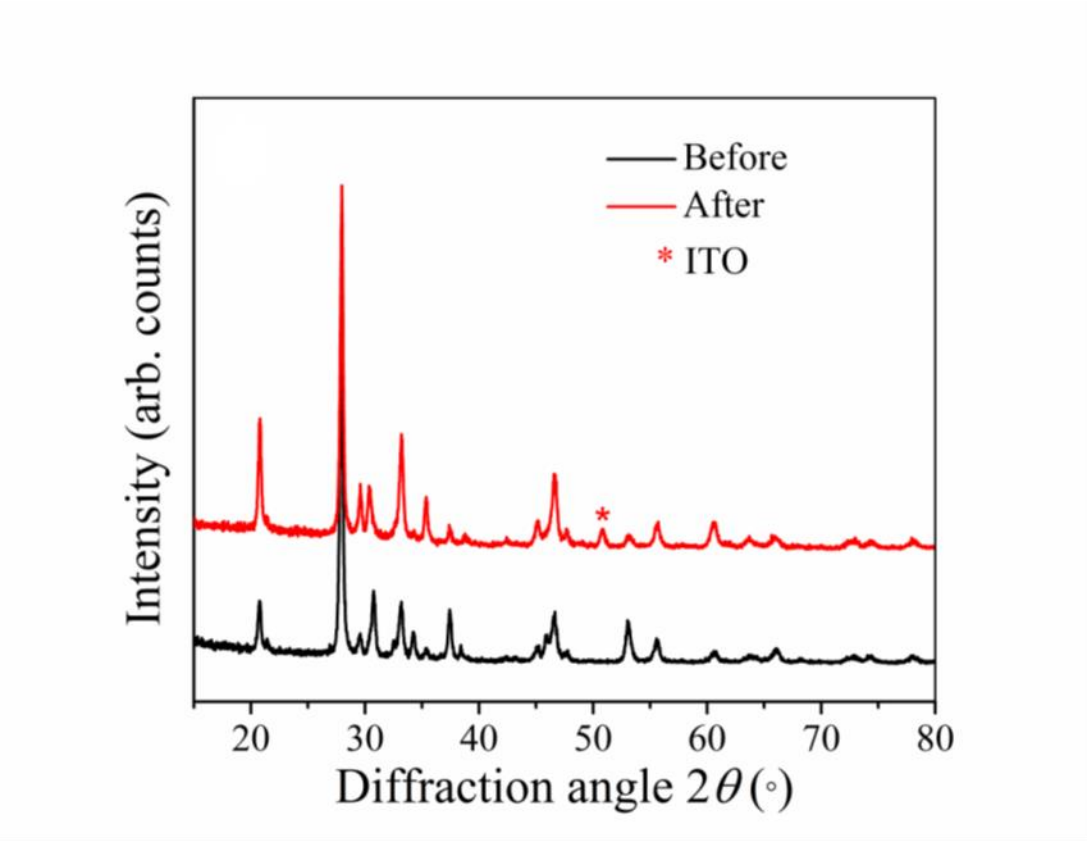

Figure. S4. XRD patterns of a representative $CuBi_2O_4$ sample before and after PEC tests.

APPENDIX E

FILM MORPHOLOGY OF PEC ELECTRODE

Figure. S5 shows the top view and titled view of the PEC electrode. The top view SEM images show that the spray-coated $CuBi_2O_4$ film is relatively flat but not compact on ITO substrate, with micro-sized holes. The sample for titled view SEM imaging was prepared by using a blade to scratch off one side of the coating, and the SEM stage was tilted 55^o when taking the images. The average thickness of the coating layer measured directly from the tiled view is 8 ± 1 μm, and the actual thickness of the $CuBi_2O_4$ coating is estimated as ~14 μm, which would be enough to absorb and utilize the incoming light.

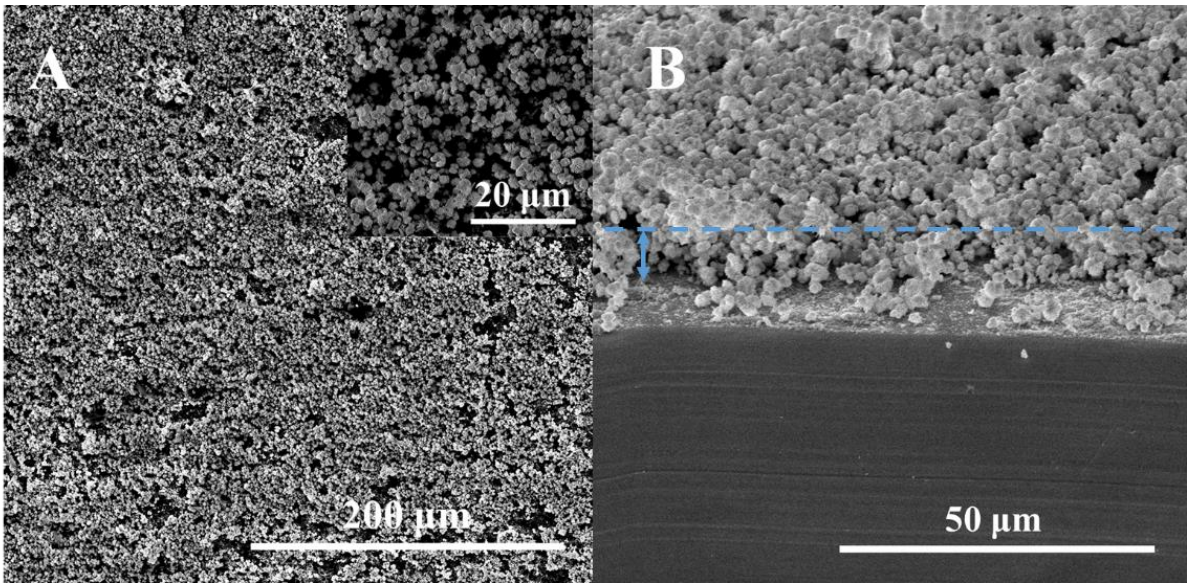

Figure. S5. Top (A) and titled (B) view SEM images of PEC electrode. The insert in (A) is the zoom-in image.

APPENDIX F

EDS MAPPING OF $CuBi_2O_4$ SAMPLE D (MICRO-FLOWERS)

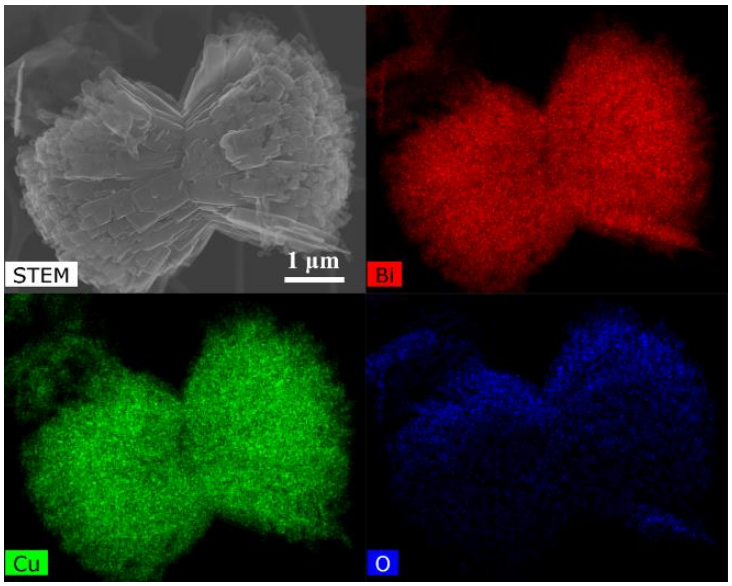

Figure. S6. STEM image and EDS mapping of Bi, Cu and O elements of Sample D.

Table S1. Elemental analysis of Sample D by EDS.

Element	Series	Net	unn. C [wt.%]	norm. C [wt.%]	Atom. C [at.%]	Error (3 Sigma) [wt.%]
Bismuth	L-series	511961	57.92	57.92	9.1	17.45
Copper	K-series	185635	10.61	10.61	5.48	1.03
Oxygen	K-series	11668	0.88	0.88	1.8	0.16
Carbon	K-series	59787	30.59	30.59	83.62	2.85
Nickel	K-series	171384	0	0	0	0
Aluminium	K-series	25949	0	0	0	0
	Total:		100	100	100	